Graduate Theses and Dissertations   Graduate School

2009

Nanocrystalline diamond for RF MEMS applications

Srinath Balachandran
University of South Florida

Nanocrystalline Diamond for RF MEMS Applications

by

Srinath Balachandran

A dissertation submitted in partial fulfillment
of the requirements for the degree of
Doctor of Philosophy
Department of Electrical Engineering
College of Engineering
University of South Florida

Major Professor: Thomas M. Weller, Ph.D.
Shekhar Bhansali, Ph.D.
Jing Wang, Ph.D.
Ashok Kumar, Ph.D.
Sarath Witanachchi, Ph.D.

Date of Approval:
June 15, 2009

Keywords: ncd, charging, high power, capacitive switch, dc switch

Dedication

This dissertation is dedicated to my late parents and late grand parents for the values they taught and instilled in me and also for helping me understand the importance of family and friends in life.

Table of Contents

List of Tables

List of Figures

vii

Nanocrystalline Diamond for RF MEMS Applications

Srinath Balachandran

ABSTRACT

Nanocrystalline diamond (NCD) due its outstanding thermal, mechanical and tribological properties is an ideal candidate for MEMS/NEMS devices. NCD offers the possibility to increase the reliability and life time of RF-MEMS switches and by mitigating the problems of stiction, charge trapping, surface wear and cold welding found in traditional all metal MEMS devices.

In this work, nanocrystalline diamond cantilever beams and bridges have been fabricated on a low resistive silicon substrate by using standard micromachining techniques. The diamond structures are then integrated onto alumina and aluminium nitride substrates upon which microwave transmission lines in the microstrip and coplanar waveguide (CPW) topology have been fabricated. The diamond actuators are integrated using a combined soldering and flip chip technique. The NCD bridges are thermally actuated wherein the difference in coefficient of thermal expansion between copper and diamond bends the diamond bridge thus moving the bridges to the actuated state. In the CPW topology, RF-MEMS switches and tunable planar inductors are realized using the micromachined devices. These devices are mounted on a $650\mu m$ thick alumina substrate and the microwave characteristics are analyzed in the frequency range of 5-30 GHz. The switches yield a return loss of 15 dB and an insertion loss of 0.2 dB at 20GHz. An inductance ratio of 2.2 is achieved by the tunable inductors at 30 GHz. High power measurements are performed on the diamond actuators which utilize a dual actuation scheme which comprises of thermal and electrostatic actuation. The measurements are performed on the diamond actuators in the power range of 24-47 dBm

for the mechanically actuated switches, and 24-40 dBm for electrically actuated switches. The measurements show an insertion loss of 0.2-03 dB in the entire power spectrum.

NCD based RF-MEMS capacitive switches is also designed, fabricated and tested. The switches are fabricated on a high resistive silicon substrate and are electrostatically actuated. Small signal measurements are presented in the frequency range of 1-65 GHz. The measured insertion loss in the up-state is 1.1 dB at 50 GHz with 30 dB isolation in the down-state. Dielectric characterization is performed using the Corona-Kelvin technique and the standard I-V and C-V stress tests for nitride and diamond films. The leaky nature of the diamond films provides a potential solution to reliability issues related to dielectric charging.

Preface

I sincerely thank my major professor and advisor, Dr. Tom Weller for allowing me to work in this project. His continued support, encouraging words and the confidence he had in me helped me overcome various setbacks throughout the project. His technical insight, patience and humility make him one of the best advisors one could ask for. It was a pleasure working for and with him over the years and I thank him for making me a better person both from a professional and personal front.

I would like thank the committee members, Dr. Shekhar Bhansali, Dr. Jing Wang, Dr. Ashok Kumar and Dr. Sarath Witanachchi for taking the time to serve on my committee. Furthermore, I thank the dean for the college of engineering, Dr. John Wiencek for chairing my dissertation defense. Along with Dr. Weller, Dr. Dunleavy was instrumental in setting up excellent measurement facilities and I would like thank them for taking great efforts in making them available to us. Many thanks to Dr. Bhansali and Dr. Kumar for providing good fabrication facilities in the college and for their timely suggestions in the dissertation work. Dr. Andrew Hoff was very helpful in sharing his expertise in charging measurements. I am very thankful to him for always being there to answer my numerous questions and offer fruitful suggestions. I would also like to thank Dr. Jeremy Muldavin for his timely and valuable inputs regarding charging experiments.

The fabrication portion of the diamond actuator portion of this dissertation was carried out through research collaboration at the University of Ulm. I am deeply indebted to Prof. Erhard Kohn from the institute of electron devices and circuits for allowing me to carry out this research with his group. During the two stints of my stay at the University, I had the great opportunity of learning and working on state of art facilities in the institute. I am very thankful to Joachim Kusterer, Michele Dipalo and David Maier for all the help they had extended during my stay at the university. I have indeed learned a lot from them and I am deeply indebted to them for accommodating me in their research projects.

My friends from my high school, undergraduate studies, Houston, Germany and India- many thanks to each and everyone for your support and friendship. It was a pleasure knowing you all and I value your friendship a lot.

Finally, I would like to thank my sister, Vidya and my uncles, Krishnan and Sekar for their continued support throughout my education and also standing by me in all the tough times. I am for ever indebted for what they have done for me. My brother in law, Kumar for his encouragement and motivation, and the entire Sivadas and Munirathnam families for their love, affection and encouragement.

Chapter 1

Introduction

1.1 Overview

Micro-Electro-Mechanical Systems (MEMS) technology is a rapidly growing field and finds various applications that include RF/Microwave circuit design, including the development of switches and tuning elements such as capacitors and inductors. MEMS are integrated systems combining both electrical and mechanical components. They are traditionally in the microscale, but also extend to a few millimeters. MEMS devices can be used as miniature sensors, controllers or actuators and have commercial uses which include pressure sensors, flow sensors, accelerometers, and optical scanners [1-3]. Switches are fundamental components that are used in Radio Frequency Integrated Circuits (RFICs) and other wireless front-end circuitry. Switches are of different kinds and can be broadly classified as active and passive. Field effect transistors (FETs) and PIN diodes are generally used in active switches. RF-MEMS based devices predominantly use passive, metal contact or capacitive type switches. In addition to being used in passive tuning circuits, inductors play a role in resonators for low phase-noise voltage controlled oscillators, filter components and reactive impedance elements in RF circuits.

RF-MEMS devices are fabricated through bulk micromachining, surface micromachining, or LIGA techniques [1-4]. Bulk micromachining is the process of fabricating devices by directly etching into a wafer. In this technique both sides of the wafer can be patterned and etched and can be used to assemble three dimensional structures. The method is widely used in forming membranes, holes, beams and grooves [4]. The surface micromachining technique consists of building up micro electro mechanical structures in layers of thin films on the surface of a wafer (or any other suitable substrate). It is different from bulk processes as the devices are fabricated

1

entirely out of the thin film material. Unlike surface milling, in surface micromachining layers of materials can be added or subtracted [1, 4]. LIGA is a German acronym which stands for Lithography, Electroplating and Molding and is a technique used to produce molds for the fabrication of micromachined components [5].

At present, MEMS components are dominated by silicon technologies. Silicon is the only material to combine sensors and actuators with passive and active electronics for signal readout, data conversion, data processing, data storage, and so forth. Silicon wafer substrates or films as well as fabrication methods for devices have reached a nearly ideal status in terms of quality and yield. However, for applications under extreme conditions silicon may not be suitable any more. Such harsh environments are for instance high temperatures, aggressive media, or high energy particle radiation. For these purposes semiconductors with a wide bandgap and ceramics are preferable. An excellent candidate in this respect is diamond. It is extremely hard and stiff, mechanically and temperature stable, chemically inert and corrosion resistant, piezoresistive, and has the highest thermal conductivity of all natural solids at room temperature. Its resistivity range can be varied by doping over about 10^{15} orders of magnitude from highly insulating to quasi-metallic. Besides, its mechanically-relevant material properties such as Young's modulus and hardness remain practically the same within a wide range of temperature. Also quasi-metallic electrical conductivity is nearly temperature independent within typical operation regimes of MEMS.

With particular reference to RF-MEMS switches, the superior mechanical and electrical properties of diamond can eliminate, or at least mitigate, common failure mechanisms. For Ohmic switches these mechanisms include wear at contact surfaces, surface hardening and cold welding which can arise from electrical arching and resistive heating. The high hardness and thermal conductivity of nanocrystalline diamond (NCD) enables significant improvements in each of these areas. However, for Ohmic switches, if diamond is to be used as contact, it needs to have high electrical conductivity, which currently is only provided by the unique nitrogen-doped ultrananocrystalline diamond (N-UNCD) developed and patented at Argonne National Laboratories [6]. For the capacitive switches, an additional failure mechanism is charge trapping at the surface of the

insulating material used on the bottom electrode (typically silicon nitride or SiO_2); depending on the nature of the trapping the switch may spontaneously release or remain closed when the bias voltage is removed. The dielectric properties of diamond films can be varied by controlling the amount of incorporated hydrogen in the plasma and thereby changing the carbon bonding configuration at the grain boundary, providing a novel approach to producing a leaky dielectric, which is one approach to minimizing or eliminating the charging problem in RF-MEMS switches.

This research is mainly focused on combining NCD films and RF-MEMS technology to generate tunable NCD DC contact switches, inductors and capacitive shunt switches using diamond as a dielectric. The DC contact switches are fabricated on a low resistivity silicon substrate and a combination of surface and bulk micromachining techniques are used to realize tunable devices in CPW and microstrip configurations. The tunable switches and inductors are integrated using solid-liquid interdiffusion, which is a popular technique in assembling interconnects in the IC industry. Figure 1.1 shows the cross section of an integrated NCD actuator to a host substrate which carries the microwave transmission lines.
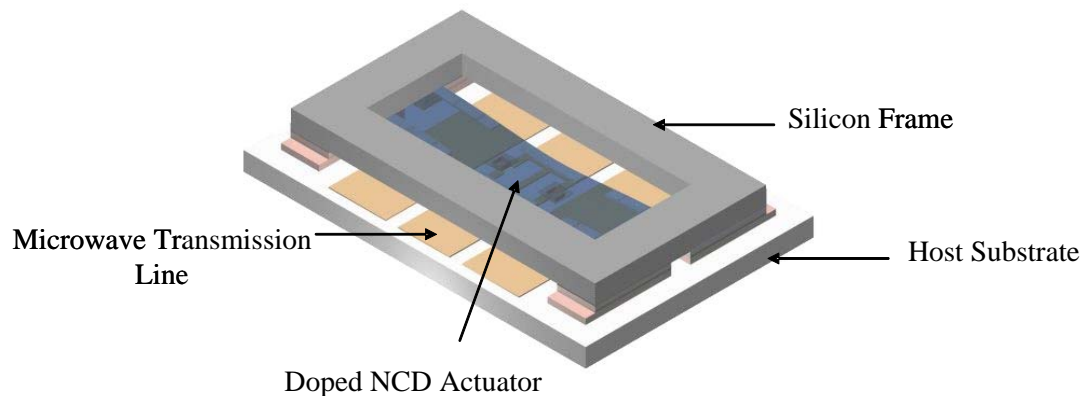
Figure 1.1 – Cross Section of the NCD Actuator Integrated to a Host Substrate

In order to fabricate these actuators for reliability, the mechanical characteristics of NCD thin films should be well understood. The first part of this research is focused on the growth process, material and mechanical characterization of doped and undoped NCD

films. The diamond actuators are designed to operate in a bi-stable configuration. In order to understand the operation, mechanical simulations using ANSYS^{TM} are carried out. The microwave performance of the switches and inductors is studied by measuring the S-parameters of the devices in the frequency range of 1- 40 GHz. Finally, these actuators are tested for microwave performance and mechanical stability by performing large signal measurements at 1.9 GHz and 2.1 GHz with varying power levels.

The next portion of this research is focused on developing capacitive shunt switches using NCD as a dielectric. Figure 1.2 shows the top view of the device. Prior to making these devices, the growth of NCD on metallic films is studied. In order to obtain reliable films, diamond requires carbide forming materials. For this purpose both tungsten and molybdenum deposited by sputtering techniques are used.
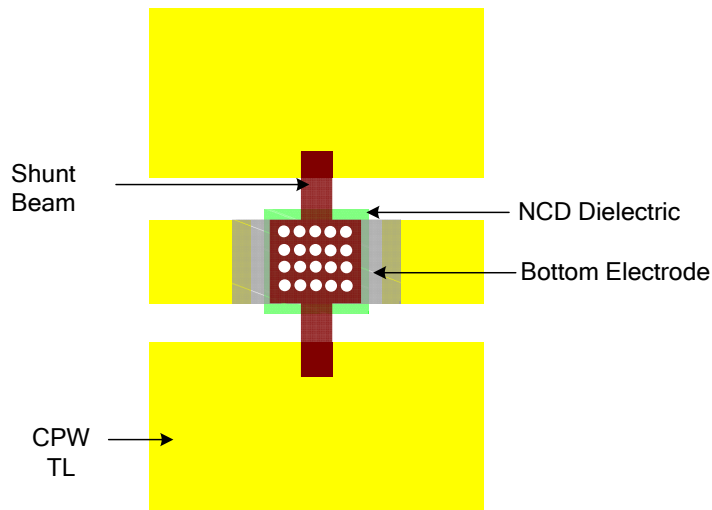
Figure 1.2 – Design of the Capacitive Shunt Switch with NCD as a Dielectric

Electromagnetic simulations using Agilent's Advanced Design System (ADS) software and small signal measurements are carried out in the frequency range of 1-65 GHz to understand the microwave characteristics of the switch. The charging characteristics of thin film NCD is studied using Corona Kelvin metrology (CKM), C-V and I-V measurements to demonstrate the leaky and non-charging nature of the diamond films. These measurements are carried out for NCD based metal-insulator-metal (MIM) capacitors and MEMS switches.

4

1.2   Dissertation Organization

Chapter 2 presents the background of RF-MEMS technology. Different types of capacitive switches along with S-parameter simulation results and lumped element models will be presented. A comprehensive study of the limitations of capacitive and DC contact switches will be discussed. Furthermore, the various microactuation techniques are discussed along with the parameters which have an influence on the actuation voltage. The mechanical aspects, forces which play a role in the bending of the beams, and their uses in the area of MEMS are discussed.

In Chapter 3, the growth along with the seeding techniques to develop intrinsic and doped NCD films will be presented. The two popular schools of thought involved in diamond growth, hydrogen chemistry and argon chemistry, are discussed in detail. Apart from micromachining techniques, measurement techniques to understand the mechanical properties that include Young's modulus, intrinsic stress and mechanical resonant frequency of NCD cantilevers are reviewed. Finally, the effect of process of parameters on the intrinsic stress during growth and its distribution on a 4-inch wafer will be highlighted through measurements.

The design, fabrication and measurement results of a thermally actuated NCD actuator are presented in Chapter 4. Mechanical simulations are performed in ANSYS^{TM} to achieve bi-stable mode of operation of the actuator and small signal simulations of the switch and tunable inductor are performed in Agilent's ADS software. In addition to the integration techniques, high power measurements of the NCD actuator integrated in a microstrip topology will be presented.

Chapter 5 deals with the design, fabrication and measurement of NCD based capacitive shunt switches. Material characterization highlighting the quality of diamond growth on metallic thin films will be presented. In addition to the simulation and measurement of S-Parameter results, charging properties of NCD as a dielectric will be discussed using Corona Kelvin metrology (CKM), I-V and C-V measurements. C-V and I-V measurements are performed on both MIM and MEM structures.

Chapter 6 concludes the dissertation with a discussion of improvements and future directions for NCD based RF-MEMS devices. For completeness, appendices with fabrication details are presented.

1.3   Contributions

The following contributions have been made to the RF-MEMS and diamond community through this dissertation research.

- A thorough analysis of the growth process involved in developing intrinsic and doped diamond films. The two schools of thought, hydrogen chemistry and argon chemistry, and the various seeding methodologies and their effect on the quality of the films are discussed. Although system dependent, the various process parameters which are involved in controlling the stress in the NCD films have been studied.

- A thermally actuated NCD based actuator is integrated using a SOLID^{TM} process to realize RF-MEMS based switches and tunable inductors in a CPW topology. The switches and inductors are tested up to 40 GHz. High power measurements are performed on the microstrip switch in the power range of 24-47 with an insertion loss of 0.2-0.3 dB in the entire frequency range. To the best of the author's knowledge this is the first demonstration a fully integrated diamond switch for microwave applications.

- Intrinsic NCD films are used as the dielectric layer in capacitive shunt switches. The switch is electro-statically actuated and small signal measurements are presented in the frequency range of 1-65 GHz. The measured insertion loss in the up-state is ~ 1.1 dB at ~50 GHz with 30 dB isolation in the off-state. Dielectric characterization was performed using the Corona-Kelvin technique and standard I-V testing on comparison nitride and diamond test fixtures. The leaky nature of the diamond films provides a potential solution to reliability issues related to dielectric charging. To the best of the author's knowledge this is the first RF-MEMS capacitive switch using NCD as a dielectric.

Chapter 2
RF-MEMS – An Overview of the Technology and its Reliability Issues

2.1 Introduction

Micro-Electro-Mechanical Systems (MEMS) technology is a rapidly growing field and finds various applications that include RF/microwave circuit design. MEMS are integrated systems combining both electrical and mechanical components. MEMS structures are batch fabricated using standard integrated circuit processing techniques and can range in size from micrometers to millimeters. These devices have been in development since the early 90's and have since matured and attract significant attention in defense and commercial applications. Their commercial applications are in the wireless, automotive and biomedical industries and they have been used in accelerometers, pressure sensors and flow sensors. Micromachining provides a new dimension to the fabrication of high performance and low cost circuits when compared to the circuits fabricated using conventional MMIC processing. The field of MEMS and micromachining has been applied to RF (less than 2GHz) to millimeter wave frequency (3 to 300GHz) circuits to create high-performance passive components such as switches, phase shifters, high-Q varactors, tunable filters, matching networks and oscillators [7].

In this chapter, RF-MEMS switches with various topologies and actuation schemes will be presented. An overview of capacitive switches with small signal simulation results performed in Agilent's Advanced Design System (ADS) will be presented. Finally the shortcomings of RF-MEMS that include power handling limitations for Ohmic contact switches and reliability issues due to charging in capacitive switches will be discussed in detail.

2.2 Overview of RF-MEMS Switches

Most of the RF-MEMS devices designed and fabricated to date use silicon, glass, or quartz substrates [8-10] and are monolithically integrated. These devices have been fabricated utilizing electrostatic [8], thermal [9] and piezoelectric [10] actuation schemes. RF switches are one of the most researched and fabricated devices in the MEMS technology. These devices outperform their active counterparts that include field effect transistors (FETs) and pin-diodes in terms of loss at high frequencies, linearity and power consumption. Although established since its introduction in the early 90's, RF-MEMS devices still has reliability issues, slow switching speed, high packaging costs and high power handling limitations in comparison to the active devices. Recent developments have at least reduced the above mentioned limitations. Table 2.1 [7] presents a comparison of MEMS switches with PIN diodes and FETs.

Table 2.1 – Performance Comparison Between FETs, PIN Diodes and RF-MEMS Switches

Parameters	RF-MEMS	PIN	FET
Actuation Voltage (V)	20 - 80	+/-3 - 5	3 – 5
Power Consumption (mW)	0.05 - 0.1	5 - 100	0.05 - 0.1
Switching Time	1 - 300 μs	5 - 100 ns	1 - 100 ns
Isolation (1-10 GHZ)	Very High	High	Medium
Isolation (10-40 GHZ)	Very High	Medium	Low
Loss (1-40 GHZ) (dB)	0.05 - 0.2	0.3 – 1.2	0.4 – 2.5
Power Handling (W)	<1	<10	<10

RF-MEMS switches can be fabricated using a floating cantilever (dive board design) or fixed-fixed membrane as shown Figure 2.1 and Figure 2.2, respectively. These moveable membranes are modeled as mechanical springs with an equivalent spring constant, k [N/m]. The spring constant depends on the geometrical dimensions of the membrane or cantilever and on the Young's modulus of the material used (Au, Al,

nitride, etc.) and is 5-40 N/m for most RF-MEMS switch designs [7]. The switches have very low mass, around 10^{-10} to 10^{-11} Kg and, therefore, are not sensitive to acceleration forces. These switches can be fabricated in the microstrip and CPW topologies. In a CPW configuration, the anchors of the switch are directly connected to ground plane or signal line depending on the switch type. Via-holes or a quarter wavelength open stub are used to connect the anchors to the ground plane in the microstrip topology. RF-MEMS switches can be fabricated as DC contact or capacitively coupled switches. The following section presents the design and simulation results of series and shunt capacitive switches.
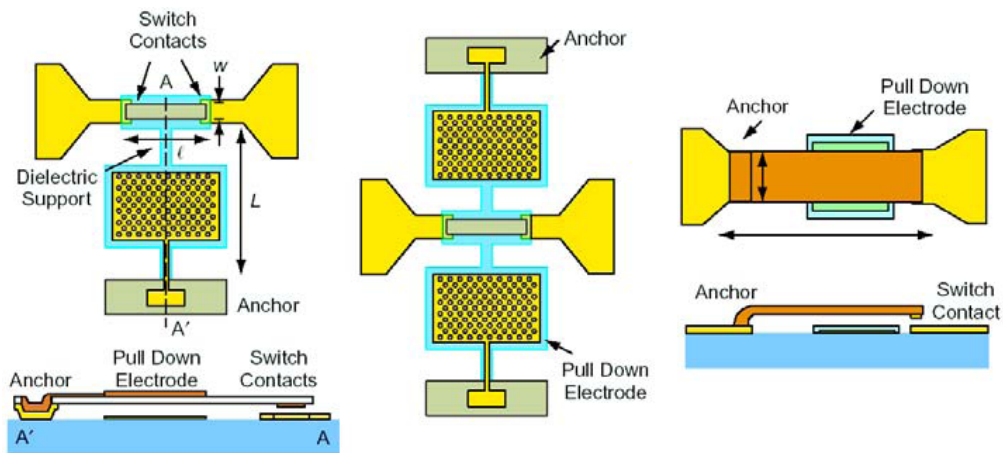
Figure 2.1 – Broadside MEMS Series Switch Utilizing Cantilever Beams [11]
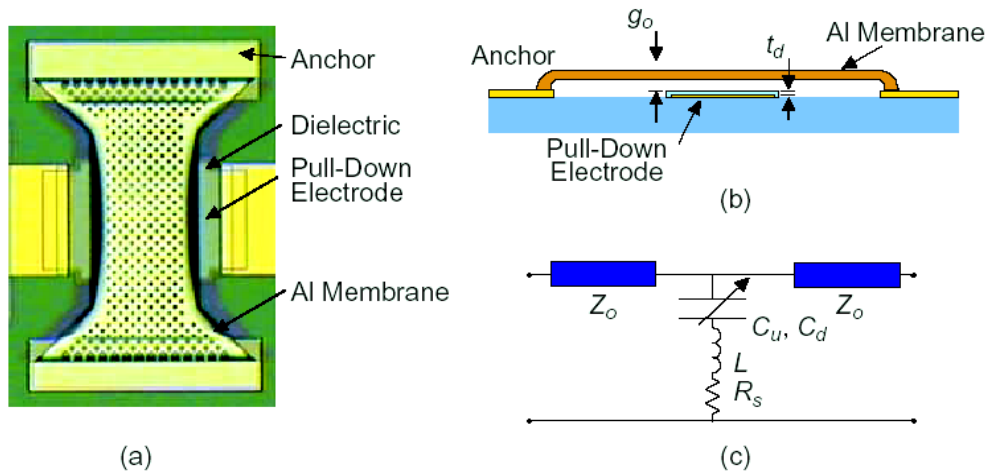
Figure 2.2 – Raytheon MEMS Capacitive Shunt Switch Utilizing Fixed-Fixed Beam [11]

2.2.1 Capacitive Switches

Capacitive RF-MEMS switches consist of a movable membrane that is used to realize a variable capacitance, and thereby a variation in impedance between the non-actuated ("OFF") and actuated ("ON") states. A DC voltage is applied between the bridge and the transmission line, causing the bridge to collapse on a dielectric layer. The increased capacitance value that arises when the bridge or beam is actuated connects the transmission line to the ground and acts as a short at microwave frequencies. The dielectric layer in capacitive switches is generally formed using a PECVD growth process to achieve conformal deposition. The dielectric thickness depends on the required capacitance ratio as per the application. The popular dielectric materials used in RF-MEMS switches are silicon nitride and silicon oxide. The bridge height is typically between 2-3 μm, length of the moveable membrane is 250-400 μm, and the width is between 30-150 μm. As stated earlier, capacitive switches can be designed in series and shunt configurations; Figure 2.3 shows a RF-MEMS capacitive switch in a series configuration.
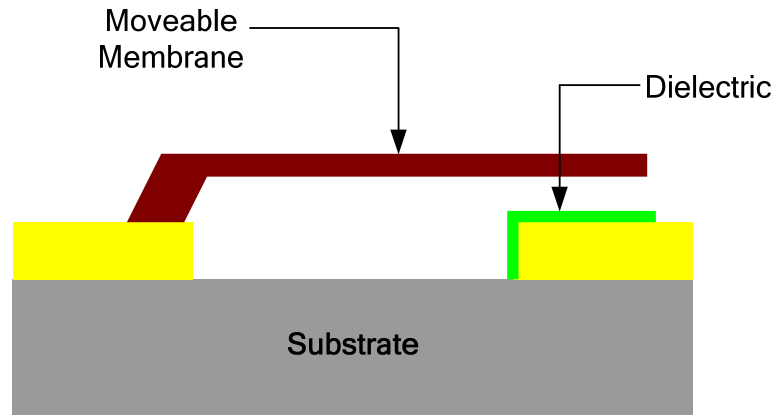
Figure 2.3 – Capacitive RF-MEMS Switch in a Series Configuration

Relatively simple circuit schematics can be used to emulate the electrical response of a capacitive switch. The capacitive switch shown in Figure 2.3 can be represented as a series capacitor-inductor-resistor (CLR) network. Figure 2.4 shows the circuit schematic of a series capacitive switch; in this circuit the series capacitance varies between 30fF in the non-actuated state to 3 pF in the actuated state. The inductance contributed by the

bridge is assumed to be 10 pH, and the contact resistance contributed by the bridge is accounted for with the 0.5 Ω resistor.
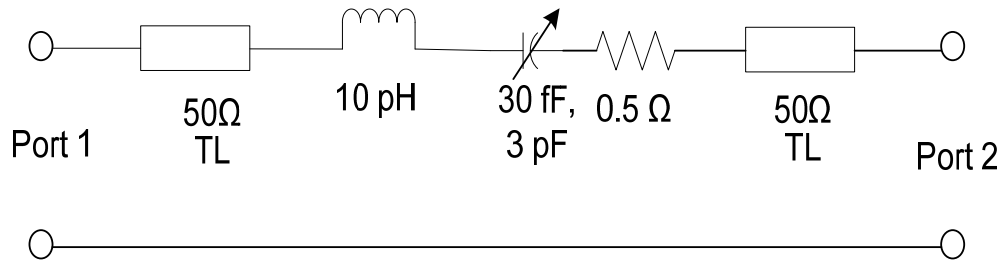
Figure 2.4 – Equivalent Circuit of a Series Capacitive Switch

One of the major disadvantages of a series capacitive switch is the low return loss associated with the non-actuated state. When the beam is the up-state, which is the RF-OFF (non-actuated) state, the switch capacitance is small and hence most of the signal is reflected back. When actuated, i.e. when the beam makes contact with the dielectric layer, the switch capacitance becomes high and the switch is the ON state. In this state, the switch exhibits a high–pass characteristic with the cut-off frequency. The cut-off frequency, which is controlled by the bridge inductance and capacitance values, defines the working range of the device. For the circuit in Figure 2.4, the device can be considered as a switch for a frequency less than 5 GHz wherein the isolation is greater than 20 dB in the OFF state and the insertion loss is less than 1 dB in the ON state. Figure 2.5 shows the S-parameters of the series switch in the OFF and ON states. For an ideal series switch designed to provide an isolation and insertion loss better than 40-50 dB and 0.2dB in the K band frequency range, respectively, the capacitance ratio should be on the order of ~ 3000. This ratio is difficult to achieve in practice, often prompting the use of a DC contact switch in combination with a capacitive shunt switch [12].
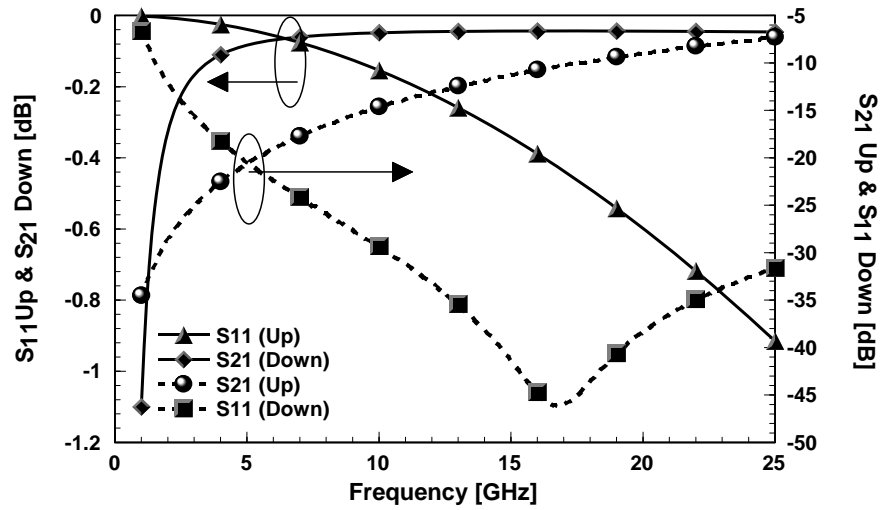
Figure 2.5 – S-Parameters of the Capacitive Series Switch in the OFF and ON States

Figure 2.6 and Figure 2.7 show the design and equivalent circuit of a capacitive shunt switch, respectively. Similar to the series switch, the capacitance varies between 30 fF in the OFF state to 3 pF in the ON state. The inductance and resistance values are assumed to be similar to that of the series switch.
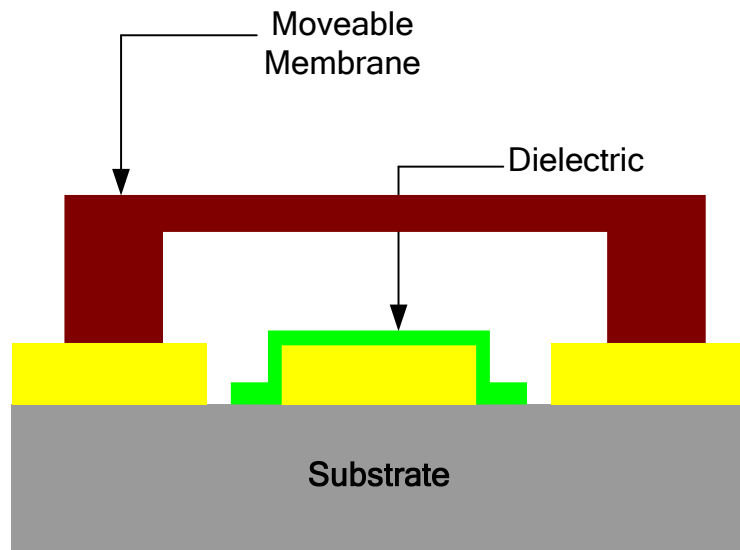
Figure 2.6 – Capacitive RF-MEMS Switch in Shunt Configuration
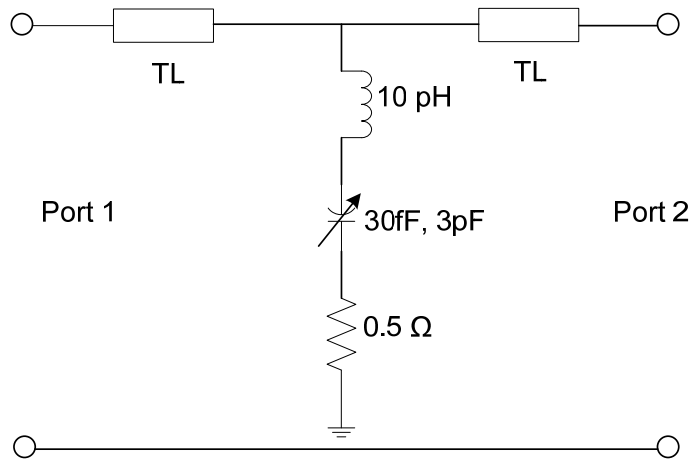
Figure 2.7 – Equivalent Circuit of a Capacitive Shunt Switch

In the shunt switch, when the beam is in the non-actuated state, the return loss is dominated by the 30 fF capacitor. Upon actuation, the signal goes through the high capacitance path to ground, thereby providing good isolation between the two ports. Figure 2.8 shows the simulated S-parameters of the capacitive shunt switch in the ON and OFF states. At high frequencies the combined effect of the inductance of the bridge and capacitance causes a resonance (minimum impedance to ground) in the isolation response.
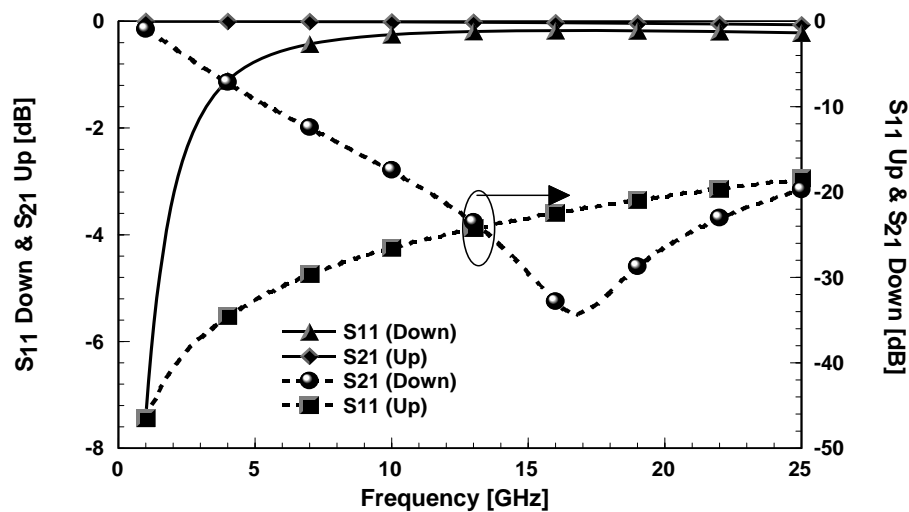
Figure 2.8 – S-Parameters of the Capacitive Shunt Switch in the ON and OFF States

The capacitive shunt switch developed by C. Goldsmith et al. [13] and the DC contact series switch developed by Lincoln laboratories [14] have been used as standards in their respective configurations.

2.3   Actuation Schemes in RF-MEMS

Actuation refers to the act of affecting or transmitting mechanical motion, forces and work by a device or system on its surroundings in response to the application of a bias voltage or current [15]. Considerable research has been directed at designing and fabricating RF-MEMS devices with a variety of different actuation schemes. The most popular actuation schemes used in MEMS processes are electrostatic actuation, piezoelectric actuation, magnetic actuation, and thermal actuation

Electrostatic actuation [1, 2], which is the simplest and the easiest to control, is the preferred actuation scheme in many MEMS applications. In this case, the positive and negative charges set by applied voltages on structures elicit Coulomb forces which cause motion. This electrostatic force between a top and bottom electrode when a DC potential is applied is given by

$$F = \frac{QE}{2} = \frac{\varepsilon A V^2}{2\left(g + \dfrac{t_d}{\varepsilon_r}\right)^2} \tag{2.1}$$

where V, g, and t_d are the voltage, electrode gap and thickness of the dielectric layer, respectively. The threshold voltage which is the voltage at which the moveable membrane falls on to the bottom electrode, can be approximated to the value shown in equation 2.2 wherein V_{th} is the threshold voltage, E is the Young's modulus, I is the geometrical moment of inertia, t_d is the inter-electrode distance, and l and w are the length and width of the structure.

$$V_{th} = \sqrt{\frac{18EIt_d^3}{5\varepsilon_0 \ell^4 w}} \tag{2.2}$$

Electrostatic actuation is useful in applications where integration on a chip is easy from a fabrication point of view. Most of the MEMS beams which are easily fabricated require more than 15 volts for actuation, which is typically not compatible with low

14

voltage CMOS applications. Also, there is no proper scheme for producing repulsive forces using this method of actuation. In addition to RF-MEMS switches, electrostatic actuation is also used in actuators for resonators and light modulators

Piezoelectricity is a phenomenon in which a mechanical stress on a material produces an electrical polarization and, reciprocally, an applied field produces a mechanical stress. In piezoelectric actuation [7] the applied voltage induces fields which change the dimension of structure and this dimensional change is used to cause motion. Here the electrically induced strain is approximately proportional to the applied electric field. The stress associated with this actuation scheme is very high, which constitutes a high energy density. Piezoelectric actuation scheme has its share of advantages and disadvantages in comparison to electrostatic actuation. Although the actuation voltage is very less (w.r.t electrostatic actuation), integrating piezo materials with host substrate and the fabrication methodologies are complicated. Potential limitations of piezoelectric actuation include hysteresis behavior, change in response over time [16]. Piezoelectric materials (ZnO, AlN) are characterized by the charge sensitivity coefficients, d_{ij}, which relate the amount of charge generated at the surfaces of the material on the i axis to the applied force, F, on the j axis

$$\Delta Q_i = d_{ij}\Delta F_j = d_{ij}\Delta\sigma A \qquad (2.3)$$

The voltage across the electrodes can be given as,

$$V = \frac{Q}{C} = \frac{Qx}{\varepsilon_0\varepsilon_r A} \quad ; \quad \Delta V_i = \frac{d_{ij}\Delta F_j x}{\varepsilon_0\varepsilon_r A} \qquad (2.4)$$

The popular materials which exhibit piezoelectric properties are barium titanate (BaTiO$_3$), lead zirconium titanate (PZT), zinc oxide (ZnO) and aluminum nitride (AlN). These materials have been used in many RF-MEMS devices such as phase shifters, filters etc. [7]

Magnetic actuation is not common in MEMS process because, apart from being incompatible with CMOS processes, the fabrication process is very tedious. In this actuation scheme, the magnet-induced or current-induced magnetic force produces

motion. This force is caused when charge carriers travel through a perpendicular magnetic field thereby causing a deflection; this is popularly known as the Lorentz force [17]. The charges produce a voltage called the Hall voltage which is used in the actuation scheme. The hall voltage as shown in equation 2.5 is dependent on the hall coefficient (R_H), current density (J), width of the structure (W), and magnetic flux density (B_Z).

$$V_H = R_H J_X W B_Z \qquad (2.5)$$

Magnetic actuation [2, 7] is difficult because ferromagnetic materials are required for focusing the magnetic flux needed for actuation. On the positive side, magnetic actuation in MEMS provides sufficient force and requires very small voltages for actuation. Magnetic actuators find their application in micro generators and in low-voltage/large – force /low –efficiency actuators.

In the case of thermal actuation, the current or voltage applied causes an element to heat up and expand. This expansion results in a dimensional change used to communicate motion. The coefficient of thermal expansion, α_L, quantifies the relative dimensional change of an object that occurs for a change in temperature. The movement in the actuator is achieved when two dissimilar materials with different α_L are sandwiched together. This principle is used in thermostat switches which use the bimetallic or thermal bimorph mechanism. Similar to magnetic actuation, thermal actuation requires very low voltage for actuation. Power consumption, which is a major limitation of this scheme, can be avoided by using bi-stable structures [18] or dual mode actuation schemes [19]. Thermal actuation is used in gas pressure sensors, thermal flow sensors and in humidity sensors [2].

Apart from the aforementioned there are other actuation schemes that include electrostrictive actuation, magnetostrictive actuation, ultrasonic actuation and chemical actuation. These methods are not widely popular and are used for specific purposes depending on the nature of the application.

16

2.4   Failure Mechanisms of RF-MEMS Switches

When first introduced, RF-MEMS devices had limitations with reliability, power handling, switching speed, high-voltage drive and packaging. Recent developments by researchers at MIT Lincoln Lab and the University of California at San Diego [14, 20] have successfully demonstrated long term reliability up to a few hundred billion cycles. These reliability experiments have been carried out for both DC contact and capacitive switches under hot and cold switching conditions. The switching speed of RF-MEMS devices was considered slow in comparison to active competitors, however special fabrication techniques like the focused ion-beam (FIB) milled nano-switch [21] and "Mini-MEMS" [22] switches have shown switching speed in the hundreds of nanoseconds. Further improvements in these designs are in progress to improve the switch speed to less than 200 ns. Performance and reliability of the switches due to packaging have been partially addressed in terms wafer level and chip level packaging. Glass frit wafer bonding [23], metallic cap technique [24] by Teravicta, low temperature thermosonic flip chip and low temperature glass seal ring [25] by XCOM wireless are the popular packaging schemes available. Long term reliability and the high cost associated with these techniques are still being addressed.

Apart from the above stated problems, there are two main issues when it comes to the reliability of RF-MEMS switches. In capacitive switches, reliability is limited by dielectric charging of the insulator layer. In DC contact switches, the reliability is affected by the metal contact used and by power handling capabilities. In the following section, an overview of charging and the methods to improve the reliability of capacitive switches and power handling capabilities for DC contact switches will be presented.

2.4.1   Dielectric Charging

Reliability of capacitive switches (low power) is reduced mainly due to the moveable membrane not releasing or coming back to the normal OFF state after the actuation voltage is removed. This failure is mainly due to stiction between the metal layer and the dielectric and is caused by charge accumulation due to injection and trapping inside the dielectric layer. Charge trapping has been studied extensively in the

CMOS industry for years for transistor applications. Many groups [26-29] in the RF-MEMS community have addressed this charging issue in multiple ways which deal with surface charging and bulk charging effects. Dielectric charging can be associated with stress which can be mechanical, electrical or thermal. Typically during charging, electrons are trapped at low electric fields and get released or de-trapped at high fields, but holes are typically observed only at high fields (~ 10 MV/cm). Apart from charge injection and trapping, the surface and interface of the dielectric layer and electrodes where defects are concentrated, will be areas for charge accumulation.

Figure 2.9 shows the schematic representation of an electrostatically actuated capacitive switch. At a certain voltage, the electrostatic force (F_E) becomes greater than the restoring spring force (F_{spring}) and causes the top plate to collapse. This voltage is called the pull-in-voltage (V_{pi}). (The pull-in voltage mentioned here is same as the threshold voltage discussed earlier.) Once actuated, the beam continues to stay in the bottom state until the applied voltage is lesser than the hold down voltage (V_{po}). When actatuated repeatedly there is net amount of charge injected into the dielectric and this effectively changes or shifts the pull-in and pull-out voltages by a margin. This shift in voltage, V_{shift} changes continuously, leading to the eventual failure of the switch.
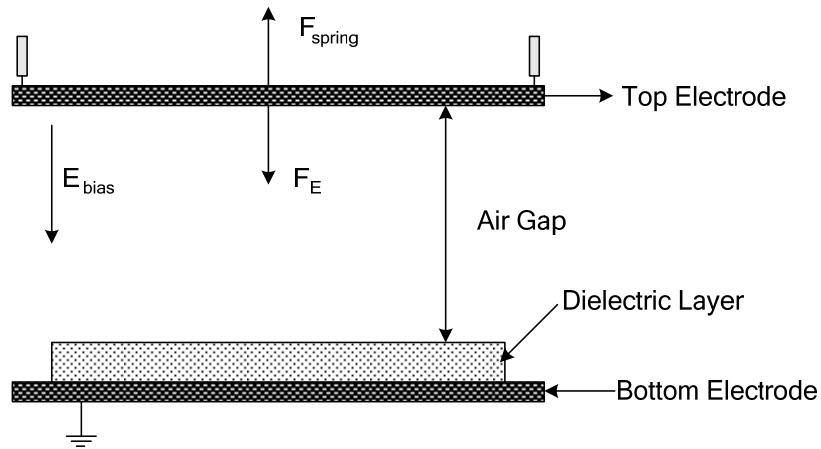
Figure 2.9 – Schematic Representation of the Actuation Mechanism in Capacitive RF-MEMS Switch

When the beam is actuated, the electric field in the dielectric layer is typically on the order of few Megavolts/cm. Because of this high electric field, charge is continuously

introduced into the dielectric layer thereby changing the electric field in the gap between the two electrodes and thus affecting the electrostatic force. A trapped charge in the dielectric layer results in image charges in the top and bottom electrodes i.e. if the trapped charges are +ve in the dielectric, that results in accumulation of −ve charges in the electrodes as shown in Figure 2.10. This reduces the total amount of charge on the electrode if a voltage is applied. This voltage shift will eventually change the net capacitance contributed by the switch. As reported by Reid, a uniform trap density of $10^{12}/cm^2$ is more than enough to cause a capacitive switch to fail in the actuated state. [7]
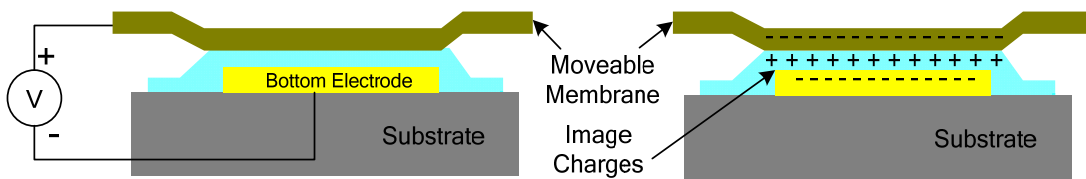
Figure 2.10 – Accumulation of Image Charges on the Electrodes During Actuation

Researchers from NXP semiconductors [30] have suggested two different techniques to study charge injection as a function of voltage and time. In the first technique, called the whole CV method, capacitance is measured in terms of voltage until the pull-in voltage. The shift in voltage is measured from successive CV curves measured during the actuation cycle. This technique is probably the oldest and the most well known method to evaluate the charging mechanism. In the second technique, the center shift method, only the shift in the center part of the CV curve is measured. Through this shift the voltage at the lowest capacitance value is calculated by fitting a parabola through the center of the curve. This technique is faster than the simple CV and successive approximation methods, and therefore has less influence on the device under test. There are modifications introduced into this technique wherein RF measurements and voltage shift is determined by manually tuning the bias voltage for measuring the capacitance.

Charging has also been studied by understanding the effects of dipolar and intrinsic space charge and interfacial polarization on the RF-MEMS switches. In this technique, charging is studied in contactless mode wherein the membrane is actuated at low voltages (6-8 volts). Polarization which is caused when an electric field is applied to

19

a dielectric layer is measured and the change in intrinsic polarization effects is monitored. This change in the polarization effects is directly related to the change in capacitance of the switch. Temperature dependent CV measurements were also performed to understand the amphoteric nature of the traps and its effects. Furthermore, a correlation between the method of deposition of the dielectric and the thickness of the dielectric in charging mechanism was deduced [31].

Apart from measuring MEM structures, researchers have analyzed the charging mechanism with switches intentionally fabricated in the down-state and on MIM structures. I-V and C-V measurements have been done to see the shift in leakage current and capacitance, respectively. In these measurements, the current measured from the I-V technique is comprised of the displacement current, trap charging current and steady state leakage current. The change in the leakage current and capacitance values have also been performed under stressed voltage and current conditions. The increasing voltage used in the stress testing causes defects in the dielectric layer, which lead to increased current and capacitance values [32].

The use of different dielectric materials to mitigate these charging issues has also been suggested by many research groups. PECVD silicon-dioxide has a lower trap density than silicon nitride films. Del Rio et al. [33] have demonstrated capacitive switches using alumina and zinc oxide alloys as the dielectric layer. The dielectric layer is deposited using atomic layer deposition (ALD) technique. The conformal growth of the dielectric layer makes it very reliable. Preliminary tests have shown that these films are capable of dissipating trapped charges and maximizing the ON state capacitance. Research groups from Sandia National Labs [34] and Purdue University [35] have suggested the use of amorphous and nanocrystalline diamond (NCD). Amorphous diamond films have been used in RF-MEMS switches and their non-charging behavior has also been reported. Nanocrystalline diamond is a very new film and little to no research has been done in using it as a dielectric film in capacitive switches. The complexity involved in the growth process and micromachining has made NCD related MEMS a rarity. But considerable improvements in micromachining techniques and the superior electrical and microwave properties is making NCD films attract lot of attention

in the RF-MEMS area. These charge leaky films provide a conductive path for the charges during actuation, thereby avoiding charge trapping and storage. In addition to these new films, carbon nanotube based RF MEMS switches [36] have been demonstrated. In these switches, double walled carbon nanotubes have been incorporated into the switch and the increased reliability due to the high density of the dielectric was demonstrated.

Another standard method to reduce charging is by using bipolar voltage when actuating the beams. By using this scheme the electrostatic force which is proportional to the applied voltage is maintained constant through the actuation process. Although this technique does not entirely remove charge injection into the dielectric, extended test results have shown switches having higher reliability through this technique.

Charging in RF-MEMS switches has been addressed by using a Schottky diode with a membrane and semiconductor in place of the usual dielectric layer. Pillans et al. [37] have demonstrated the use of Schottky barrier contact based RF-MEMS switch. In this switch, n^{++} InGaAs is used as the bottom electrode and epitaxial InAlAs is used as the dielectric layer. The entire switch was fabricated on an InP substrate, which facilitates direct integration with solid state devices. The switch operates as a normal RF-MEMS switch under reverse bias conditions and once the charges accumulate, the switch can be forward biased to effectively recombine any trapped charges. Figure 2.11 shows the top view of the fabricated Schottky switch.
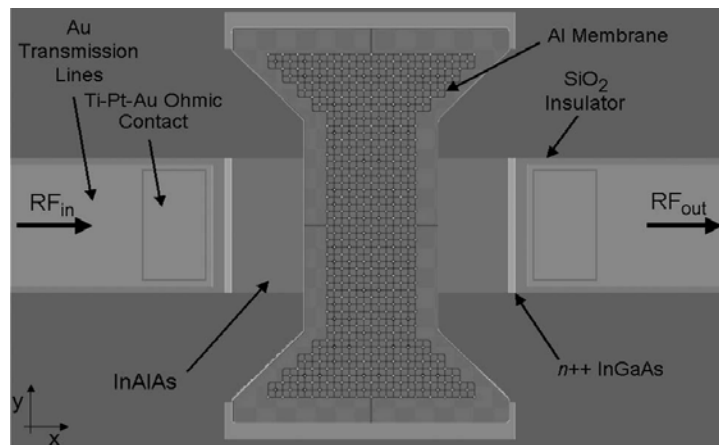
Figure 2.11 – Top View of the Fabricated Schottky Contact RF-MEMS Switch [37]

21

In addition to the above stated solutions, charging problems can also be reduced by using low voltage actuation schemes (thermal, magnetic and piezoelectric). Fabrication complexities and integration issues with these low voltage actuation techniques are being addressed to make them viable in future applications. Research groups have suggested alternative solutions [38-40] which deal with charging due to Frenkel-Poole conduction, mechanical deformation and choice of substrate. These methods as claimed by the authors tend to offer better results for charging related studies.

2.4.2   Contact Material Issues

In DC contact switches the most prevalent failure mechanism is the damage created in the contact area of the beam or the electrode as repeated actuation causes two metal surfaces to come in contact under low, medium or high power conditions. Damage can include pitting and hardening [7] of the metal at these contact areas. Over time the repeated contact also reduces the contact area, thereby increasing the contact resistance of the switch which is typically between 1-2 Ω under normal conditions. Over time, this value starts to increase and can become as large as 7-8 Ω. As demonstrated by researchers at Rockwell Science Center, reliability can be increased by controlling the actuation voltage in electrostatically actuated switches. By controlling the actuation voltage, the impact upon actuation can be reduced thereby reducing the pitting effects.

Upper Actuation Electrode   Upper Contact Electrode

Lower Actuation Electrode   Lower Contact Electrode
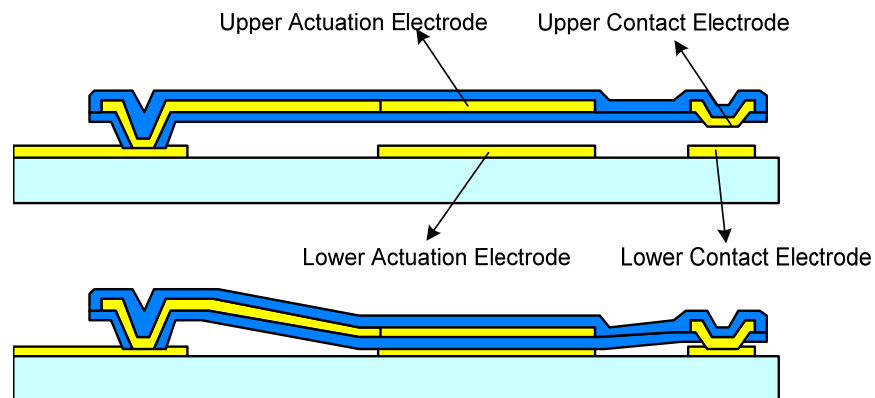
Figure 2.12 – Cross Section of DC Contact Switch in OFF and ON State [41]

Contact resistance can be controlled by the choice of material used in the fixed beams or cantilever structures. The contact material to be used is dependent on the force

required during the actuation scheme. Gold is the most common material used in RF-MEMS structures, particularly for low force designs, and the hardness of sputtered and electroplated gold is 3 GPa and 1 GPa, respectively [7,44]. For high contact force designs, apart from gold the other popular metals are rhenium and gold-palladium alloys. There is considerable interest among many to use doped NCD or diamond like carbon (DLC) in metal contacts. Although these materials are good choices because of their hardness, deposition of these materials on metals in low temperature conditions is still a challenge.

Other failure mechanisms in DC contact switches are related to humidity, contamination in contact areas and organic deposits after the fabrication process. Figure 2.13 (a and b) shows the SEM image of a fabricated tunable inductor. It is seen that there are organic deposits around the contact area of the beam; this contamination will result in the failure of the cantilever structure during actuation. Contamination related problems can be reduced by fabricating and packaging the switches in a clean environment.

(a)   (b)
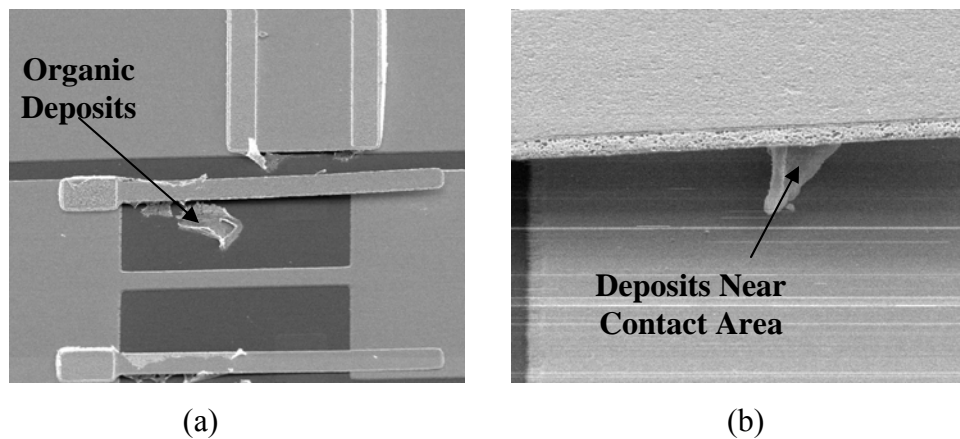
Figure 2.13 – SEM Image of DC Contact Switch with Organic Deposits

2.5   Power Handling Capabilities

Over the years the high power capability of RF-MEMS switches (DC or capacitive; shunt or series) has been limited by failures due to self actuation, electromigration, latching and Joule heating issues [42-44]. Although considerable research has gone into addressing this problem, the long term reliability of the switches under high power conditions is still an active area of study. At lower power levels

(milliwatts) under nitrogen ambience, dry air and vacuum conditions little to no difference in the number of cycles under hot or cold switching condition is typically observed [7]. Table 2.2 shows the list of the current state of art in high power testing for capacitive and DC contact switches [45-48].

Table 2.2 – State of Art in High Power RF-MEMS Switches

Research Group	Switch Type	Testing Conditions
Lincoln Labs	Capacitive	10 Watts cold switching & 1.7 Watts hot switching
Raytheon	Capacitive	4 Watts cold switching & 510 mW hot switching
Radant MEMS	DC Contact	10 Watts hot switching

The power handling capability of an RF-MEMS switch depends on the type of switch (DC contact or capacitive) and the configuration (series or shunt) in which it is fabricated. In most the cases electrostatic actuation is the preferred scheme for high power RF-MEMS switches. The DC actuation voltage (V_{act}) of a bridge can be given by [42]

$$V_{act} = \sqrt{\frac{8kg^3}{27\varepsilon_o A}} \qquad (2.6)$$

Where k is the spring constant, g is the initial height of the bridge and A is the area of cross section. An RF signal with a magnitude of V_O generates an equivalent DC voltage of

$$V_{eq} = \frac{V_O}{\sqrt{2}} \qquad (2.7)$$

And the equivalent input power can be evaluated in terms of the input voltage and the input impedance (Z_O)

$$P_{in} = \frac{V_O^2}{2Z_O} \qquad (2.8)$$

24

When the switch is the up-state, almost zero power gets reflected and the minimum power [42] to actuate or rather "self actuate" the switch can be given as shown in equation 2.9. This input power causes a force on the metallic plates and if this power is sufficiently high, the induced force will be large enough to self actuate the moveable membrane.

$$P_{act(\min)} = \frac{8kg^3}{27\varepsilon_O AZ_O}$$ (2.9)

Equations 2.6 – 2.9 apply for a shunt switch. For a series switch, the equivalent voltage (V_{eq}) is $2V_O$. Assuming the same area and spring constant, series capacitive switches are capable of handling $1/4^{th}$ of the power as the shunt switches. Recent improvements in designs have shown improvements for designs fabricated in the series configuration, too.

Another high power handling issue deals with the high current which is propagated in the moveable membrane and transmission under high power conditions. Electromigration [43] is defined as the movement of metal ions in a conductor upon an input electric current. The transmission lines can exhibit this effect, thereby lowering the conductivity of the material and increasing the overall loss (degrading performance) of the switch. Furthermore, high power levels in capacitive switches also lead to charging related issues which can cause the switch to fail.

In DC contact switches, the contact area typically dissipates 0.5 % of the incident power [1]. This dissipation can result in localized heating near or at the contact area. Localized heating can subsequently lead to increased contact resistance in the actuated state. The increase in contact resistance is due to the bilateral heat current [44] due to the high power. Therefore thermal conduction plays an important role in the stable operation and reliability of the switch. Thermal constriction conductance (W/K) [44] as shown in equation 2.10 is the ability of the contact to dissipate heat through the contact and it is dependent on the thermal conductivity of the material (k), the radius of the contact spot, and b the radius of the cathode.

$$G_{ct} = \left(R_{cd} \left(1 + F\left(\frac{a}{b}\right)^{-1} \right) \right)$$ (2.10)

where R_{cd} can be defined in terms of the thermal conductivity (k) and a

$$R_{cd} = \frac{1}{4ka} \qquad (2.11)$$

and
$$F\left(\frac{a}{b}\right) = 1 - 1.4098\left(a/b\right) + 0.3441\left(a/b\right)^3 \qquad (2.12)$$

As demonstrated by Hyman et al. [44] samples with large contact area and good thermal conductivity exhibit little change in contact resistance up to 50 mA, while switches fabricated with low thermal conductivity yield higher contact resistance at elevated current and power levels. Damage and material transfer also increase with contact force and current level which is the effect of heat conduction.

2.6   Summary

RF-MEMS switches of different types and configurations have been discussed. Lumped element circuit models and small signal simulations using Agilent's ADS for series and shunt type capacitive switches were presented. Different actuation schemes that include electrostatic, thermal, piezoelectric and magnetic along with their advantages and disadvantages have been discussed in detail. Charging which is the major reason in the failure of capacitive switches and the solutions to eliminate or mitigate this effect has been presented in detail. Similarly, reliability issues in DC contact switches that include material contamination and failure due to high power handling have been discussed. Although a multitude of solutions have been analyzed and presented, choosing the best method is cost and application dependent.

Chapter 3

Nanocrystalline Diamond – Properties, Growth and Characterization

3.1 Introduction

Micro-electro-mechanical devices (MEMS) have been fabricated on substrates that include silicon, quartz, and glass among others. But these devices are limited in applications which require reliability under high temperature and high power conditions. Furthermore, MEMS devices unlike integrated circuits (IC's) involve moveable components wherein the mechanical and tribological properties of silicon limit its application. Because of these limitations other materials such as SiC, GaN and diamond are now under investigation.

Diamond has been investigated for application to active devices such as field effective transistors (FET) for high power electronics as well as for tools used in grinding, polishing, cutting, and dicing. Diamond has the highest Young's modulus, hardness and thermal conductivity and it is transparent from the UV to far IR region. Furthermore, its superior electronic properties make it suitable for use in heat sinks, and radiation detectors [49]. Diamond is chemically inert, stable at high temperature (1000^0C in vacuum) and is suitable for operation in harsh environments (except oxygen ambience) [50]. Because of these characteristics diamond is a very good candidate for realizing reliable, high power and temperature-stable MEMS and microwave devices.

Table 3.1 [51, 52] compares the mechanical properties of NCD films with other materials used in microsystems technology. Along with positive mechanical attributes NCD possesses low loss when used as a thin film at microwave frequencies.

Table 3.1 – Mechanical Properties of NCD Thin Films in Comparison to Materials Used in Microsystems Technology

	Si	(3c)SiC	(6c) SiC	(h)GaN	Diamond
Bandgap (ev)	1.12	2.2	2.9	3.45	5.45
Break down field (10^6 V/cm)	0.5	4-6	3	3-6	10
Young's Modulus (Gpa)	170	450	-	390	1050
Fracture Strength (Gpa)	1.37	-	-	~2.5	10.3
Thermal Conductivity(W/cm.K)	1.47	4.9	4.9	1.3	22
Thermal Stability (^{0}C)	500	900	1300	650	1500

Thin film diamond can be classified into single crystal, microcrystalline (MCD), nanocrystalline (NCD) and ultrananocrystalline (UNCD) films. These films are grown on different substrates which is dependent on the respective application. In this chapter, discussions will be focused on the growth and characterization of NCD films. The popular techniques used to grow these thin films along with their chemistry of growth and seeding process will be discussed in detail. Finally, mechanical characteristics that include Young's modulus, mechanical resonance frequency and intrinsic stress of NCD films will be presented.

3.2   Structure and Growth of Nanocrsytalline Diamond (NCD)

Diamond has a face centered cubic crystal (FCC) lattice structure with a unique arrangement of carbon atoms with eight corner atoms, six face centered atoms and four other atoms from adjacent interpenetrating lattices offset by one-quarter of the body diagonal as shown in the ball and stick model of Figure 3.1 [53]. Each of the carbon atoms is covalently bonded to four nearest neighboring atoms by σ bonds resulting in a strong sp^3 character. The (111) planes of the diamond are along the bond direction with a lattice constant (a_0) of 3.567 Å and a bond length of 1.54 Å. Due to this unique chemical

bonding, and atomic density of 1.76×10^{23} cm^{-3}, diamonds possess several extraordinary material properties.
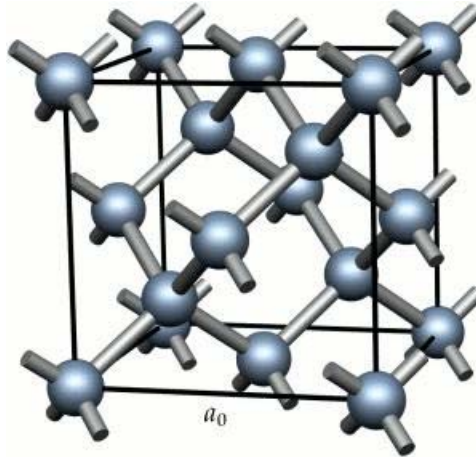
Figure 3.1 – Crystal Structure of Diamond Lattice [53]

Chemical vapor deposition (CVD) involves the dissociation of chemical species in a vapor phase to form a coating or a thin film. Thin film diamond is generally grown through a CVD process. The growth process in diamond films can be initiated by adding one carbon atom to its initial template. Subsequent addition of these carbon atoms result in a tetrahedron bonded carbon network. CVD growth process of a diamond film can be broken down into the following steps [54]:

- A gas phase must be activated, either by a high temperature (ex: hot-filament CVD) or by plasma excitation (ex: microwave CVD).
- The gas phase must contain carbon-containing species such as hydrocarbon, carbon dioxide or carbon monoxide.
- A sufficiently high concentration of atomic hydrogen to etch graphite and suppresses gaseous graphite precursors must be provided.
- The substrate must be seeded to initiate the nucleation and growth of diamond from the vapor phase.
- A driving force must exist to transport the carbon-containing species from the gas phase to the surface of the substrate. In most CVD methods, the temperature gradient acts as a driving force for the motion of diamond-producing species via diffusion.

Thin film NCD is grown through a chemical vapor deposition (CVD) process wherein the growth occurs by the decomposition of carbon containing precursor molecules (typically methane) in either a pure hydrogen, or hydrogen and argon environment. NCD growth is done through a thermal (hot filament) [55], plasma (microwave or RF) [56] activation or use of a combustion flame (oxyacetylene). Of the three, hot filament and microwave plasma methodologies are the most popular techniques used for thin film diamond growth.

Prior to diamond growth, the wafer needs to go through a seeding step which aids in the growth of the thin film. Seeding is popularly done through three different techniques:

- Mechanical polishing of the wafer: In this technique nanometer sized diamond powder is sprinkled on the silicon wafer and the wafer is mechanically scratched. By this the diamond powder is spread uniformly across the wafer and this acts as a seeding layer in the CVD system. Seeding through this method results in a nucleation density of $10^7 cm^{-2}$ [57].

- Ultrasonication: Here a silicon wafer is suspended in slurry of nanometer sized powder with acetone or methanol for 20-30 minutes. Through this process the surface of the wafer is damaged and seeded with the diamond powder for the subsequent growth process. Nucleation density of $10^6 - 10^{10}$ cm^{-2} is achieved through this method [58].

- Bias Enhanced Nucleation (BEN): Although the first two processes are popular and result in good diamond films, nucleation density is best in the BEN process [59]. In the microwave plasma enhanced CVD (MPECVD) process, prior to growth, in the BEN stage the substrate is negatively biased at around 250 volts resulting in a starting current value of 10mA. The current increases and saturates at 100mA (Figure 3.2) in a half hour seeding procedure, beyond which the current tends to decrease with time. Nucleation density achieved through this procedure is around $10^{15} cm^{-2}$.
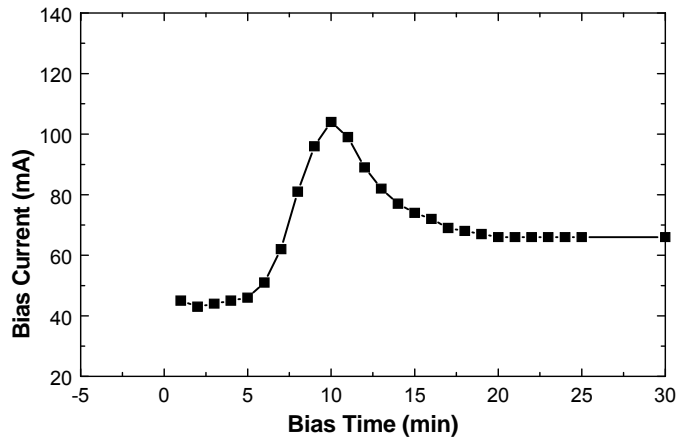
Figure 3.2 – Varying Current Value in Time During the BEN Process

In this work, diamond films grown by the hot filament (HFCVD) method are used in the MEMS actuators and the microwave plasma (MPECVD) films are used in the shunt switches. The growth recipes used at the University of Ulm (hydrogen chemistry) and at the University of South Florida (argon chemistry) for intrinsic NCD are given below:

Table 3.2 – Growth Recipe for NCD Films Using Hot Filament (HFCVD) and Microwave Plasma (MPECVD) Process

Growth Process	Gas Flow (sccm)			Total Pressure (Torr)	Substrate Temp. (^{0}C)	Power (kW)
	Ar	H_2	CH_4			
Hot Filament CVD (HFCVD)	–	200	3	12 – 15	850	2.4 – 2.8
Microwave Plasma CVD (Ulm MPECVD)	–	400 – 500	4 – 8	15	800 – 850	2.4
Microwave Plasma CVD (USF MPECVD)	788	8	4	135	725	1.8

Diamond films grown in the HFCVD technique use bias enhanced nucleation (BEN) as the seeding method. The HFCVD technique is based on the heating of metal filaments up to 2000°-2200°C in order to break molecular hydrogen and carbon compounds and to form C_yH_x free radicals; these free radicals move toward the substrate by a temperature gradient. On the substrate surface both diamond (sp^3) and graphite (sp^2) bonds are formed; the graphite bonds are etched by atomic hydrogen allowing diamond growth on the substrate surface. Figure 3.3 shows the SEM image of a diamond film grown in the HFCVD reactor.
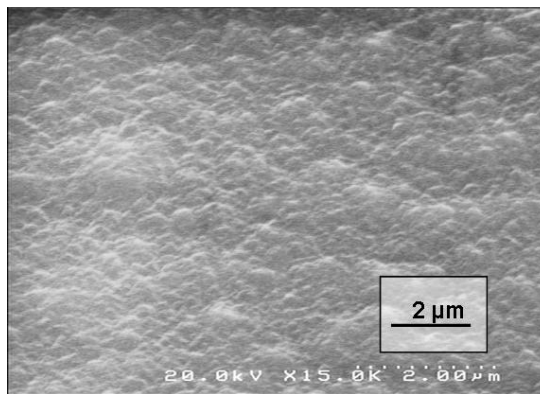
Figure 3.3 – SEM Image of a NCD Film Grown by the HFCVD Technique

In the MPECVD technique, a C_2 dimer-based growth mechanism that would result in nanocrystalline structure was proposed [60]. In the films deposited using 5% CH_4 and 95% Ar, the C_2 dimers resulted in the inclusion of an amorphous carbon or graphitic carbon [61]. Such non-diamond forms of carbon are due to the homogenous nucleation resulting from a high ratio of hydrocarbon to carbon dimers. But on the other hand, during the deposition of nano-diamond films, the heterogeneous nucleation rate ($>10^{10}\,cm^2sec^{-1}$) increases due to highly reactive C_2 species, resulting in the smaller grain size of the diamond films [63]. According to the proposed model, the feed gases methane and argon disassociate and favor the formation of $(C_2H_2)^+$ at a low ionization potential. The positively charged acetylene radical attracts an electron to form a highly reactive carbon dimer and hydrogen. Hydrogen is then desorbed away while the carbon dimers nucleate at the reconstructed surface. As the reaction continues, the number of carbon

dimers in the plasma increases and they join the previously hybridized carbon atoms. In this way, a closely hybridized sp^3 network of carbon atoms forms a continuous film of nanocrystalline diamond.

The limited applications of microcrystalline diamond (MCD) films have been surpassed by synthesizing a new class of material known as "nanocrystalline diamond" (NCD) films. The nanocrystalline diamond films can be grown by altering the CVD process [64, 65]. Unlike MCD, NCD films consist of small grains on the order of 20-50 nm and a low surface roughness of ~20 nm. Recently, "ultra-nanocrystalline diamond" (UNCD) films having smaller grain size (3-5 nm) than NCD have been developed [66]. The growth of NCD/UNCD films opened wide windows of applications ranging from tribology, MEMS, optics, RF applications and field emission devices [67-69]. Typically, MCD films are deposited in CH_4 (1%)/H_2 (99%), NCD films are deposited in CH_4 (1%)/Ar (98%)/ H_2 (1%) and UNCD films are deposited in CH_4 (1%)/Ar (99%) gas chemistries. Microcrystalline diamond films consist of large grains (grain size: ~ 5-10 μm) and rough surfaces (mean surface roughness: ~ 300-700 nm) thereby limiting their application to cutting tools, abrasive coatings and heat sinks [14-16].

The intrinsic diamond films are electrically insulating with resistivity on the order of 10^{13}- 10^{16} ohm-cm. Electrical conductivity can be achieved by doping the films during the deposition. The diffusion of dopants into the diamond films is not a practical method of doping as the surface is not diffusive to most of the impurities. Though there are a few reports on the ion-implantation of diamond films [70], it is an expensive technique and can damage the surface. Therefore, dopants such as boron (p-type), nitrogen, phosphorous and sulphur (n-type) are incorporated in the gas chemistry during the growth [71]. The most widely used dopants are boron (p- type) and nitrogen (n-type), as these are readily soluble with diamond. It was observed that the quality of the films improve with the incorporation of trace amounts of boron by reducing the point defects. But excess concentration of boron promotes graphitization due to the incorporation of boron interstitial sites. In the case of single crystal or microcrystalline diamond, p-type conductivity can be easily achieved. But, it is difficult to obtain n-type conductivity at room temperature in these films as nitrogen forms a deep donor (~1.7 eV). Nitrogen

forms a shallow donor level (~ 0.4 eV) [72] in NCD/UNCD films and results in high n-type conductivity (~143 Ω^{-1} cm^{-1}). The drastic reduction in the grain size of the diamond films from several microns to few nanometers by changing the gas chemistry suggests that the growth mechanism of nanocrystalline diamond films is different from conventional CVD diamond films. Boron is the most common and preferred p-dopant and the doping mechanism are well established both in the HFCVD and MPECVD techniques [73]. Nitrogen doped diamond films are available using MPECVD technique whereas HFCVD films with nitrogen doping are still in the process of being matured.

3.3   Characterization Techniques for NCD Films

Unlike the microcrystalline diamond films, NCD films deposited in hydrogen poor gas chemistry have a complex grain boundary structure with grain size on the order of few nanometers. These differences in the grain structure result in different mechanical and electrical properties of NCD films. The structural, mechanical and electrical properties of these films have been studied by several analytical and metrology techniques.

Scanning electron microscopy (SEM) has been a very useful technique in the characterization of diamond thin films. The microstructure of diamond films changes dramatically with the continued addition of Ar to reacting gas mixtures during CVD process. The transition from micro- to nanocrystalline by systematically adding argon to hydrogen-rich plasma has been characterized by SEM micrographs as a function of argon content shown in Figure 3.4. Different combinations of gas mixtures have been used.

<div align="center">(a)   (b)</div>
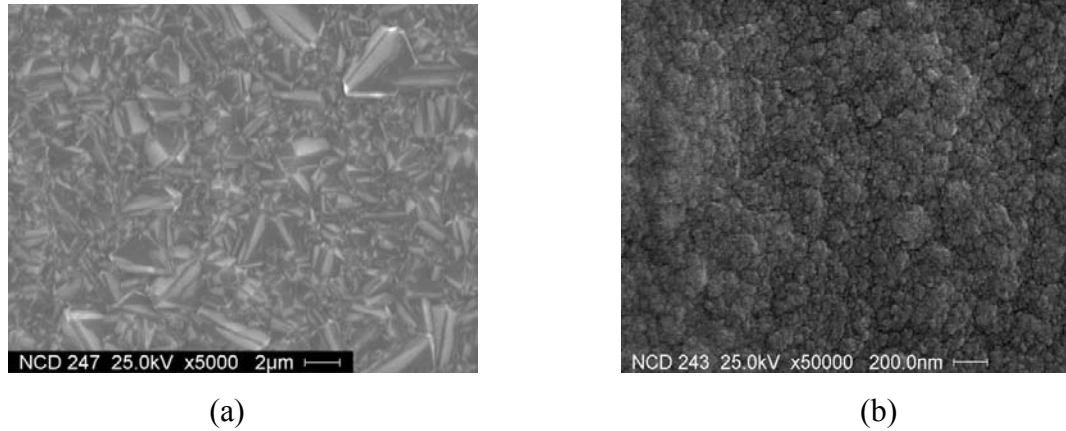
Figure 3.4 – SEM Images of Diamond Films Grown with Different Ar Ratios (a) 50% and (b) 98%

Raman spectroscopy [74] is a powerful technique to determine the chemical and structural properties of liquid or solid materials by a simple non-destructive and non-contact method of measurement. In the case of Raman spectroscopy of carbon based materials, the scattering is about 50 times more sensitive to π-bonded amorphous carbon and graphite than to the phonon band of diamond. Hence, this method can be used to establish the crystalline quality of diamond thin films by estimating the amount of sp^2 bonded carbon in the films. Lin et al. [75] performed the analysis of diamond films grown with $Ar/CH_4/H_2$ plasmas with different gas mixtures. For films grown without Ar, a sharp diamond characteristic peak is observed at 1332 cm^{-1}. No scattering can be found in the range from 1400 to 1600 cm^{-1} suggesting that the diamond film contains very little sp^2 bonded carbon. With addition of argon to the reactant gas up to 92%, a sharp diamond peak still exists indicating the presence of microcrystalline diamond grains. The typical spectrum of a single crystal diamond, highly ordered pyrolytic graphite (HOPG), microcrystalline diamond and nanocrystalline diamond are shown in Figure 5 (a-d) respectively. Apart from Raman spectroscopy, near edge X-ray absorption fine structure (NEXAFS) is another popular technique for characterizing diamond films. This technique is used in identifying the percentage of sp^2 and $sp3^3$ bonded carbon in the thin film.
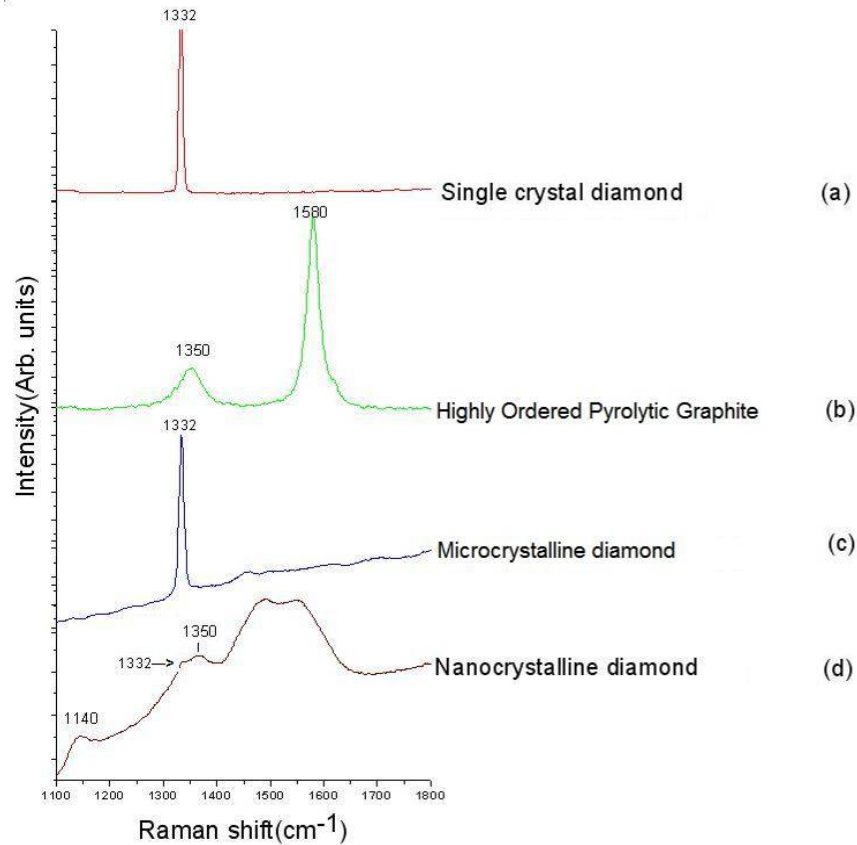
Figure 3.5 – Raman Spectra of Carbon Based Materials [54]

3.4   Mechanical Characteristics of NCD Films

In order to improve the reliability of micromachined devices, it its very important to understand the mechanical properties of the thin film used to fabricate them. Amongst others, Young's modulus, intrinsic stress and the parameters affecting it, and fracture strength determine the performance of the devices. In this section, the different characterization techniques used to measure these properties will be discussed in detail.

3.4.1   Young's Modulus

According to solid mechanics, Young's modulus (E) is a measure of the stiffness of an isotopic elastic material [76]. It is defined as the ratio of the uniaxial stress over uniaxial strain in the range of stress in which the Hooke's law is valid. In electrostatically actuated RF-MEMS switches, the actuation or threshold voltage is dependent on the spring constant of the material. For thin, long cantilevers with small air gaps, the spring

constant is associated with a small reset force which in turn affects the release of the structure when switched off. Under such circumstances, it is preferable to use a stiff material with a high Young's modulus. Stiction of the moveable membrane due to dielectric charging in capacitive switches can be mitigated by using such stiff material. Theoretically, diamond possesses the highest Young's modulus among all solid materials. The values of 1150 GPa and 960 GPa have been reported for NCD and UNCD films, respectively [77]. Furthermore, the Young's modulus of diamond is very stable at elevated temperature (700^{0}C) which makes it far superior to other materials.

Young's modulus can be measured using different techniques and in this work it is determined by cantilever resonance measurements [77]. In this technique, diamond cantilevers of different lengths and widths are fabricated and the first order mechanical resonant frequency is measured using a piezo oscillator. First, boron doped NCD film is grown on a low resistive silicon substrate to a thickness of 1.2 μm. Titanium is patterned and used as a hard mask to etch the NCD film. Diamond is then etched in a RIE system and subsequently released by etching the silicon layer by CF_4 plasma. The entire wafer is then diced wherein individual diamond cantilevers with varying lengths are stuck to a commercially available piezo crystal oscillator using epoxy. Figure 3.6 (a) shows the SEM image of the diamond cantilevers of different lengths grown in the HFCVD technique and Figure 3.6 (b) shows the SEM image of the released diamond cantilever grown in the MPECVD technique. It is evident from these SEM images, that films grown using both techniques have an intrinsic stress that builds up during the growth process.
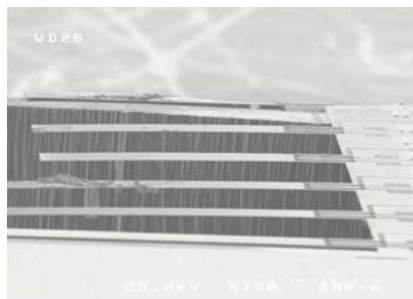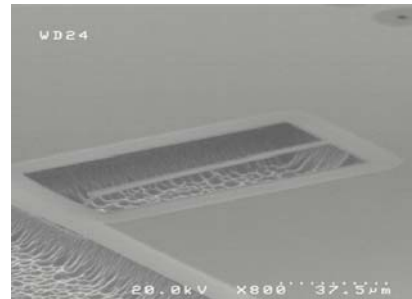
(a)   (b)

Figure 3.6 – SEM Image of Released Diamond Cantilever (a) Using HFCVD, and (b) Using MPECVD Technique

37

A function generator is used to measure the first order mechanical resonant frequency. The released diamond cantilevers are attached to a commercial piezo crystal which is in turn connected to the function generator. The first order resonant frequency is observed through a microscope as the tip of the cantilever starts to vibrate at the highest center frequency value. The mechanical resonant frequency is dependent on the length and width of the structure and on the thickness of the film and can be evaluated given in equation 3.1 [77]

$$F_{RES} = \frac{\lambda_i^2}{4 * \pi} * \sqrt{\frac{E}{3 * \rho}} * \frac{t}{L^2}$$

(3.1)

In this experiment, the measured resonant frequency is used to evaluate the Young's modulus of the diamond film. Table 3.2 gives the details of the measured resonant frequency and evaluated Young's modulus for cantilevers whose width is 40 μm and thickness is 1.2 μm.

Table 3.3 – Measured Resonance Frequency and Young's Modulus for Diamond Cantilevers

Length of Cantilever	Measured Resonant Frequency	Young's Modulus from Measurement
100 μm	326 KHz	1015 GPa
300 μm	82 KHz	1010 Gpa

3.4.2 Intrinsic Stress

Reliable MEMS devices can be fabricated by understanding the stress conditions that develop during the deposition (sputtering, evaporation and CVD) process. Stress in NCD films can vary widely (-500MPa to + 700 MPa) depending on the growth parameters that include pressure, substrate temperature and gas ratio. There are various techniques which are available to measure the compressive and tensile stress in the film [78-80]. In this work, the rotation tips are used to measure the compressive stress in NCD films wherein the strain is converted into a rotation angle which is directly proportional to the strain caused in the material. Although this technique can be used for measuring both

kinds of stresses (tensile and compressive), our discussion is only focused on compressively-stressed NCD structures. Measured values show compressive stress ranging from 140 MPa to 557 MPa for a 1.2 μm thick film is measured. Figure 3.7 shows the SEM images of the rotation tip structures used for measuring the stress.
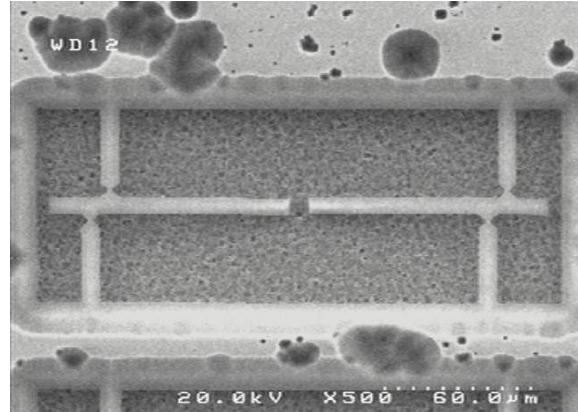
Figure 3.7 – Released Structures Used for Measuring the Intrinsic Stress in Diamond Films

Micromachined structures tend to elongate or shorten depending on the stress which builds up during the growth process. The cantilever structures studied in this work are compressively stressed resulting in an elongation of the short beams upon release. This elongation on either side causes the beam to change its angle (rotation). The difference in the distance between the two long beams is used to evaluate the strain using equation 3.2 [80]. Considering the rotational points to be ideal, the structure can be represented as shown in Figure 3.8. As shown in the figure, L_A and L_B correspond to the length of the stationary beam, L_C is the length of the moveable beam, W is the width of the moveable beam O is the distance between the turning points.
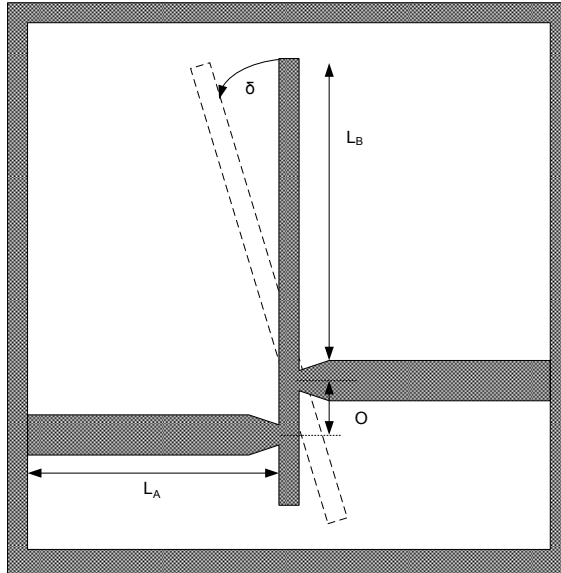
Figure 3.8 – Cantilever Structure Used to Evaluate Intrinsic Stress

Figure 3.9 shows the geometry used to calculate the rotation angle for measuring the strain in the film. Equation 3.2 is used to evaluate the strain with respect to the stationary arm. This equation is derived under the assumption that the width of the moveable arms is much smaller than the stationary arms (L_A and L_B).

$$\varepsilon^{''} = \frac{O*\tan(\alpha)}{(L_A + L_B)} \tag{3.2}$$
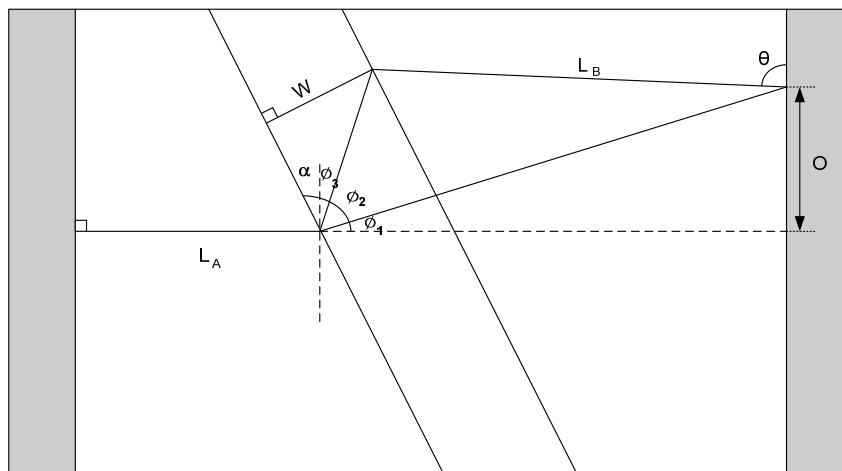
Figure 3.9 – Geometry Used to Evaluate the Rotation Angle to Calculate Strain ($\varepsilon^{''}$)

The deflection caused by the moveable arm L_C can be defined in terms of the rotation angle as shown in equation 3.3.

$$\tan(\alpha) = \frac{y}{L_C + \frac{1}{2}O}$$ (3.3)

From equations 3.2 and 3.3, the overall strain can be represented in terms of the deflection as shown in equation 3.4

$$\varepsilon = \frac{O * y}{(L_A + L_B) * \left(L_C + \frac{1}{2}O\right)}$$ (3.4)

Figure 3.10 shows the SEM image of the moveable arms which have vertical displacement due to the compressive stress in the growth process.
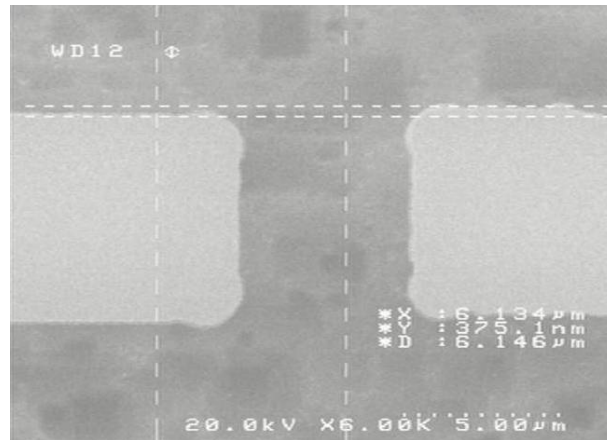
Figure 3.10 – SEM Image of the Released Cantilevers with Intrinsic Stress

This equation, which shows the linear relationship between strain and deflection, can be used for both tensile and compressive stress measurements. The only limitation with this technique is that the distance between the turning points (O) must be not smaller than a value which results in stiffness that thwarts the movement of the arms. Table 3.3 shows the measured stress value (as a function of strain) of a 1.2 μm intrinsic diamond film for various lengths of the stationary and moveable arms. The Young's modulus for these measurements is assumed to be ~ 1020 GPa.

Table 3.4 – Measured Intrinsic Stress of a 1.2 μm NCD Film

L_A & L_B (μm)	L_C (μm)	O (μm)	2Y (μm)	Stress ($\varepsilon^{'}$) MPa
33	76	8.27	0.305	243
33	76	8.27	0.35	279
50	95	11	0.51	285
50	95	11	0.47	262

Stress during the growth process is dependent on many parameters like pressure, temperature and gas mixture ratio. In the HFCVD technique, films with high compressive stress can be achieved at higher pressure and temperature. Although a thorough mathematical model cannot be derived, Figure 3.11 shows the compressive stress that can be achieved with varying temperature and pressure conditions. Furthermore, stress distribution is generally uniform over a 1 inch radius of a 4 inch wafer. The uniformity in the stress distribution is a direct result of the homogeneity of the diamond film during the growth process. Figure 3.12 shows the stress distribution in the diamond film for a 4 inch wafer.
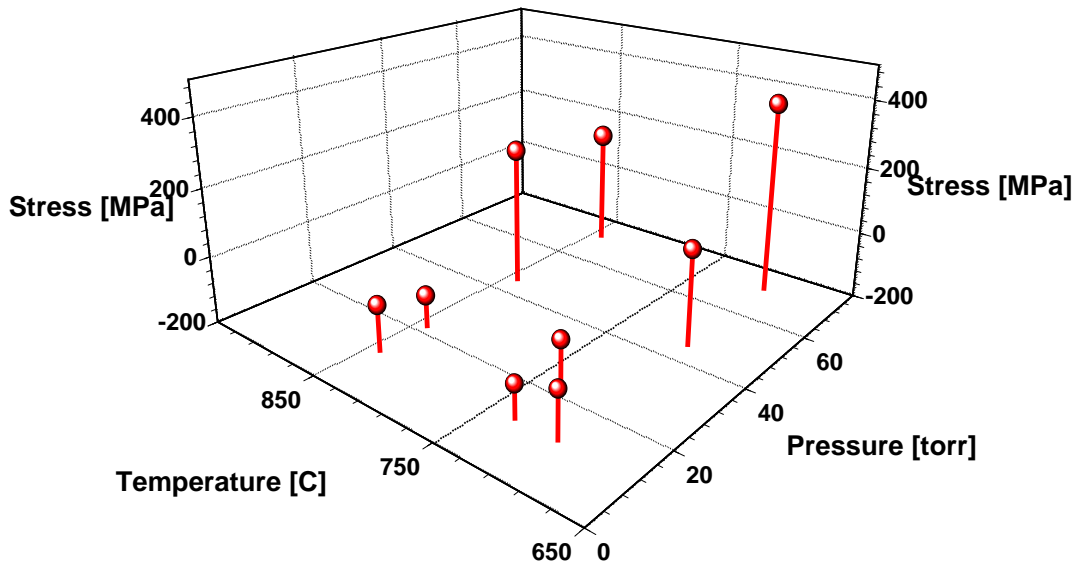
Figure 3.11 – Measured Intrinsic Stress with Varying Temperature and Pressure Conditions

42
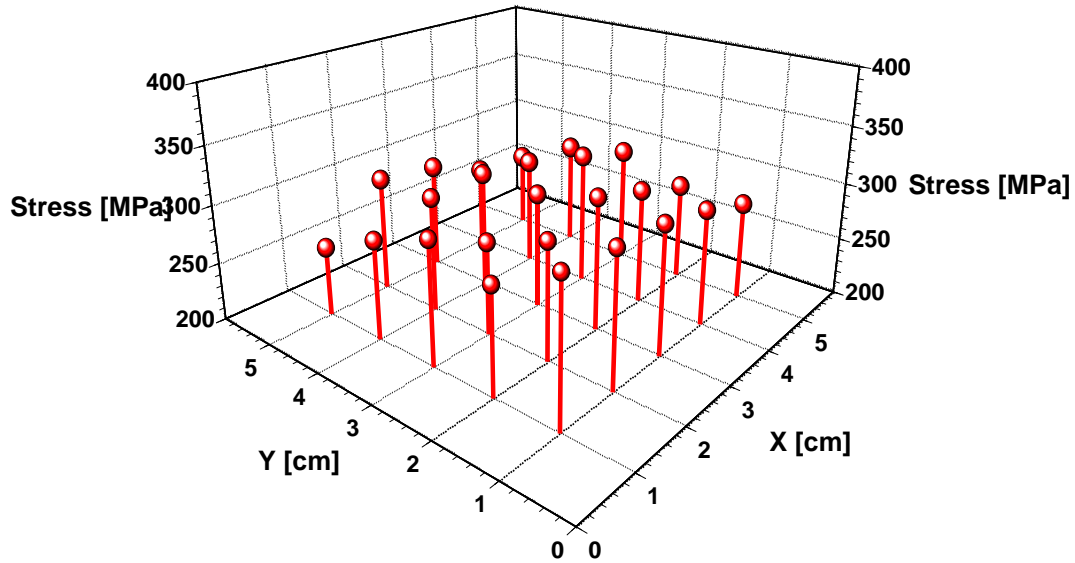
Figure 3.12 – Measured Compressive Distribution Across a 4-inch Wafer

3.5   Summary

Growth of NCD films using MPECVD and HFCVD techniques has been presented. The effect of using different seeding techniques on the quality of the diamond films have been presented with examples. The growth process involved in diamond films using hydrogen and argon chemistry has been discussed in detail. Mechanical properties of the diamond films that include Young's modulus, mechanical resonant and intrinsic stress have been measured. Furthermore, the effect of process parameters (temperature, gas ratio and pressure) on the mechanical properties of NCD films was described with a mathematical model wherein intrinsic stress measurements and the factors affecting this intrinsic stress were studied in detail.

Chapter 4

Thermal and Dual Actuation Nanocrystalline Diamond Bridges and Cantilevers

4.1 Introduction

Radio frequency micro-electro mechanical systems (RF-MEMS) technology has been growing rapidly in the last few years and has found a multitude of applications in the automotive, defence and communication industries. Due to their outstanding properties and excellent performance at high frequencies, RF-MEMS devices have started replacing their solid state counterparts in filters [81], phase shifters [82] and antennas [83]. According to a 2006 market study, the global market for MEMS, with RF-MEMS being a major part will reach $12 billion by 2010 [84]. Although they are small in size and exhibit low parasitic losses, the monolithic configuration confines the device to a substrate common to the entire system. Furthermore, power handling [38] capabilities of RF-MEMS devices have been limited due to using all metal structures in the devices. Diamond has long been used in active devices such as FETS for high power electronics [85]. Also its stability under high temperature makes it a very good candidate for realizing reliable, high power and temperature stable RF-MEMS and microwave devices. The outstanding mechanical properties of nanocrystalline diamond (NCD) thin films and its low loss at microwave frequencies can be used to produce mechanically stable and high power RF-MEMS devices

In this chapter, the life cycle of a thermally actuated NCD bridges and cantilevers will be presented. The diamond actuators are designed to operate in a bi-stable mode. Design equations realizing the thermal actuation scheme and simulation results which facilitate the bi-stable operation will be discussed. The overall design of the actuator and the choice of material will also presented. Fabrication steps along with the solid-liquid interdiffusion (SOLID) process used for integrating the actuator will be discussed in detail. Small signal measurements are carried out in the frequency range of 1-30 GHz and

compared with the simulation results, which are performed using Agilent's *Advanced Design System* (ADS). Finally, high power measurements of the switch integrated in the microstrip topology will be presented. In addition to thermally actuated switches, a dual mode switch which combines thermal and electrostatic actuation schemes is also discussed. The fabrication and measurement results of this switch are also presented.

4.2   Design of the NCD Actuator

The NCD actuator is made of boron doped diamond film which is grown through a hot filament CVD process. Figure 4.1 shows the design of the NCD actuator. The diamond bridge is 1200μm long, 300μm wide and 1.5μm thick. The diamond film used in the actuator is grown to purposefully achieve compressive stress of ~ +300 Mpa. The parameters involved in achieving these stress values have been discussed in Chapter 3. The resistivity of the boron doped NCD film is ~ 1mΩ-cm. In addition to the fixed-fixed bridges, NCD based cantilevers (500μm, 1000μm in length) were also designed.
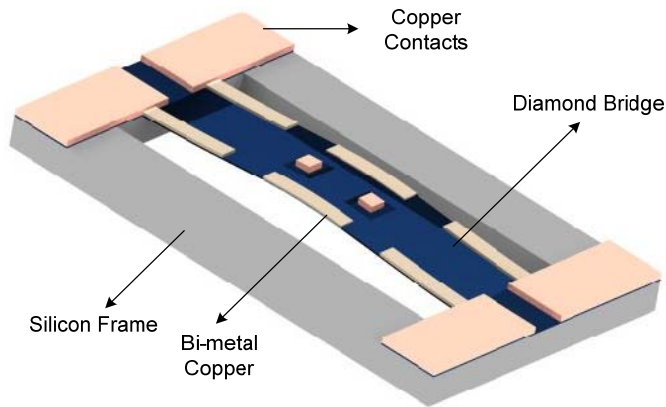
Figure 4.1 – Design of the Thermally Actuated NCD Bridge

The bridges are thermally actuated using a bi-metal actuation scheme [86]. Compared to electrostatic actuation, thermal actuation has the advantage of having a lower actuation voltage and a higher contact force. The main drawback of thermal actuation is the static power consumption, which can be avoided by using a designing the actuator to operate in a bi-stable mode. Copper which is used to facilitate the thermal actuation scheme is deposited on top of the doped diamond thin film. In addition to the

actuation pads, copper is also used in the contact pads of the actuator. The difference in the coefficient of thermal expansion between the two materials ($0.8\cdot10^{-6}$/K for diamond and $13\cdot10^{-6}$/K for copper) results in resistive heating of the doped areas. This resistive heating effect causes the diamond actuator to bend thereby switching to the actuated state. . The pull-in voltage (and current) to switch the bridge depends on the geometry of the diamond heating elements.

Figure 4.2 (a) and Figure 4.2 (b) show the top view of the different actuator designs. These designs were optimized in ANSYS^{TM} to achieve the best performance in terms of bending moment, deflection and ease of integration. Gold wirings are included in the design to provide a DC electrical path to the contact pad at the center of the diamond bridge. The contact pads are 100 μm x 100 μm in dimension.
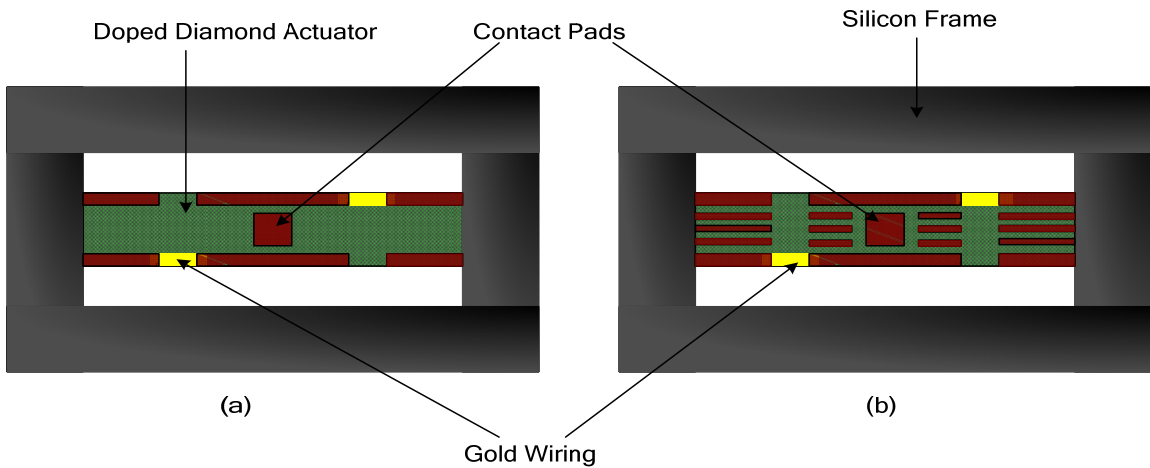
Figure 4.2 – Top View of the Diamond Actuator with Different Copper Heating Elements

As explained in Chapter 3, the buckling effect in the beam is obtained by optimizing pressure, gas composition and temperature during the NCD growth. This buckling effect can also be explained through a mathematical formula. According to theory of beam mechanics analysis, a straight beam can be axially compressed to yield buckled stable positions depending on the nature (axial or lateral) and position (extreme or center) of the load. A straight beam which is subjected to an axial load p can be represented as [79]

$$EI\frac{d^4w}{dx^4} + p\frac{d^2w}{dx^2} = 0 \qquad (4.1)$$

where w is the lateral displacement of the beam, E is the Young's modulus of the beam, and I is the moment of inertia of the beam. By assuming fixed boundary conditions at both ends and normalizing the axial force equation 4.1 can be represented as

$$w = A\sin\left(\frac{Nx}{l}\right) + B\cos\left(\frac{Nx}{l}\right) + Cx + D \qquad (4.2)$$

where A, B, C and D are constants. The compressive force generated can be categorized into various modes and the buckling caused in the beam can vary depending on the force generated (F) at each mode. Initially, the beam is straight, if the compressive energy (E_C) generated is less than beam bending energy (E_{BB}). As the compressive force changes (F=F_1), E_{BB} is greater than E_C, and this results in buckling of the beam. The buckling effect in the first mode increases the overall length of the beam thereby lowering the compressive force. Figure 4.3 shows this buckling effect of the beam.
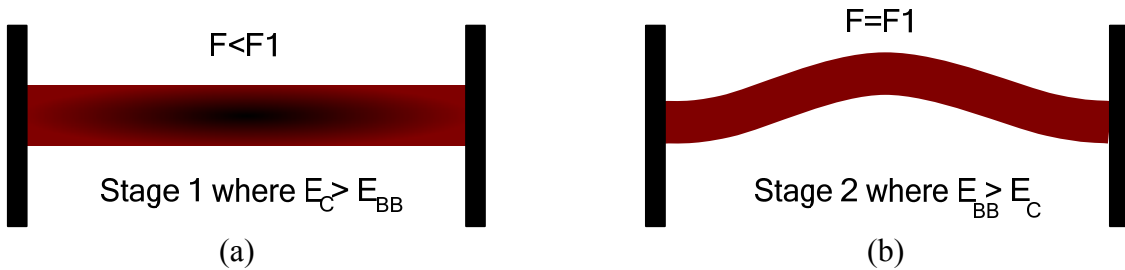
Figure 4.3 – Stages in a Straight Beam which is Compressively Stressed (a) E_C is Greater than E_{BB} and (b) E_{BB} is Greater than E_C

Mechanical simulations were performed in ANSYS^{TM} to optimize the length of the beam to achieve the bi-stable condition. Figure 4.4 shows the simulated contact force for double anchored cantilevers of different lengths versus the separation distance between the actuator and integrated substrate.
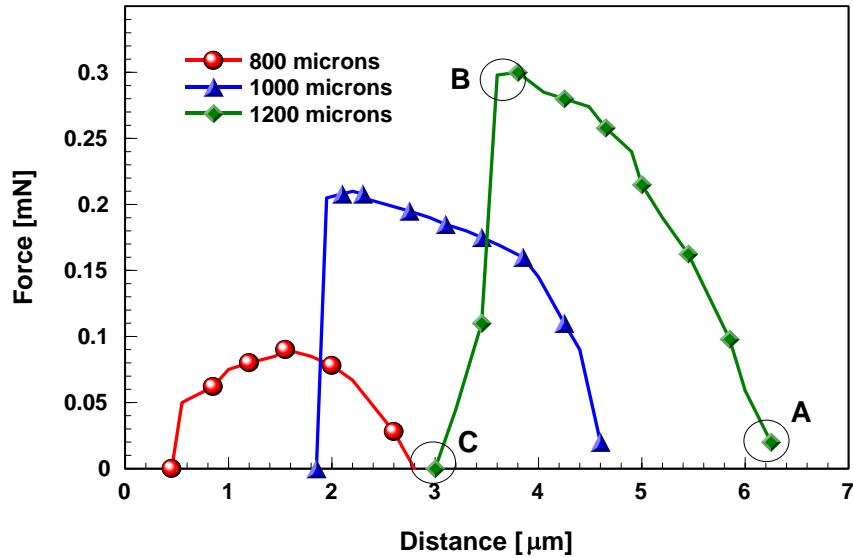
Figure 4.4 – Simulated Force vs Distance of Separation Between Actuator and Host Substrate

Many aspects have to be taken into account while designing the bridge. Intrinsic stress, thickness of the diamond layer and the length of the beam determine the buckling effect. Furthermore, these parameters together with the separation between the beam and the base plate influence the magnitude of the force, which is generated against the base plate. At the point A (near 6 μm), the force is zero, since the beam is completely released and just touches the base plate. When the separation is reduced, the cantilever is in contact and generates a center force on the base plate. This force increases with decreasing separation and reaches a maximum, at 3.4 μm (point B), before it drops immediately back to zero. At point C (~ 3 μm) the beam can no longer reach the lower stable state; the beam flips back and becomes mono-stable. For very long beams the center force decreases steadily from its maximum, because an s-shaped quasi-stable interstate appears before it becomes mono-stable. Although both 1000μm and 1200 μm long beams gave satisfactory results, the longer beam was chosen to accommodate the copper heating elements for better actuation. In thermal actuation, the amount of thermal expansion for a material can be given by

48

$$\varepsilon_{th} = \int_{T0}^{T1} \alpha_{th}(v)dv \qquad (4.3)$$

where T0 and T1 are the lower and upper temperature limit respectively, and α_{th} is the coefficient of thermal expansion. The expansion ε_{th} and the strain produced varies as a function of temperature wherein ΔT is the change in temperature, σ_x is the stress and E is the Young's modulus. ε_{th} and strain ($\varepsilon^{"}$) can be represented as

$$\varepsilon_{th} = \frac{\Delta l}{l} = \alpha_{th} * \Delta T \qquad (4.4)$$

$$\varepsilon^{"} = \frac{\sigma_x}{E} \qquad (4.5)$$

In the bridge or cantilever structure, the generated thermal strains in both materials (NCD and copper) are converted into intrinsic stress leading to a bending moment. This in turn leads to the deflection of the actuator. According to Hooke's law [87], stiff materials that possess high Young's modulus lead to high stress values. For this a proper figure of merit for thermal stress generation is the product of E and α_{th}. Upon heating, the bending moment caused by the material is dependent on its Young's modulus (E), thickness, length and width. To achieve the maximum bending moment the product of the E and α_{th} of NCD should be different (lower or higher) than the other material. Table 4.1 shows the E, α_{th} and their product for different materials as compared to that of NCD. It is seen from this table that a combination of copper and NCD is nearly ideal for the thermal actuation scheme, second only to the copper-Ni combination.

Table 4.1 – Comparison of Young's Modulus (E) and Coefficient of Thermal Expansion (α_{th}) for Different Materials

Property	NCD	Cu	Ni	Au	Al
Young's Modulus [GPa]	1050	130	210	78	70
CTE (α_{th}) [ppm/C]	0.85	17	13	14	23
E*α_{th}	840	2210	2730	1092	1610

In the first iteration of the design, nickel was used as the heating element. Although the product of E and α_{th} is higher in nickel than copper, Cu was preferred for because fewer fabrication steps are required and the integration process is simplified. Figure 4.5 show the operation of the actuator in the down-state and up-state, respectively. The up and down movement of the actuator is dependent on the heating of the individual copper heating element placed on top of the doped diamond film. The corner two blocks are used to push the bridge down and the center block is used to bring the bridge back to the up-state. As mentioned earlier, the actuator is designed to be bi-stable, and hence the design must accommodate heating elements for transforming the bridge between both states.
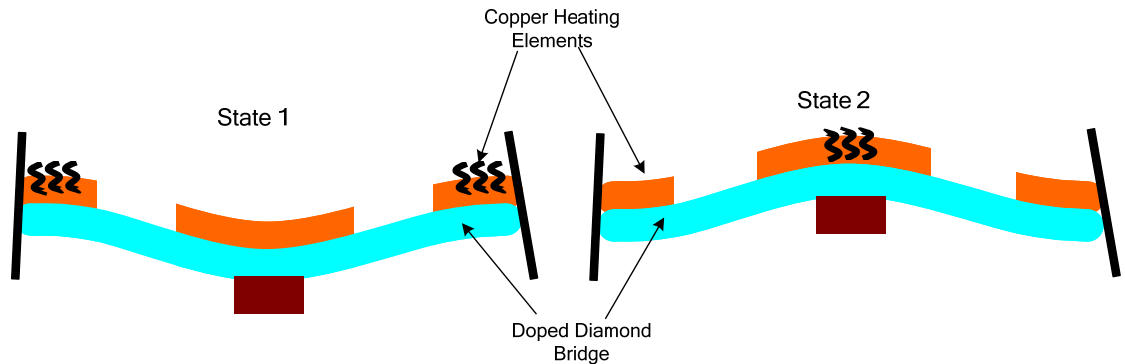
Figure 4.5 – Bi-Stable Layout of the Actuator with Individual Copper Heating Elements

4.3 Fabrication

The diamond bridges are fabricated on a 500 μm thick low resistivity silicon wafer. Prior to the 2nd generation design a diamond actuator was fabricated in which the bridge was composed of intrinsic diamond with areas of selectively grown doped diamond. The doped diamond bridge was chosen so that resistance of the heaters can be lower without actually making the bridge thicker and stiffer. Furthermore, the first generation switches included nickel to facilitate the thermal actuation scheme. The fabrication steps as shown in Figure 4.6 are as follows:

- The silicon wafer is nucleated by BEN (bias enhanced nucleation) and an intrinsic diamond layer of 1500Å thickness is grown through a microwave plasma assisted CVD process. Boron doped diamond (p-type) is later grown

with HFCVD (hot filament CVD) to a thickness of 8500 Å. This boron doped diamond is the heart of the micromachined actuator.

- Intrinsic diamond is selectively grown using a SiO_2 mask. The 4000 Å thick diamond layer is used for electrical isolation of the contact areas while actuating the bridges.

- A Cr/Au seed layer of 700Å is deposited using an ion beam reactor after which a 1 μm thick copper film is deposited by electroplating to serve as the bi-metal for thermal actuation.

- Copper pads which are used to integrate the diamond switches onto the host substrate are electroplated to a thickness of 12μm. The RF contact areas are also formed by electroplating in this step.

- The previously deposited seed layer is patterned to provide electrical continuity to actuate the bridges.

- 400 Å of platinum is patterned over the copper contact area using lift-off technique.

- Diamond bridges are then etched in a RIE system using titanium as the hard mask

- Finally, using patterned silicon dioxide as a backside hard mask, diamond structures are released from the silicon wafer through a DRIE process resulting in a free standing diamond bridge that is embedded in a silicon frame.
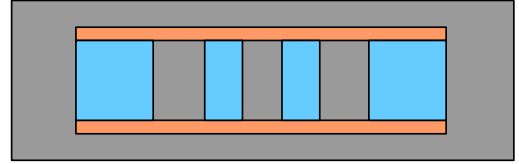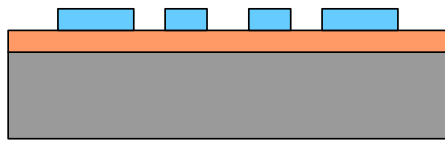
(A)
Intrinsic diamond is selectively grown on top of boron doped diamond. Resistivity of boron is around 1mΩ.cm
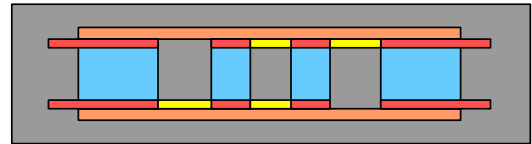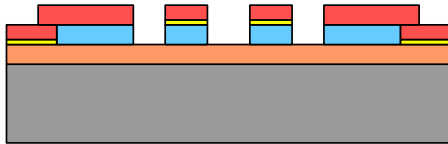
(B)
Copper bi-metal pads electroplated. A seed layer of Cr+Au is deposited using a thermal evaporator prior to the plating process
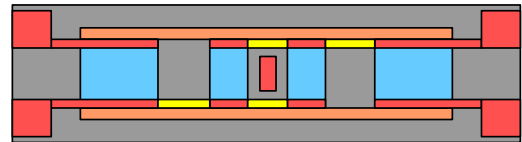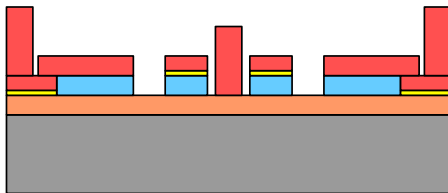
(C)
Copper pads for integration are electroplated. After this, seed layer is patterned to provide electrical continuity for the diamond bridge to be thermally actuated
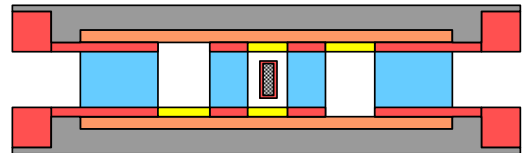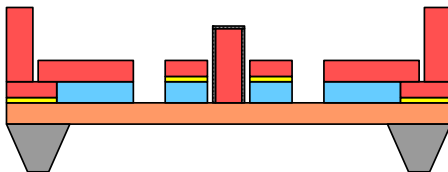
(D)
Finally, the diamond bridges are released through a DRIE process. Prior to this a thin layer of platinum is deposited on top of the copper contact through liftoff process.

Figure 4.6 – Fabrication Procedure of the Nanocrystalline Diamond Actuator

Figure 4.7(a) and 4.7(b) shows the front view and the back view of the fabricated diamond actuator. The overall size of the entire chip is 1600μm long and 900μm wide.

(a)   (b)
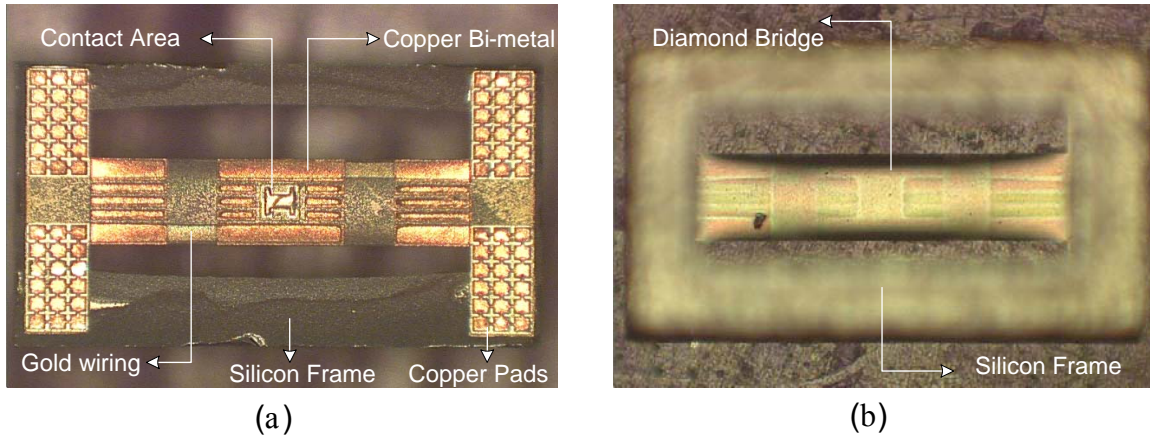
Figure 4.7 – Microphotograph of the Fabricated Diamond Actuator (a) Front View (b) Back View with the Silicon Frame

After the release process, each actuator (with the frame) is individually diced using a dicing saw. To avoid any damage the released actuators are glued onto a 3-4 inch silicon substrate. After dicing, they are cleaned in acetone and methanol to remove the glue. These diamond actuators, being embedded in the silicon frame, are substrate independent and can be integrated onto any microwave substrate that can withstand the high-temperature SOLID process [88]. Figure 4.8 shows the integration process of the diamond actuator to the host substrate in the CPW topology. In addition to CPW switches, the actuators are integrated to realize tunable CPW inductors and tunable switches in the microstrip topology.
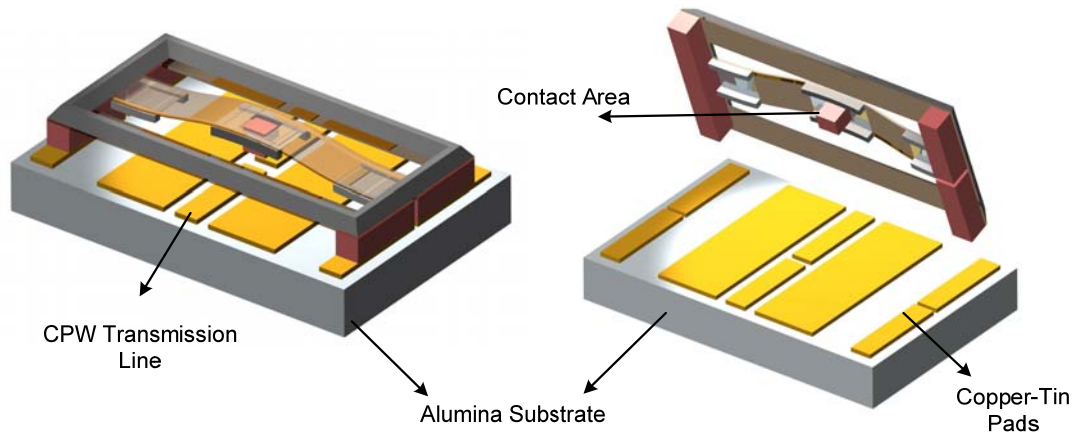
Figure 4.8 – Diamond Actuator Integrated onto a Host Substrate (Alumina, Aluminum Nitride) Using SOLID Process

53

In addition to the copper pads in the actuator frame, copper pads along with tin should be included in the host substrate for integration. Solid–liquid interdiffusion occurs between the two phases, resulting in a phase transformation of the liquid component to a higher melting point material, which is strong enough to serve as a bond and withstand elevated temperatures. Copper-Tin has been considered a SOLID [88] couple where tin acts a melting phase and copper as a solid phase. While integrating, the copper pads on the actuator are kept on top of the copper-tin stack and heated till 250^0C (melting point of tin). During the diffusion process one of the inter-metallic compounds forms the bond between the two structures and is stable till 600^0C. The alignment is carried out in a flip-chip bonding test setup wherein an accuracy of $\pm$ 5 microns is achieved during the integration. Heating for the solder process is supplied from the actuator part to prevent alloying of the pads that are located on the host substrate. Figure 4.9 shows the phase transformation in the SOLID process. Apart from Cu/Sn the other popular metal combinations are Ag/In, Au/Pb and Au/Sn.
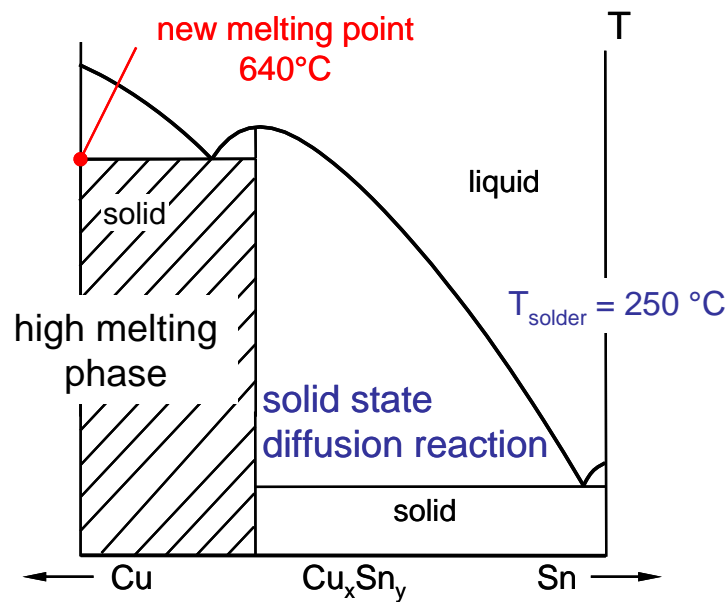
Figure 4.9 – Phase Transformation in the Cu-Sn SOLID Process

In the second generation switches, tin was included in the actuator part instead of the host substrate. This approach was chosen for better yield in the tin electroplating

process due to fabrication limitations. Figure 4.10 shows a microphotograph of the integrated switch with the host substrate. The four outer rectangles are copper blocks used for biasing the switches.
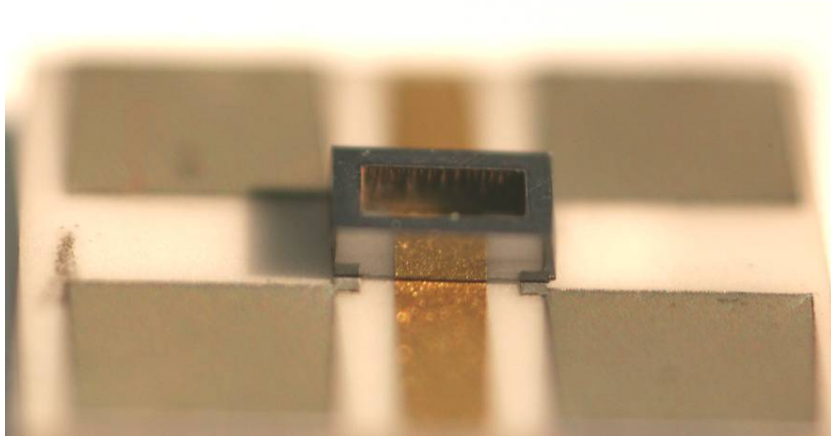
Figure 4.10 – Integrated Switch with a Host Alumina Substrate in a Microstrip Topology

4.4   Small Signal Analysis of the CPW Integrated Switch

The diamond actuators are used to realize RF-MEMS DC contact type switches in CPW and microstrip topologies. The CPW transmission lines are designed on a 650 μm thick alumina substrate (ε_r=9.9, tanδ=0.0002). The transmission lines are 3000 μm long with a center conductor width (W) of 100 μm and slot width (G) of 50 μm. The center conductor of these lines is purposefully interrupted in the middle resulting in two transmission lines which are 1475 μm long. During actuation, the contact pad in the diamond bridge closes this gap resulting in a continuous transmission path.

Small signal measurements were done in the frequency span of 1-30 GHz using an Anritsu Lightning VNA. A bias tee was used to protect the VNA test ports from DC current. Before measuring the structures a probe-tip SOLT calibration is performed on a commercial GGB CS-9 calibration. The diamond bridges are thermally actuated at 2 volts and upon actuation the platinum coated copper pad makes contact with the CPW line. Small signal simulations were performed using ADS Momentum, a 2.5 D electromagnetic simulator. Figure 4.11 and Figure 4.12 show the comparison between the simulated and measured S_{11} and S_{21} in the non-actuated and actuated states for the CPW integrated switch, respectively. The return loss and insertion loss in the actuated state are

20 dB and 0.2 dB, respectively, at 20GHz. It is evident from the S-parameters that in the actuated state, the diamond bridge makes a very good contact with the transmission line with a contact resistance of ~ 0.8 ohms.
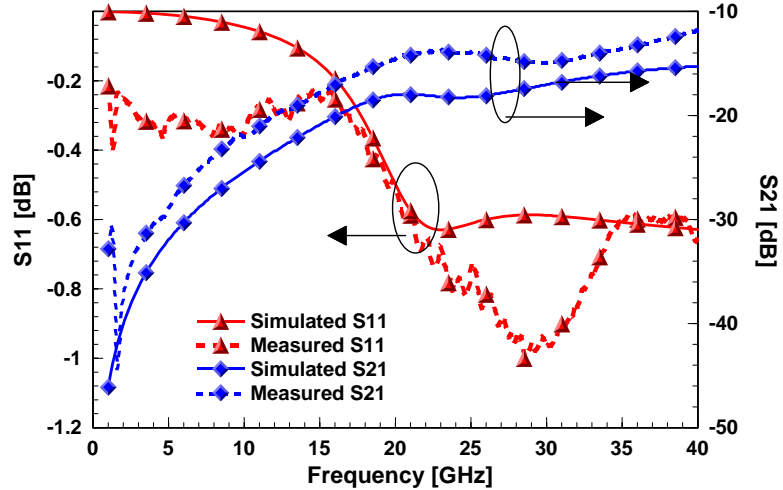
Figure 4.11 – S-Parameters of the CPW Integrated Actuator in the Non-Actuated State
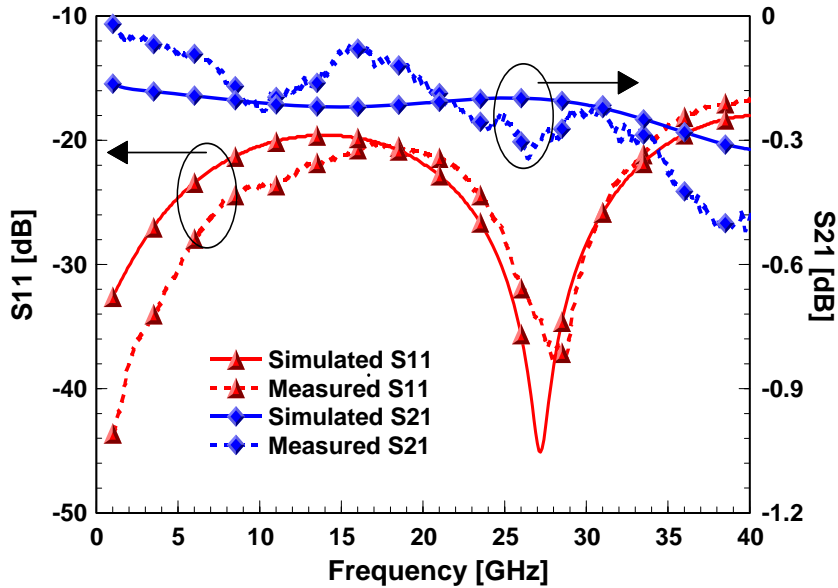
Figure 4.12 – S-Parameters of the CPW Integrated Actuator in the Actuated State

4.5 Small Signal Analysis of the CPW Inductor

Inductors are integral components in RF front end architectures that include filters, matching networks and tunable circuits such as phase shifters. The most common

inductor topologies include planar spirals, air-core, and embedded solenoid designs [7]. In comparison to capacitors, however, relatively few tunable inductor configurations have been published, and among those presented many are hybrid approaches that employ (MEMS) switches to activate different static inductive sections. Furthermore, less attention has been paid to designs that enable control in the sub-nH range as is potentially desirable for matching purposes in applications that use distributed loading of small capacitances, e.g. in loaded-line phase shifters [7].

From transmission line theory, narrow or thin high impedance transmission lines are analogous to inductors. The inductance value is dependent on the width and length of the line. Generally speaking the net inductance value increases with an increase in length and decrease in width. In addition to implementing the devices as a simple RF switch, tunable inductors were realized wherein the non-actuated and the actuated-state of the bridges yield different net inductance values [89]. The inductor circuits fabricated on the alumina substrate are 400 μm long. Figure 4.13 shows the inductor layout along with the integrated diamond bridge.
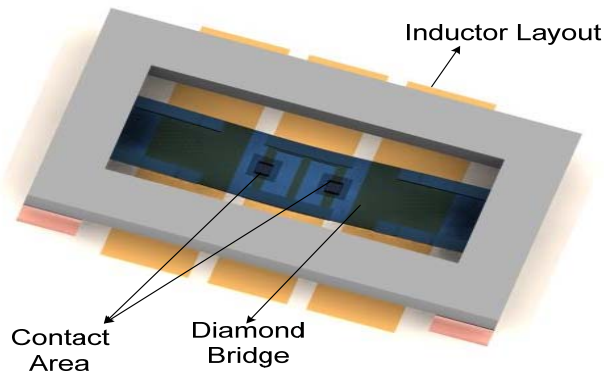
Figure 4.13 - Design of the Integrated CPW Inductor and Diamond Actuator

The geometry of the transmission line is a crucial factor in determining the net inductance value in the non-actuated (L_{high}) state and in the actuated state (L_{low}) of the inductor. The inductors are designed such that the characteristic impedance of the feed lines is close to 50 Ohms. The impedance value of these feed lines is a function of the center conductor width and slot width. In this work, the center conductor width (w) and

slot width (s) is 270 μm and 115 μm, respectively. The overall length of the inductor circuits is approximately 400 μm. Although the inductance value can be increased by making the center conductor narrower, processing limitations restricted the minimum width to 30 μm. These CPW lines are designed in a way that the effective inductance value (L_{eff}) is much greater in comparison to the capacitance in the transmission line. The inductance value for all the designs is controlled by the fixed-fixed beams, wherein the L_{eff} values differ with the actuated and non-actuated state of the beam. The inductors are designed to have a high inductance value when the beams are up and low inductance value in the actuated state of the beams. When the beams are in the non-actuated (up) state, the circuit offers high impedance (Z_h) to the input signal. Since the length of the device is electrically small (0.075λ at 25GHz) the topology effectively emulates a lumped inductor with high inductance value (L_{high}). In the down-state the inductance value (L_{low}) reduces due to the decrease in the effective characteristic impedance (Z_l). The inductance ratio (L_{ratio}) is directly related to the change in the impedance states (Z_h/Z_l) and is defined as (L_{high}/L_{low}).

For a short electrical length ($< \pi/4$) a high impedance transmission line section emulates a series inductor as given by equation 4.6. Tunable operation is achieved by changing the effective width of the slot and/or the center conductor by using the diamond actuator.

$$L_d = \frac{Z_h q_1}{w}; \; L_u = \frac{Z_l q_2}{w} \tag{4.6}$$

In the non-actuated state of the actuator the inductor represents a high impedance state which translates into a high inductance value. When the bridges are actuated the contact pads makes a DC short with the transmission lines, leading to low impedance and in turn a low inductance state. Figure 4.14 (a) and (b) shows the top view the tunable inductor wherein the change in width of the transmission line correspond to the change in inductance between the two states.
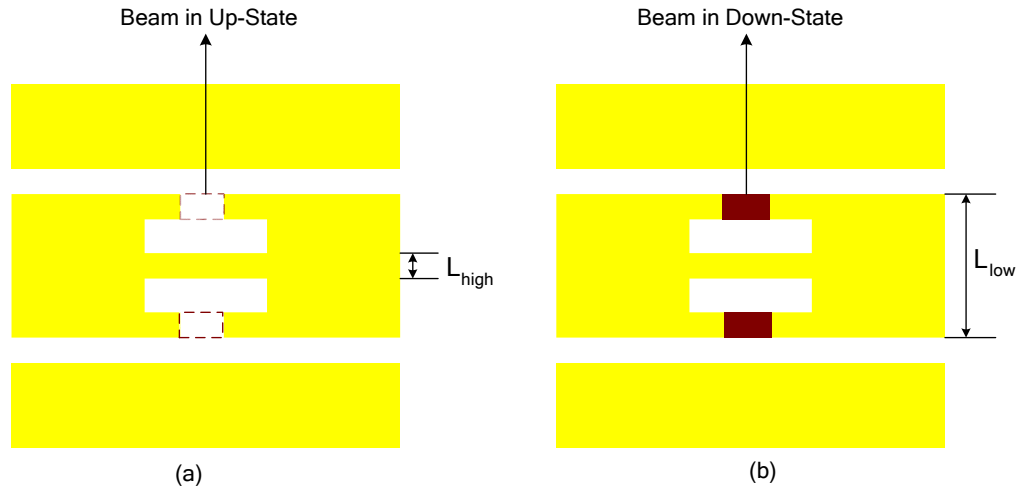
Figure 4.14 – Change in Impedance and Effective Inductance Between the Up-State and Down-State of the Tunable Inductor

The inductors were measured in the frequency range of 1-30 GHz in the same setup as that of the RF switches. Figure 4.15 and Figure 4.16 shows the return loss and insertion loss, respectively of the tunable inductor in the non-actuated and the actuated state of the diamond bridge.
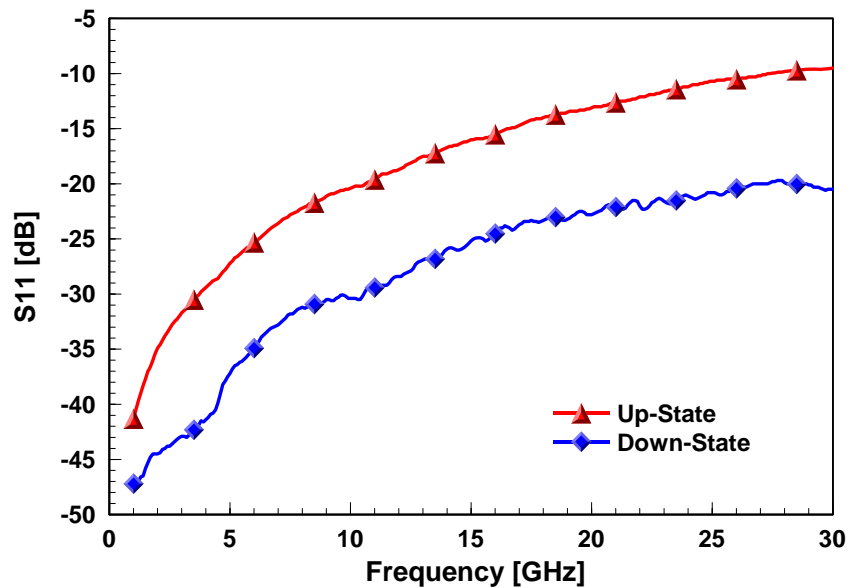
Figure 4.15 – Measured Return Loss (S_{11}) of the Inductor in the Non-Actuated and Actuated State
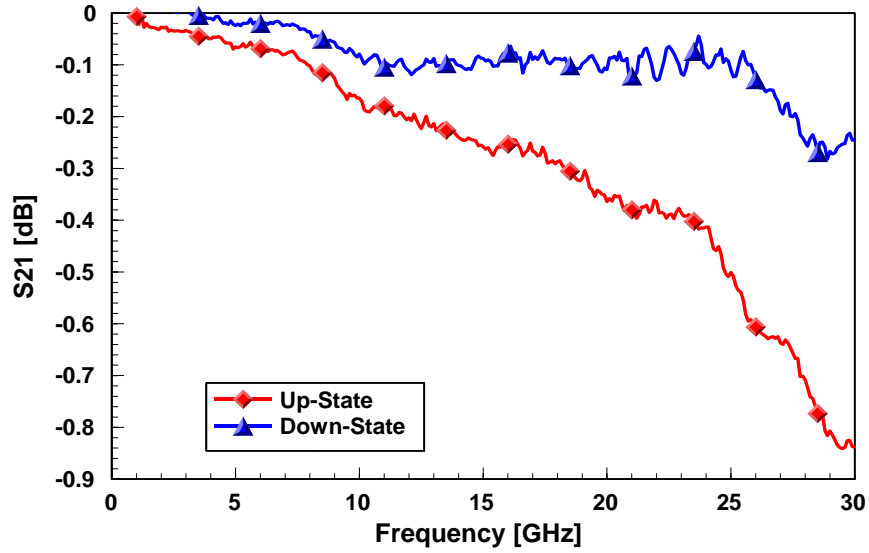
Figure 4.16 – Measured Insertion Loss (S_{21}) of the Inductor in the Non-Actuated and Actuated State

The effective inductance (L_{eff}) of the circuit is extracted by numerically shorting port 2 of the inductor and is related to the input impedance (Z_{in}) by equation 4.7.

$$L_{eff} = \frac{Im\{Z_{in}\}}{2 * \pi * freq}$$ (4.7)

The measured inductance in the two states and the inductance ratio (L_{ratio}) are shown in Figure 4.17. An inductance ratio of 2.2 was achieved at 30 GHz with 1.2 being the maximum inductance value.
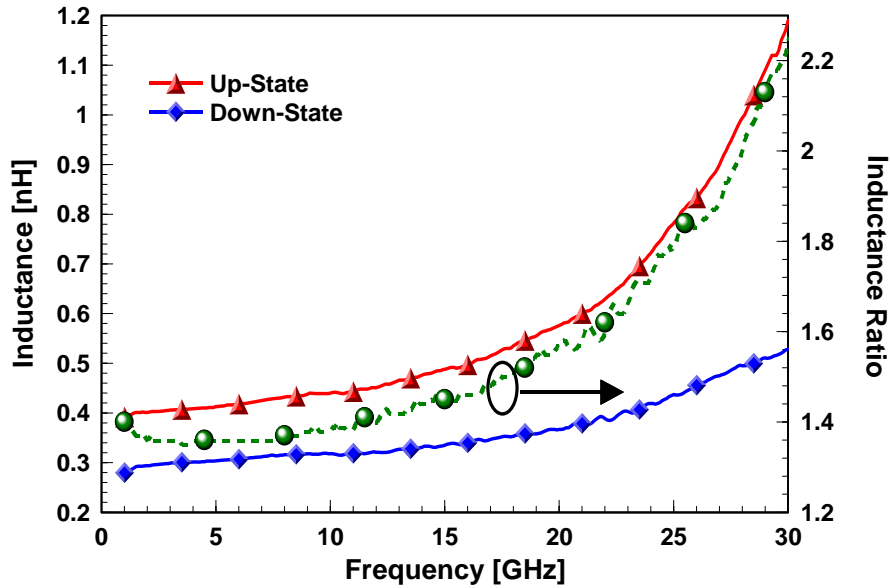
Figure 4.17 – Measured Inductance in Up and Down States and Inductance Ratio

4.6 Large Signal Measurements – 1st Generation

Power handling capabilities of RF-MEMS devices have been previously investigated for series [38] and shunt capacitive switches [90] at X-band frequencies up to an input power of 7 watts. In this work, the micromachined diamond air-bridge integrated in the microstrip topology is tested at 2.1 GHz until 45 watts. Prior to testing, the microstrip substrate with the diamond bridge is modified for the measurement setup. The alumina wafer is solder attached to a brass carrier. Two 250 mil long, 50 Ω microstrip lines are fabricated on a 31 mil FR4 substrate and solder mounted on the either side of the alumina wafer; this is done to connect the SMA coaxial adapters on either side of the carrier for testing. Bond wires which are 3-mil in diameter are used to connect the 50 Ω lines with the microstrip line on the alumina substrate. Figure 4.18 shows the details of the coaxial test fixture used for high power measurement.
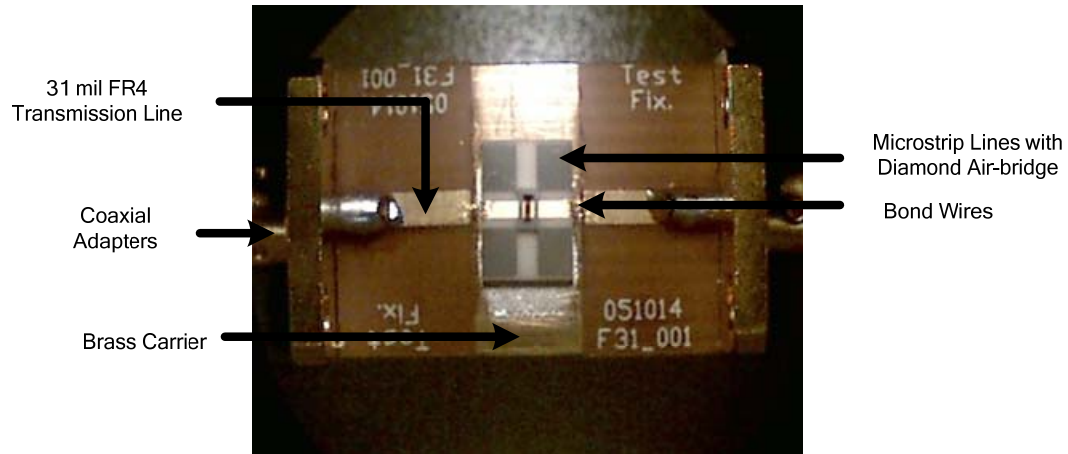
Figure 4.18 – Diamond Actuator Integrated in Microstrip Topology for High Power Testing

The setup for high power measurement is shown in Figure 4.19. Maury Microwave ATS 400 software was used to extract the data. An Anritsu 68169B signal generator is used as the RF source. The frequency and input power level for the measurements are 2.1 GH and 15 dBm, respectively. In the next stage the input signal is passed through a 100 watt amplifier with a gain of 50 dB. A three port circulator is used as an isolator with the third port terminated by a 100 watt load, in order to isolate the signal source and the amplifier from potential high reflected power. The isolator and the brass carrier are mounted on a heat sink to avoid thermal issues. The signal source, amplifier and the isolator constituted the input side of the high power setup. The output signal from the diamond actuator (DUT) is passed through stages of high power attenuators before measuring the power level in an Anritsu power meter. Prior to measurement, a two port thru calibration is performed wherein the reference planes were shifted to the inner edges of the 31 mil FR4 transmission line. Measurements are performed in the power range of 24-47 dBm at 2.1 GHz. For the initial test circuits, electrical actuation of the diamond actuators did not result in intimate contact of the copper pads with the host substrate due to issues associated with the flip-chip bonding. To work around this issue, the diamond bridges were mechanically actuated in addition to the applied DC voltage.
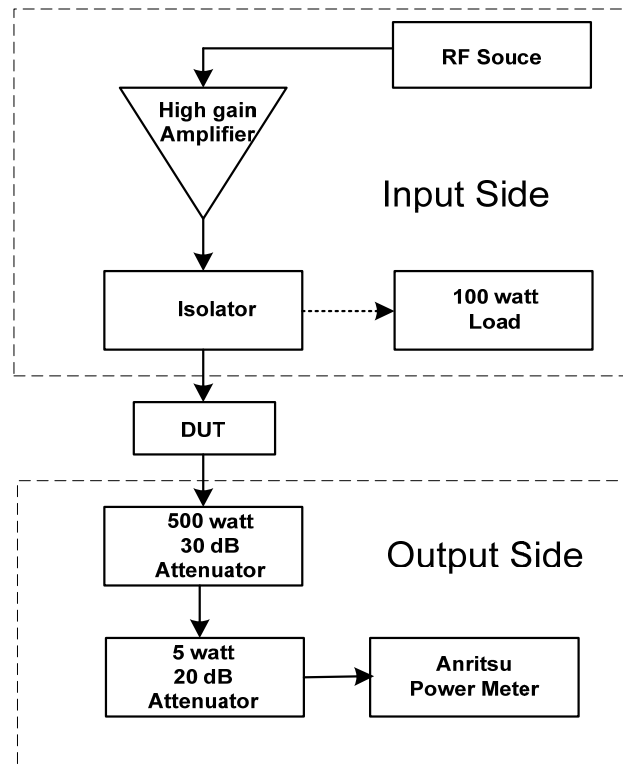
Figure 4.19 – High Power Bench for Testing Diamond Switches

The switches are tested for self actuation and isolation in the up-state. The measured insertion loss (or isolation) in the non-actuated state is shown in Figure 4.20. As seen from graph, the measured isolation is around 16-17 dB at 2.1 GHz in the entire power range. Unlike most of the RF-MEMS switches, the bias pads and the RF transmission lines are isolated from each other in the integrated diamond actuator. This isolation prevents the bridges from self actuation problems when an input RF power is applied. Furthermore in the initial high power tests, some variation in the device performance was noticed and complete contact was not obtained using electrical actuation; this can be attributed to the height differences in the flip-chip mounted structures. Therefore the devices used in the high power testing required such mechanical actuation, which was achieved using a needle probe attached to a micro-positioner.
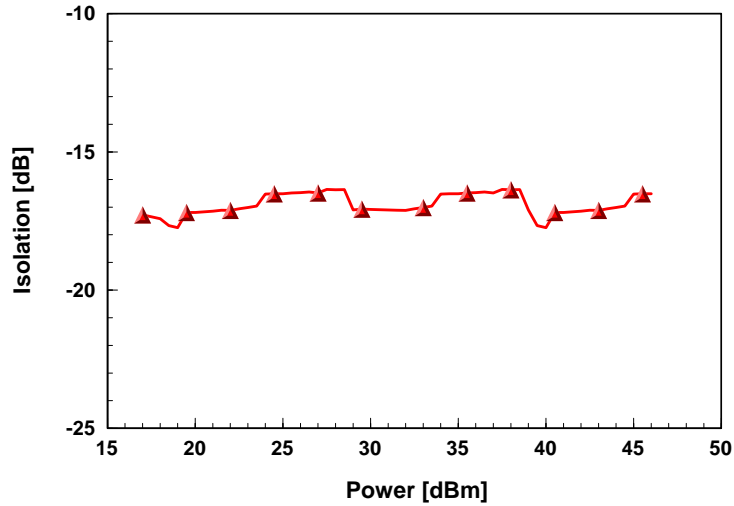
Figure 4.20 – Measured Isolation of the Diamond Actuator in the Non-Actuated State with Varying Input Power

As shown in Figure 4.21, the insertion loss is around 0.2-0.3 dB throughout the entire power spectrum. Measurements were made for more than one instance for repeatability and there was no significant difference in the insertion loss. The diamond bridge was stable at such power with little or no damage due to heating of the structure. Diamond which also is an excellent conductor of heat acts a good heat sink during measurement. As an improvement to this device, a dual actuation scheme based NCD bridges are being developed. In this scheme, the advantages of electrostatic and thermal actuation are used together to develop more reliable NCD actuators.
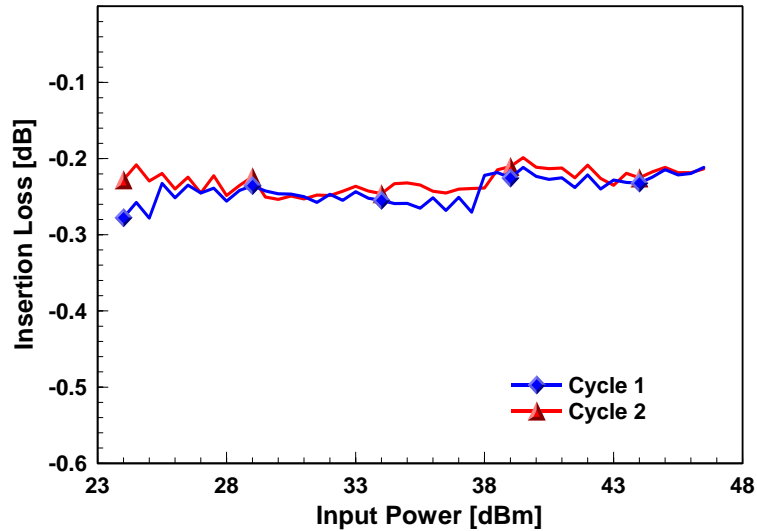
Figure 4.21 – Measured Insertion Loss of the Diamond Actuator in the Actuated State with Varying Input Power

4.7 Dual Mode Actuation of the NCD Switches

As discussed in Chapter 2, a potential disadvantage of thermal actuation is that DC power may be required to hold a device in the ON-state or OFF-state. This problem was addressed by developing actuators which operated in a bi-stable mode, wherein the actuators remain down after removing the voltage. An alternate method to address this issue is to develop switches which can actuate at a low voltage and avoid the current consumption issue by adopting a latching approach. Saias et al. [19] has demonstrated this technique for medium to high power applications using standard micromachining. The switches are fabricated on a silicon substrate in a CPW topology and are actuated using an integrated 300 μm X 300 μm CMOS driver. Once the devices are in the on-state latching electrodes secure the MEMS beam and the drive voltage/current can be removed.

In the second generation switches studied in this work the diamond actuators are integrated onto aluminum nitride (AlN) substrates. In comparison to alumina (Al_2O_3), aluminum nitride has higher thermal conductivity (140 W/mK for AlN and 18-20 W/mK for Al_2O_3). Furthermore, this integration process is also done to exhibit the substrate independent nature of the diamond actuators. Furthermore, in addition to thermally

actuating the switches, an electrostatic latch feature is used to hold the switch in the actuated state. In the absence of a bi-stable operation, this dual mode actuation (thermal + electrostatic) scheme will be useful to avoid the power consumption issues. The electrostatic latch is incorporated on the host substrate. High resistive silicon chrome (SiCr) is deposited using an e-beam evaporator to a thickness of 1500 A^0. Silicon nitride which serves as an isolation layer is patterned on top of the SiCr bias lines. After the switches are thermally actuated, SiCr and the doped diamond actuator are used as the two electrodes to facilitate the electrostatic latch mechanism. Figure 4.22 shows the description of this dual mode actuation scheme. The SiCr bias lines do not come in contact with the diamond bridges upon actuation and hence the issue of an electrical short can be avoided. In the CPW version of the switches, the electrostatic latch can be implemented by positioning the SiCr lines in the slot region or by using the ground planes as the latch electrode.

Deposition of High Resistive SiCr

Deposition of Silicon Nitride for Isolation
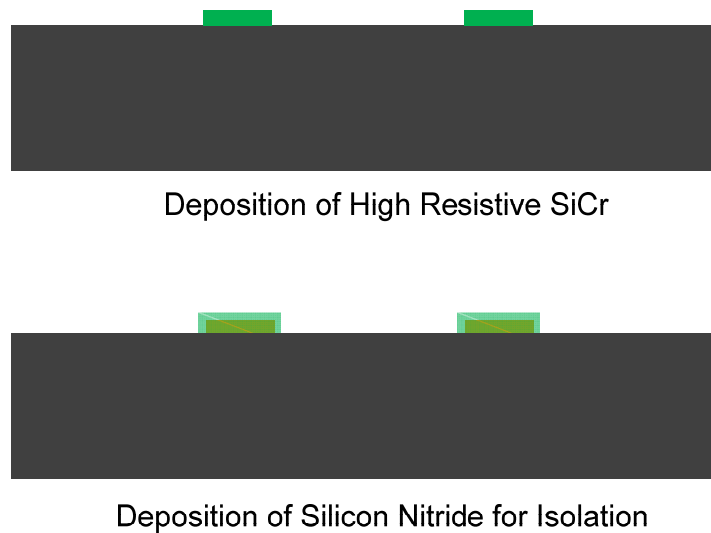
Figure 4.22 – Fabrication and Integration of the Dual Mode Actuation Scheme of the NCD Bridges

Deposition of Copper Pads and Gold Transmission Lines

Thermally actuated Integrated NCD Switch

Electrostatic Latch to keep the Switch in Actuated State
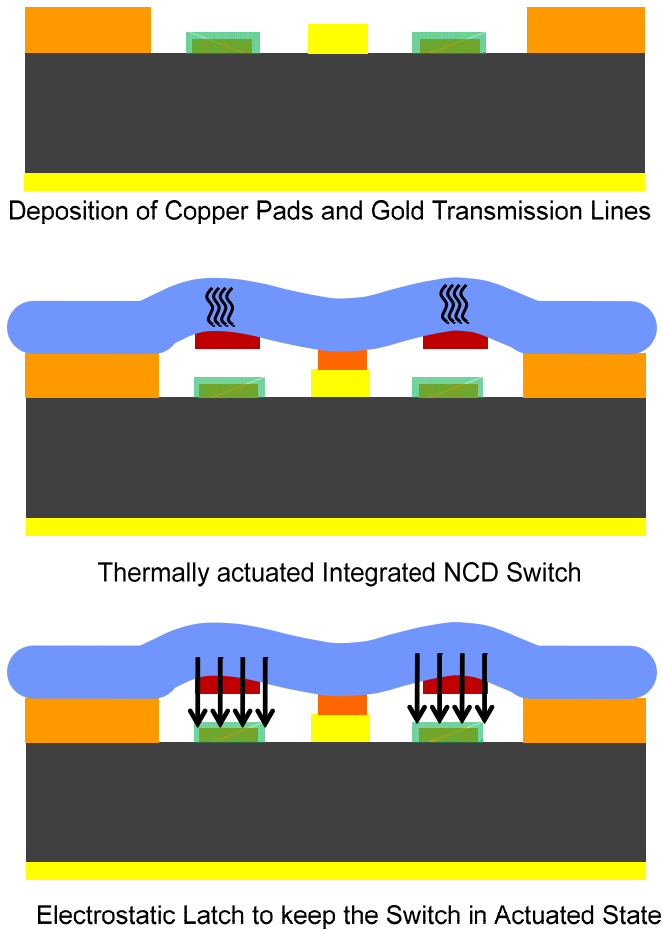
Figure 4.22 – (Continued)

4.8   Large Signal Measurements – 2nd Generation

In the thermal scheme, the switches are first actuated at 3 volts with a current value of 20 mA. Then the electrostatic hold down voltage of 28-30 volts is applied between the SiCr pads the NCD bridge. . Furthermore, due to equipment limitations, measurements for the 2nd generation switches are performed at a CW frequency of 1.9 GHz. In order to check the power handling limit of the NCD bridges, the actuators are gradually tested at increasing power levels starting from 20 dBm to 40 dBm. This is done to better understand the performance of the actuators and also avoid any damage at high power levels. Figure 4.23 shows the measured insertion loss as function of power. In this graph cycle 1 corresponds to a maximum power level of 30 dBm and cycle 10 corresponds to the measured insertion loss at a maximum input power of 40 dBm. Cycle

1 to cycle 10 increases in power level by 1 dBm. From the measured results we can conclude the increased power level at little to no effect on the insertion loss. The high thermal conductivity of NCD films prevents issues like welding and hot spot formation at these elevated power levels. The measurements are stopped at 40 dBm due to the limitations of the high power amplifier used. New measurements are under progress to test the switches at high power levels by incorporating small changes in the large signal measurement setup.
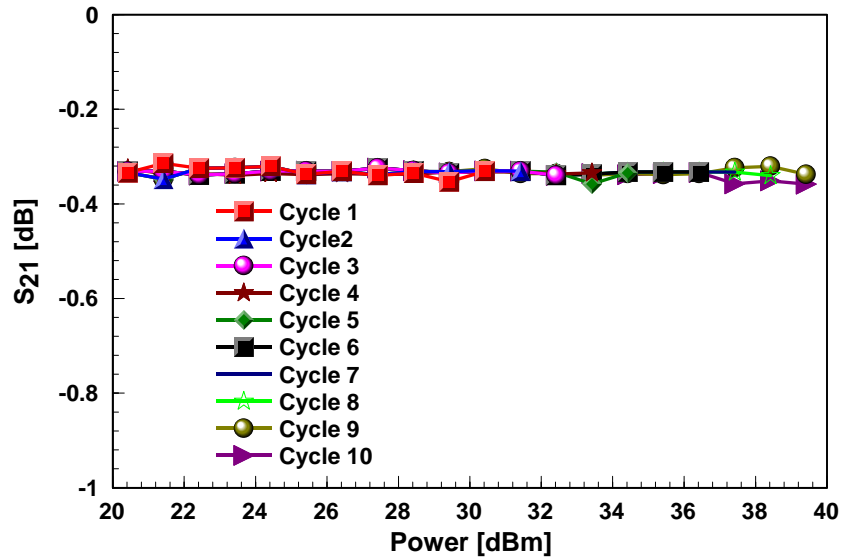
Figure 4.23 – Measured Insertion Loss at a CW Frequency of 1.9 GHz with Maximum Input Power Varying from 30 dBm to 40 dBm

In order to understand the performance of the NCD actuators at high power levels for a longer period of time, measurements are also carried out in the power span of 20-37 dBm. These measurements are carried out after actuating the NCD bridges continuously for a maximum of 2 hours using an Agilent 33120A function generator. A square wave signal at a frequency of 1 KHz (value lesser than the first order mechanical resonant frequency) with a peak to peak (V_{PP}) voltage of 4 volts is used for actuating the switches. Firstly the switches are actuated using the dual actuation scheme and then insertion loss is measured in the power span of 20-37 dBm. After the first set of measurements, the switches are actuated continuously using the thermal scheme for a period of 30 minutes. The high power measurements are once again carried out after that duration to see the

depreciation, if any, in the performance of the switches. This is repeated for a period 30-120 minutes. The above mentioned power level is chosen to ensure the actuators do not suffer any mechanical degradation over time. In addition to measuring the insertion loss, the switches are also tested for self actuation after the above mentioned 2 hours of testing. The actuators continued to exhibit no self actuation issues after actuating them continuously for 2 hours. Figure 4.24 and Figure 4.25 show the measured isolation loss and insertion loss, respectively. It is seen that the actuators exhibited consistent performance with no degradation in the mechanical stability and electrical performance of the switch. Further measurements are under progress to test the switches at high power levels for a longer period of time.
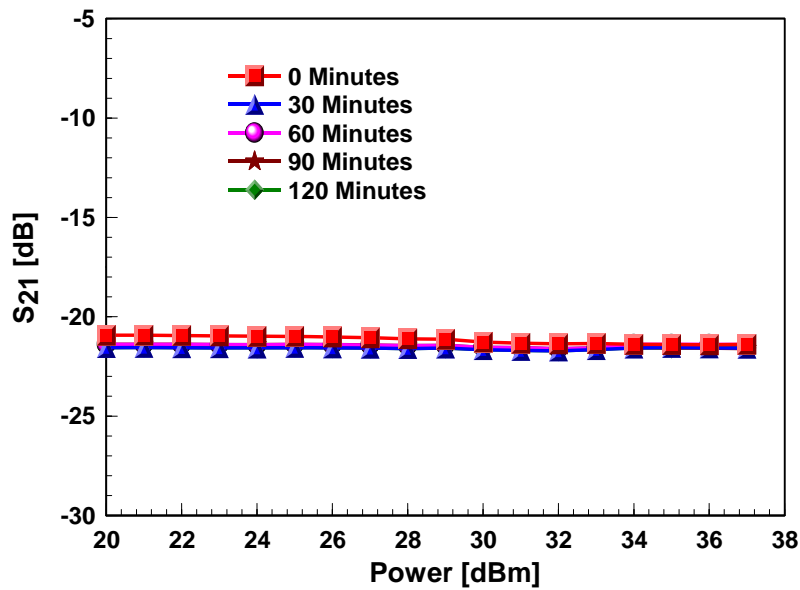
Figure 4.24 – Measured Isolation Loss After Two Hours of Continuous Actuation of the Diamond Bridges
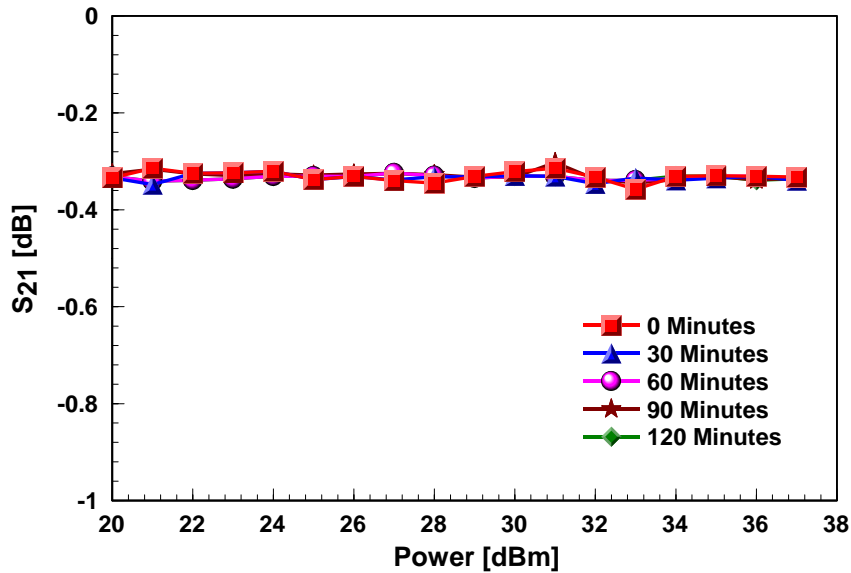
Figure 4.25 – Measured Insertion Loss After Two Hours of Continuous Actuation of the Diamond Bridges

4.9   Summary

In this work, thermally actuated nanocrystalline diamond bridges are presented. Intrinsic and boron doped NCD films have been grown on low resistive silicon wafer. The films are intentionally grown with built in compressive stress and the measured values were in the range of 140- 560 MPa. Design, fabrication and integration of the compressively stressed bi-stable actuators are presented in detail. Experimental results of a RF switch and tunable inductors using nanocrystalline diamond bridges are presented. The switches were thermally actuated and the measured results show a return loss and insertion loss of 20 dB and 0.2dB, respectively, at 20GHz. Tunable inductors were also designed and measured in the frequency range of 1-30GHz and the measured results show a inductance ratio of 2.2 at 30 GHz. In addition to the thermally actuated switches, the second generation switches are designed utilizing both thermal and electrostatic actuation schemes. High power measurements are performed on the diamond actuators in the power range of 24-47 dBm for the mechanically actuated switches, and 24-40 dBm for electrically actuated switches. The measurements show an insertion loss of 0.2-03 dB in the entire power spectrum.

Chapter 5

Nanocrystalline Diamond Capacitive Shunt Switches

5.1   Introduction

RF-MEMS devices have been implemented in a broad range of designs as DC contact [89] and capacitive switches [13] in series and shunt configurations [11]. This development work has facilitated significant maturing of the technology and technical challenges such as reliability [91], packaging [41] and high power operation [42] are now relatively well understood. In particular, the dielectric charging mechanism [26] is one of the main factors that limits the reliability of capacitive switches. This charging mechanism has been addressed in detail by several researchers [26-29] and has been discussed in Chapter 2. The usage of bi-polar actuation voltage [92] is one of the accepted means of mitigating this phenomenon. Further reduction of charging effects can be realized with the use of leaky dielectrics, given that the associated microwave loss does not significantly impair the RF switch performance. The finite DC conductivity of the diamond layer provides a conductive path for possible trapped charges [93].

In this work, a prototype design of a mm-wave shunt capacitive switch in coplanar waveguide, using NCD as the dielectric is presented. While the superior material properties of NCD films have been utilized in realizing electrostatic [94] and thermally [95] actuated switches, this is first demonstration of RF-MEMS switches using NCD as the insulator. The devices are fabricated on a high resistivity silicon substrate using standard lithography and surface micromachining techniques. Small signal measurements are performed in the frequency range of 1-65 GHz, along with preliminary charging studies that have been performed using Corona-Kelvin metrology (CKM) and standard I-V techniques. Both techniques confirm the leaky nature of the NCD film, where the voltage time rate of decay observed with the CKM technique and the leakage current in the I-V technique are increased relative to the PECVD nitride films.

71

5.2　　Design and Simulation Results

Figure 5.1 shows the geometry of the shunt switch. The switch is designed in a CPW topology and the dimensions of the CPW feedlines are determined using ADS LinceCalc [96] to be 100 μm for the center conductor and 60 μm for the slot, yielding a characteristic impedance of 50 ohms. The switches are 320 μm in length and 50 μm in width. The overlap area of the switch with the dielectric is 130 x 130 μm.
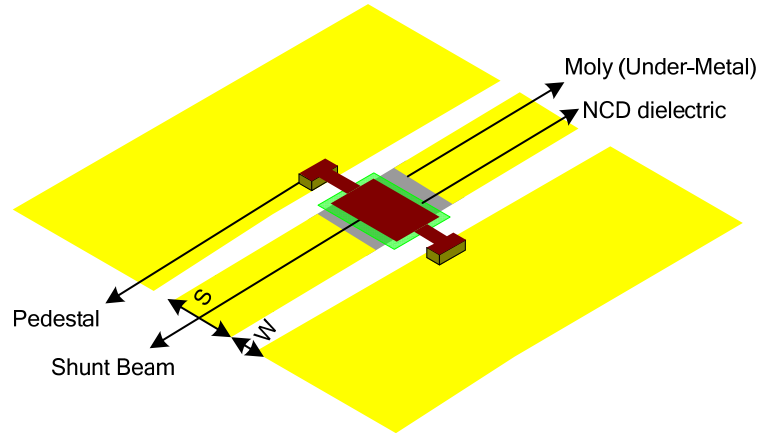
Figure 5.1 – Cross Section of the NCD Capacitive Switch

The capacitive switch is actuated using the electrostatic actuation scheme, wherein a DC voltage is applied between the MEMS bridge and the CPW transmission line. This creates an electrostatic force resulting in the collapse of the suspended bridge on the dielectric layer. In the down-state, the capacitance contributed by the metal-insulator-metal structure increases by a factor of 30-50. The increased capacitance connects the bridge and ground of the transmission line thereby creating a short at microwave frequencies. Once the voltage is removed, the bridge returns to the normal position by the restoring force. Undoped NCD film, which is the dielectric layer, is deposited using the MPECVD technique to a thickness of 0.5 μm. The relative dielectric constant of the dielectric NCD film is ~ 5. The movable membrane is 1.5 μm thick and is suspended 2 μm above the dielectric layer.

The switch design can be electrically represented as a shunt LCR circuit. Figure 5.2 shows the equivalent circuit of the capacitive shunt switch. In this "L", is the bridge

inductance, C_{Up} and C_{Down} represents the parallel plate capacitance in the non-actuated and actuated state, respectively. The series resistance "R" is contributed by the transmission line and the bridge. Although a better model can be derived to separate the individual resistance values, in this work, R accounts for both the components.
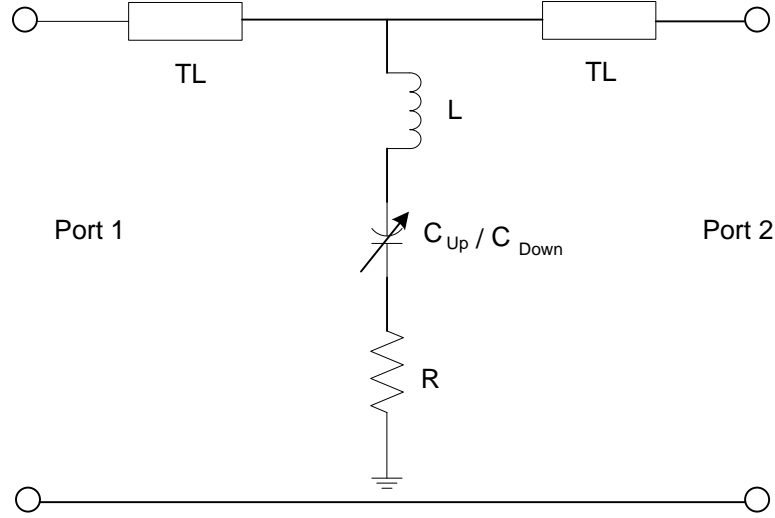
Figure 5.2 – Equivalent Circuit of the NCD Capacitive Shunt Switch

The shunt switch impedance is dependent on all three lumped elements and can be represented as

$$Z = R + j\omega L + \frac{1}{j\omega C} \tag{5.1}$$

where C changes between C_{Up} and C_{Down} depending on the actuation state of the switch. The LC resonant frequency of the switch is given by

$$F_{res} = \frac{1}{2\pi\sqrt{LC}} \tag{5.2}$$

The impedance of the switch changes depends on the frequency at which the switch operates. Below the resonant frequency, the circuit operates as a capacitor and above the resonant frequency it operates as an inductor. At the resonance frequency, the model is dominated by the series resistance. The up-state capacitance is a combination of

73

the parallel plate capacitance (C_{pp}) and the fringing field capacitance (C_{ff}). This fringing field capacitance is generally 30- 40 % of C_{pp}, which can be represented as

$$C_{pp} = \frac{\varepsilon_0 w W}{g + \dfrac{d}{\varepsilon_r}}$$ (5.3)

where ε_0 and ε_r are the absolute and relative dielectric constants, respectively. W and w are the widths of the transmission line and beam, respectively. g is the air gap between the transmission line and bridge and d is the thickness of the NCD dielectric layer. The down-state capacitance can be given by

$$C_{Down} = \frac{\varepsilon_0 \varepsilon_r w W}{d}$$ (5.4)

For the switch designed in this work, the inductance L does not have a significant effect on the up-state loss within the intended frequency band of operation. Hence the equivalent circuit shown in Figure 5.2 can be modeled only as a capacitor in this state.

In addition to the basic design, an inductively tuned shunt switch (Design 2) has also been designed. Figure 5.3 shows the basic and inductively tuned designs. Inductively tuned designs are used to achieve high isolation at lower frequencies (X band etc). This can be done by increasing the shunt inductance while maintaining the down-state capacitance of the switch
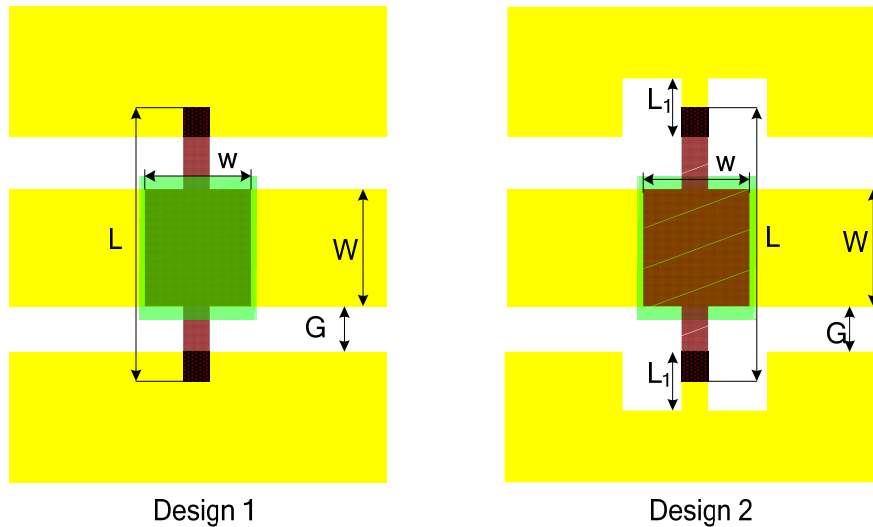
Figure 5.3 – Top View of the Basic and Inductively Tuned NCD Capacitive Switch

74

Figure 5.4 shows the isolation of the MEMS switch with a down-state capacitance of 1.26 pF. The capacitance value is similar to the standard switch. The change in resonant frequency is contributed by the change in inductance from the high impedance section transmission line between the bridge and ground plane. Simulations are performed for different values of L1, which is the length of the high impedance line. As seen from Figure 5.4, the resonant frequency shifts from 30 GHz to 20 GHz with L1 changing from 50µm to 200µm. For convenience in this work, L1 is chosen to be 150 µm.
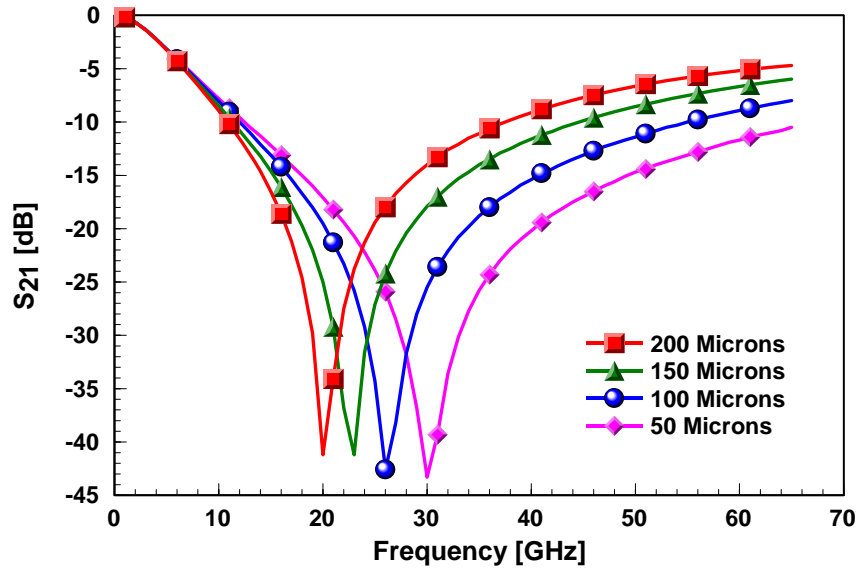
Figure 5.4 – Simulated Change in Resonant Frequency of the Inductively Tuned Shunt Switch in the Down-State for Varying Lengths of the High Impedance Line

The shunt switches are simulated in Agilent's ADS Momentum which is a 2.5D electromagnetic simulator. Figure 5.5 and Figure 5.6 show the simulated return loss (S_{11}) and insertion loss (S_{21}) in the non-actuated state and actuated state, respectively, for both designs.
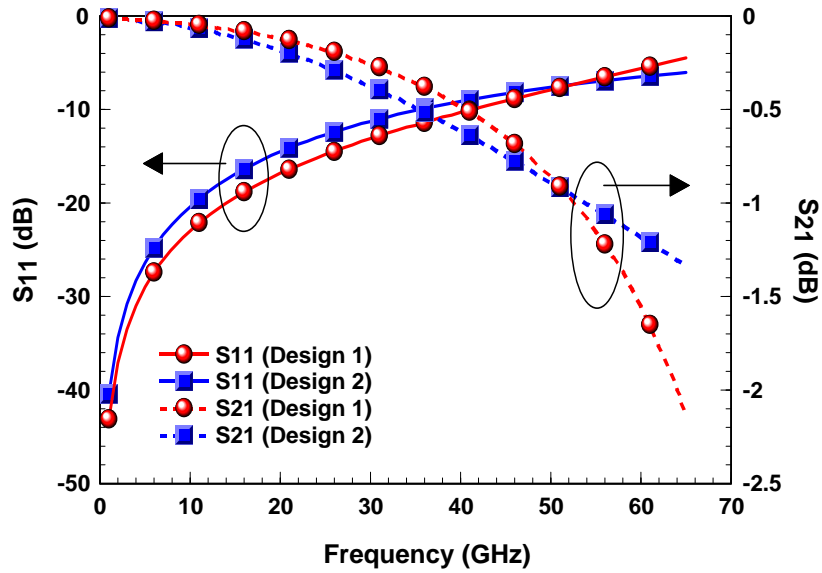
Figure 5.5 – Simulated S_{11} and S_{21} for the Basic (Design 1) and Inductively Tuned (Design 2) Capacitive Switch in the Up-State
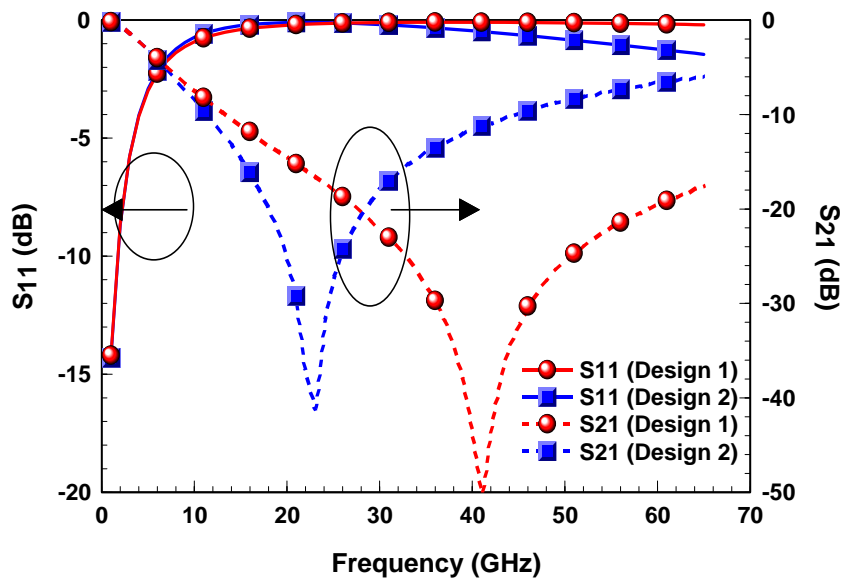
Figure 5.6 – Simulated S_{11} and S_{21} for the Basic (Design 1) and Inductively Tuned (Design 2) Capacitive Switch in the Down-State

From the simulated S_{21} response we can observe a shift in resonant frequency between the two designs. Although each design has nearly equal down-state capacitance (~ 1.28 pF), the inductively-tuned design has a much higher inductance value. The

modeled inductance value for design 1 and design 2 in the actuated state is 11.9 pH and 38.7 pH, respectively.

Figure 5.7 shows the comparison of the simulated and modeled S_{21} in the actuated state for both the designs. Tabulated results of the lumped element components from the equivalent circuit will be presented in the measurements section. As stated earlier, the high impedance T.L has little effect on the up-state performance of the switch.
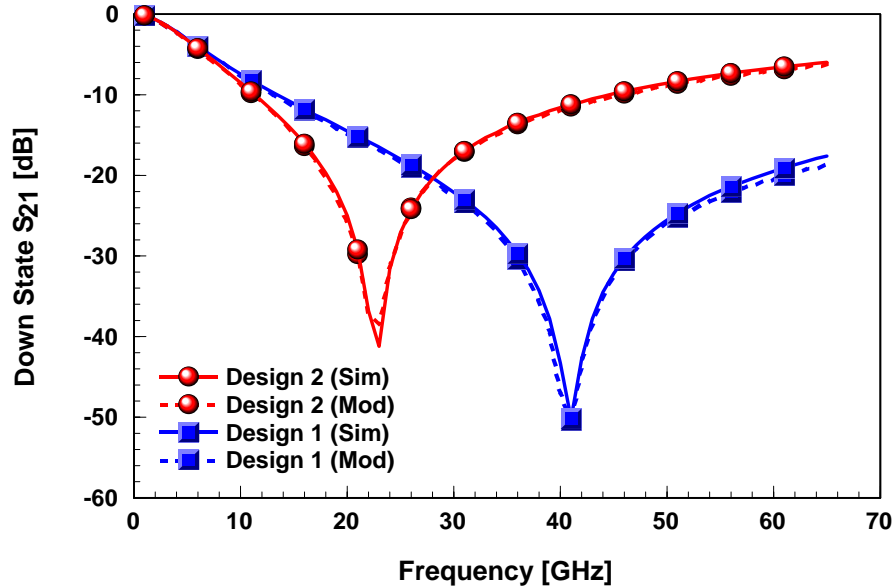
Figure 5.7 – Comparison of Simulated and Modeled S_{21} in the Down-State

5.3   Material Characterization and Fabrication

The switches are fabricated on high resistivity silicon wafers (ε_r=11.8, ρ > 2000 ohm-cm) that are cleaned using a standard RCA process. The fabrication steps as shown in Figure 5.8 are as follows:

- Molybdenum, which is a carbide forming material, is used as the bottom metal. Molybdenum is deposited by RF sputtering to a thickness of 0.7μm.
- An intrinsic NCD film is grown to a thickness of 5000 A^0. Prior to the growth the substrate is ultrasonically seeded in a nano-diamond powder dispersed in methanol. This film is later etched in O_2:CF_4 plasma using titanium as the etch mask. The typical etch rate for diamond is 300 A^0/minute.

- CPW metal lines are fabricated using a lift-off process. The Cr/Au metal lines are deposited using a thermal evaporator to a total thickness of 1μm.

- PMMA is used as the sacrificial layer and spun on to a thickness of 1.5 μm. The moveable membrane is gold electroplated to a thickness of 1.3 μm. Prior to plating, a seed layer of Cr/Au is deposited to a thickness of 1600 A^0.

- The sacrificial layer is removed in 1165 solution and the MEMS structures are released using a critical point dryer.

In this work, the NCD film is grown using the MPECVD technique. Prior to this, attempts were made to deposit the films through the hot filament technique. Apparently the very high temperature near the filaments of the reactor ($\sim 1200^0$C) caused growth defects and this resulted in the peeling of the underlying carbide forming layer. Both tungsten (W) and molybdenum (Mo) were used and the peeling problem was noticed in both the cases. In the MPECVD technique, NCD growth is good in both W and Mo. Unlike other dielectric films, the roughness of NCD on the under metal has a significant effect on the performance of the switch and in turn the capacitance upon actuation. Table 5.1 shows the comparison of the roughness of the under metal before and after the dielectric deposition. For clarity the roughness of NCD films are compared to that of nitride films grown in the PECVD technique.

Table 5.1 – Comparison of Roughness of Metal + Dielectric Stack Before and After Deposition

Metal + Dielectric Combination	Roughness before Dielectric (nm)	Roughness after Dielectric (nm)
Moly + NCD	1.5	9.4
Moly + Si_3N_4	1.5	4.8
Tungsten + NCD	0.9	8.7
Tungten + Si_3N_4	0.9	4.1

(A) Deposit Under Metal (Mo/W)

(B) Intrinsic NCD is grown and patterned in RIE

(C) CPW lines are evaporated with Cr/Au

(D) Sacrifical layer (PMMA) is spun to a thickness of 1.5 μm

(E) Shunt beam is gold electroplated to 1.3 μm

(F) Sacrificial layer is removed in 1165 and released in CPD
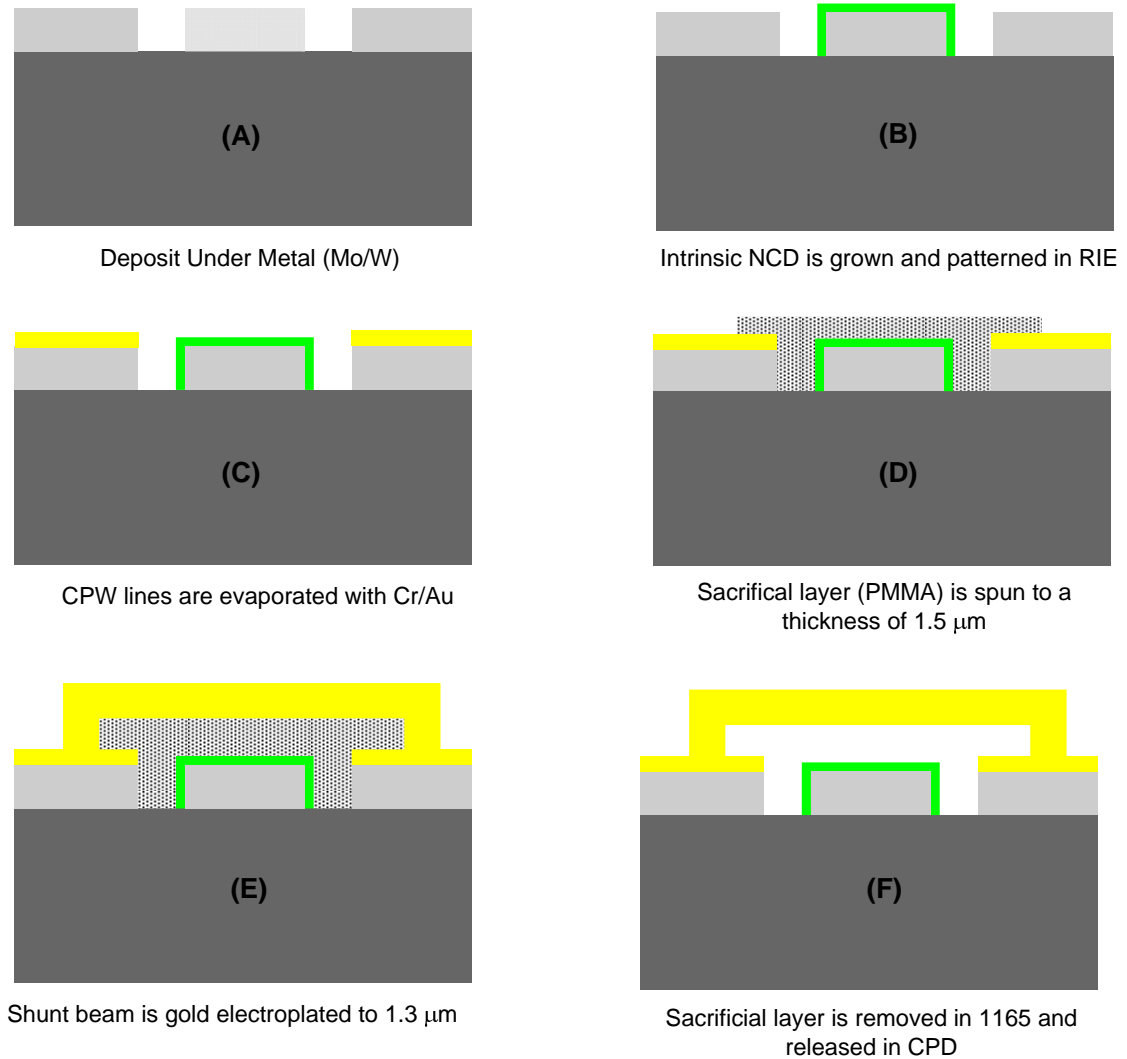
Figure 5.8 – Fabrication Procedure of the NCD Capacitive Switch

Figure 5.9(a) and Figure 5.9 (b) show microphotographs of the fabricated shunt switch. As seen in Figure 5.9 (b) there are holes in the movable membrane. In addition to permitting the removal of the sacrifical layer during the release process, the holes allow faster operation of the switch by reducing the air damping. The holes are 10 μm in diameter and spaced 10μm apart in a triangular lattice. The holes do contribute not change the capacitance in the up-state, but in the down-state they do decrease the total capacitance. In this work this effect is not taken into consideration.

(a)   (b)
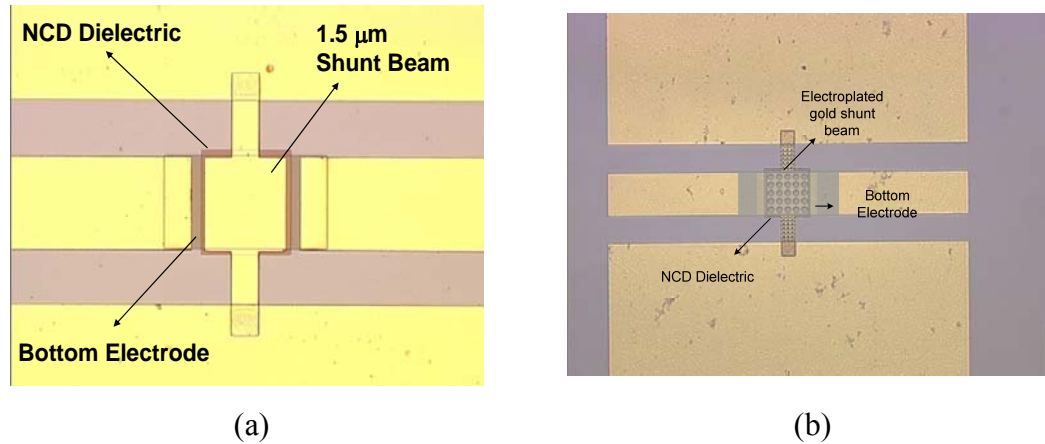
Figure 5.9 – Microphotograph of the Fabricated NCD Shunt Switch (a) Without Holes, (b) With Holes

5.4   Small Signal Measurements and Analysis

The switches are tested in the frequency range of 1-65 GHZ using an Anritsu Lightning VNA and 150 μm pitch probes on a Karl Suss semi automatic probe station. A standard center of thru TRL calibration routine is performed prior to the measurements. A Picosecond Pulse Labs bias-tee is used to protect the VNA ports from DC current and a Keithley 2400 source meter was used for the actuation of the shunt beams. The beams actuated at 22 volts drawing a current of 5-6 μA. Figure 5.10 and Figure 5.11 show the comparison of the simulated (from ADS momentum) and measured return loss and insertion loss of a switch in the up-state and down-state, respectively. The up-state insertion loss of 1.1 dB at ~50 GHz is predominantly due to mismatch loss cause by beam imperfections, as verified by the high S_{11} value; the loss factor calculated from the measured S-parameters is below 0.15 over the entire frequency range. An equivalent CLR circuit (explained in section 5.2) is used to extract the lumped element values in both the states from which the capacitance was found to be 50-55 fF in the up-state, and 0.74 pF in the down-state. The extracted inductance and resistance are 11.8 pH and 0.83 Ω, respectively. The switch was designed to yield a down-state capacitance of 1.26 pF and the discrepancy in the measured value can be attributed to roughness in the NCD dielectric film and possibly reduction in the actual contact area due to imperfect beam flatness, which reduces the net capacitance upon actuation. Table 5.2 shows the

80

comparison of the extracted lumped element values from the simulation and measurement. In addition to the roughness, the difference in overlap area during measurements is another reason for the difference in capacitance values.
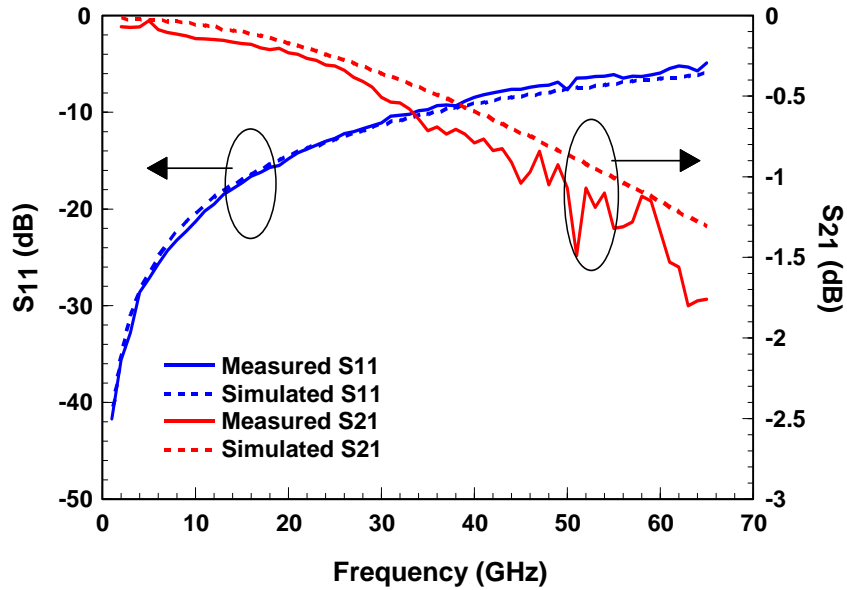
Figure 5.10 – Comparison of Simulated and Measured S_{11} and S_{21} in the Up-State of the NCD Capacitive Shunt Switch
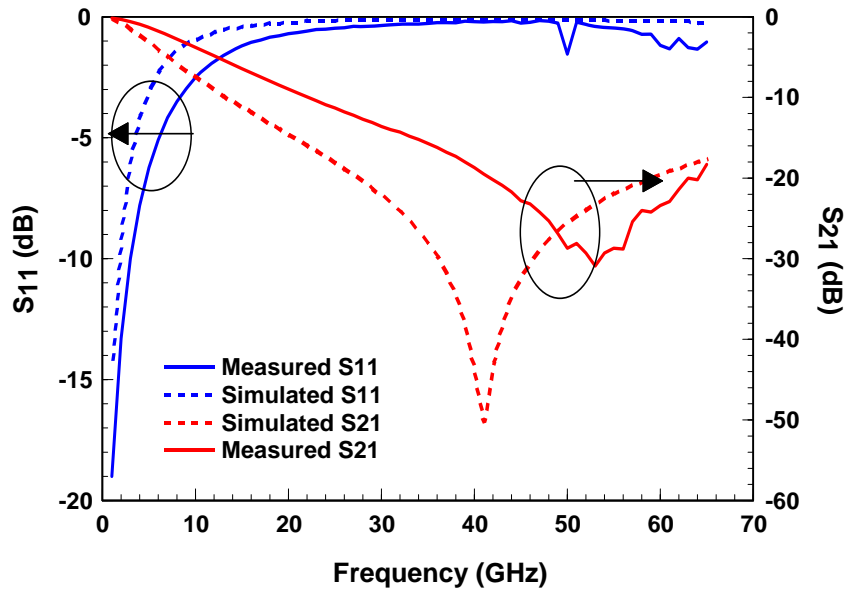
Figure 5.11 – Comparison of Simulated and Measured S_{11} and S_{21} in the Down-State of the NCD Capacitive Shunt Switch

81

Table 5.2 – Comparison of the Lumped Element Values of the Capacitive Switch from Simulations and Measurement

Design Name	L (pH)	R (ohms)	C_{up} (fF)	C_{down} (pF)
Design 1 (Simulated)	10.2	0.06	50	1.26
Design 1 (Measured)	11.8	0.8	55	0.75
Design 2 (Simulated)	40.8	0.06	50	1.26
Design 2 (Measured)	41.2	0.8	55	0.78

5.5   Corona Kelvin Measurements

The Corona Kelvin measurement (CKM) technique [97] is a non-destructive dielectric characterization method that does not require a top electrode and can therefore be used as an in-line process step. In this method, ions are generated at atmospheric pressure from air by putting a high potential on a short tip. These ions diffuse through air and are deposited on the substrate under test. The non-contact voltage is measured with a vibrating Kelvin probe relative to the grounded bottom electrode. In addition to the measured potential, this technique also computes the amount of ions deposited. Figure 5.12 shows the setup for CKM measurement. CKM is a well established technique in the CMOS industry and is accurate to 0.1mV under low voltage conditions (20 volts). Figure 5.13 and Figure 5.14 show the CKM-measured voltage decay for the nitride and diamond films, respectively, taken at three different sites across the wafers. It is evident from the data that both nitride and diamond are leaky, but the rate of voltage decay for the diamond film is considerably faster. The CKM method yields a voltage drop from 35 volts to 10 volts in ~2 minutes for the nitride films. The diamond films, due to the leaky nature have a voltage drop from 8 volts to tenths of a volt in approximately 10 seconds.
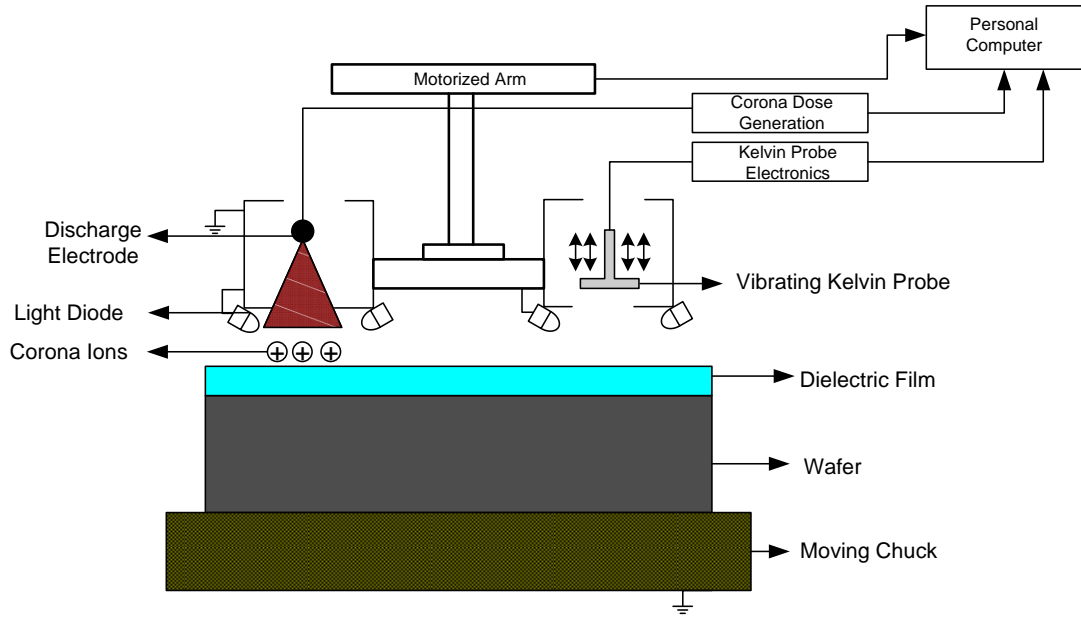
Figure 5.12 – Typical Setup for Corona Kelvin Measurement (CKM)
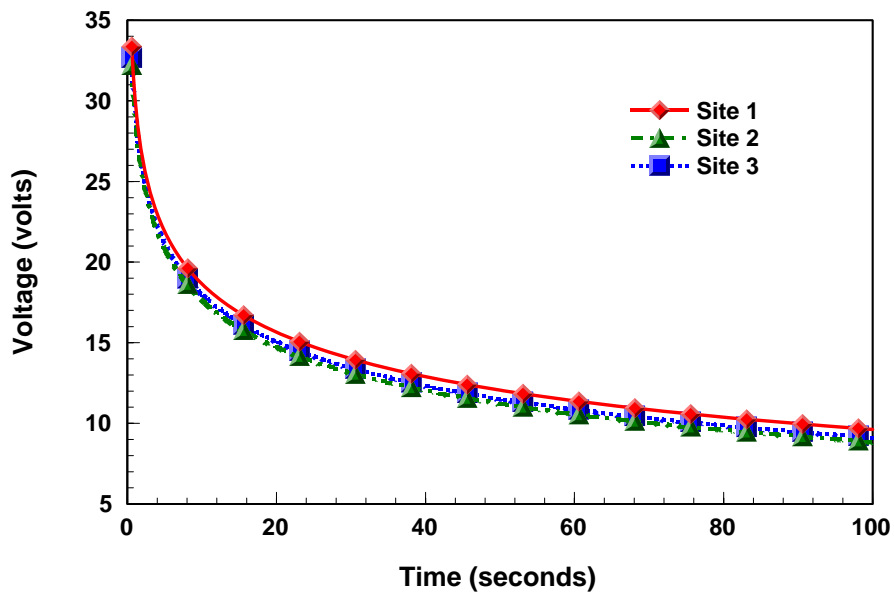
Figure 5.13 - Voltage Decay of Nitride Film at Three Different Sites of Samples Through
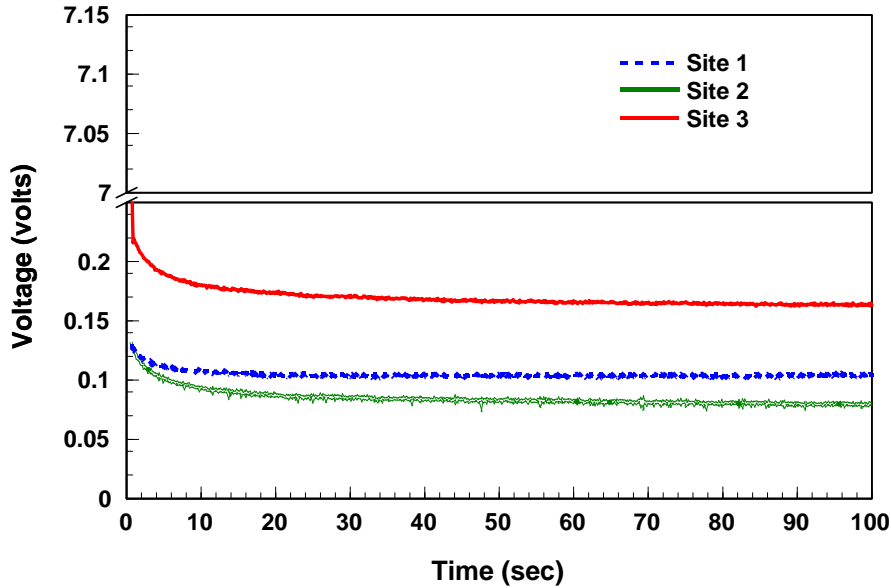
CKM Technique

Figure 5.14 – Voltage Decay of NCD Film at Three Different Sites of Samples Through CKM Technique

5.6 Stressed I-V and C-V Measurements – 1st Generation

In addition to CKM measurements, standard I-V and C-V tests are also performed to establish the non-charging nature of NCD films. For this test, metal-insulator-metal (MIM) and MEM structures using silicon nitride and NCD films are fabricated. The capacitor test structures were fabricated on high resistivity silicon substrates with molybdenum as the bottom electrode and the dielectric films were etched into small islands using standard etching recipes. The MEM devices did not work fine due to processing irregularities and hence the discussion is focused on the MIM structures. The MIM structures have a 0.7 μm thick bottom electrode made of molybdenum. The insulator material was grown to a thickness of 0.5 μm and the top metal was electroplated to a thickness of 1μm. The overall capacitance area of the MIM structure was 90 x 90 μm. I-V measurements are carried out using a 4140B picoammeter. Measurements are performed at dv/dt values of 0.25 volts/sec, 0.5 volts/sec and 1 volt/sec. Figure 5.15 and Figure 5.16 show the leakage current for different dv/dt values for the nitride and diamond film, respectively.
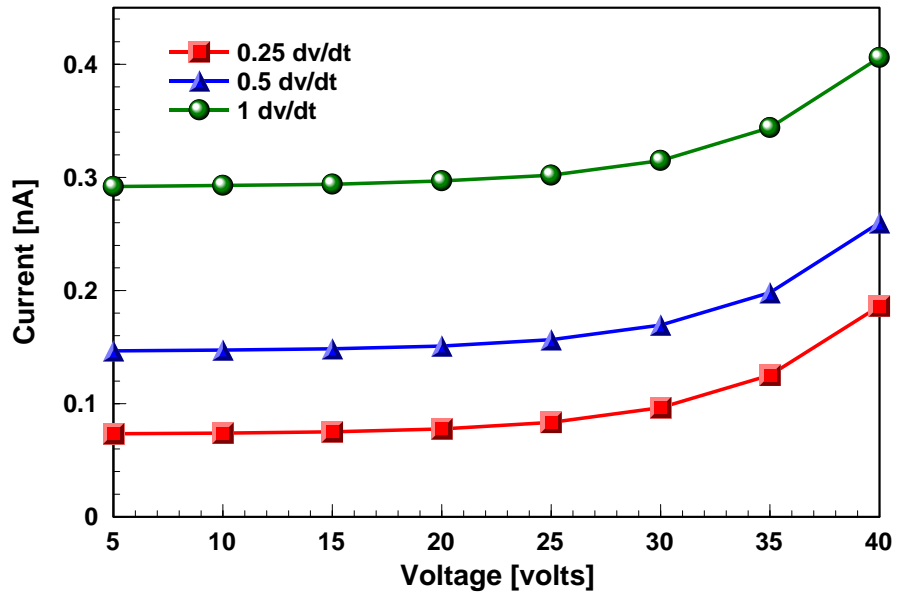
Figure 5.15 – Measured Leakage Current vs Voltage for Nitride Film with Different dv/dt
Values
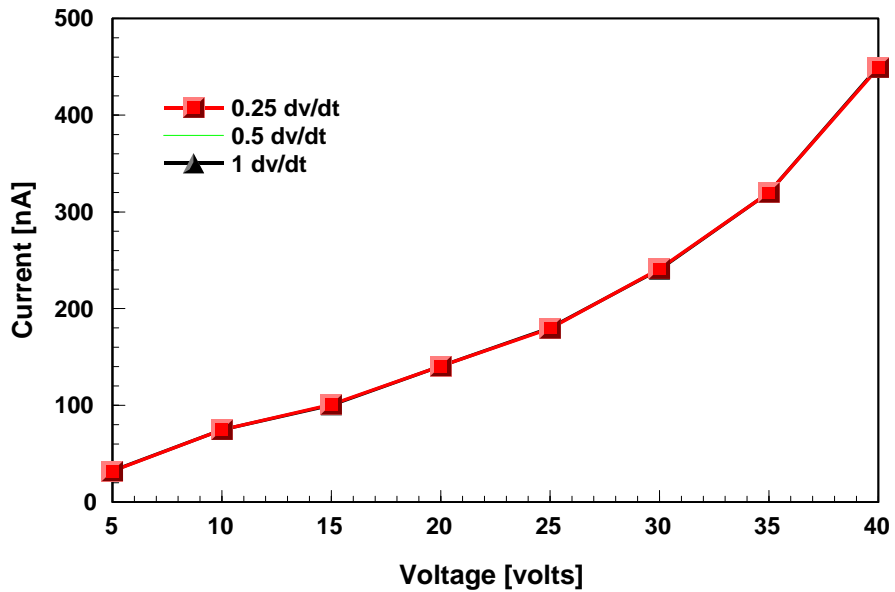
Figure 5.16 – Measured Leakage Current vs Voltage for NCD Film with Different dv/dt
Values

The leakage current (I) in the MIM capacitors is dependent on the capacitance (C), instantaneous rate of voltage (dv/dt), applied voltage (V), and conductance (1/R) as given in equation 5.5

$$I = \left(C * \frac{dv}{dt} \right) + \frac{V}{R} \tag{5.5}$$

Although both nitride and diamond films exhibit a non-linear I-V behavior, the strong dependence on the dv/dt term for the nitride film allows the capacitance value (~3.4 pF) to be extracted. For the diamond films the 1/R term dominates due to the conductive path provided by the diamond grain boundaries in the cluster, leading to leakage current in the μA range. In addition to basic I-V measurements, leakage current testing under stress conditions is also performed. Figure 5.17 and Figure 5.18 show the stress induced leakage current (SILC) measurements for nitride films stressed at 20 volts and 40 volts, respectively. These tests are carried out different periods of time (20 mins, 2 hours and 5 hours). The tests performed at 20 volts have little to no effect on the leakage current value. This is evident from the graph in Figure 5.17 wherein the leakage current is almost constant after the SILC testing.
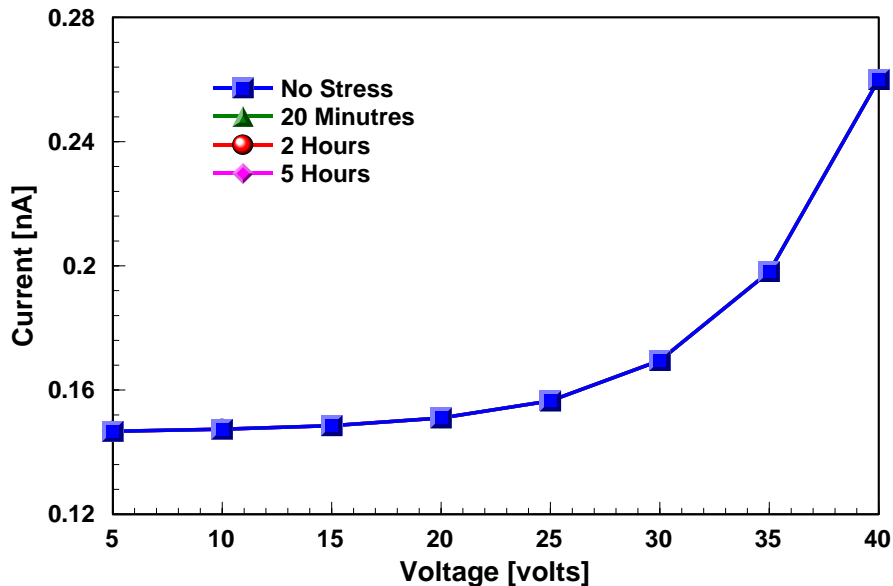
Figure 5.17 – Stress Induced Leakage Current (SILC) for Nitride Films Stressed at 20 Volts for Different Periods of Time

In Figure 5.18, the capacitors stressed at 40 volts show an increase in current after the SILC tests. This increase in current can be attributed to trapped charges which lower the effective stress voltage of the dielectric layer. Increase in current can be a result of barrier lowering due to electron de-trapping or the effect of SILC [98]. Unlike barrier lowering, the SILC process creates a permanent defect on the dielectric layer which is irreversible. Stress testing creates a high resistance breakdown spot in the dielectric layer and is very hard to detect during in-situ measurements. The initial defect created during the SILC testing gets propagated overtime resulting in a dielectric breakdown.
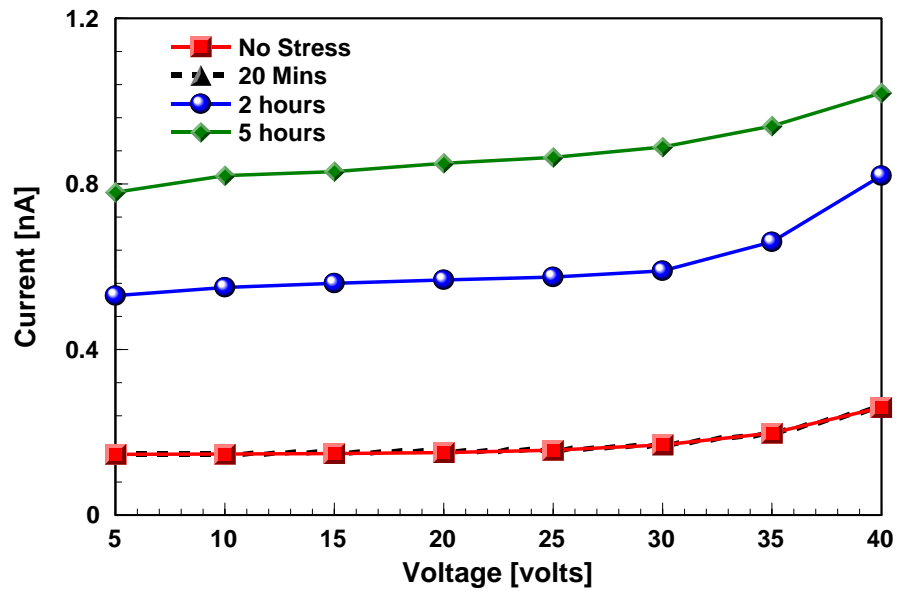
Figure 5.18 – Stress Induced Leakage Current (SILC) for Nitride Films Stressed at 40 Volts for Different Periods of Time

Figure 5.19 and Figure 5.20 show the SILC results for diamond films which are stressed at 20 volts and 40 volts, respectively. It is evident from the graphs that stress induced charge does not affect or increase the leakage current before and after the tests. Unlike nitride films where the charges create defects, the leaky nature of NCD films does not allow the charge to be stored on the surface or in the bulk of the material. NCD capacitors were also tested under stress conditions of 60 volts but this resulted in the increase of leakage current to milliamps. Unlike in silicon nitride and oxide where milliamps of leakage current correspond to dielectric break down, the dielectric

properties of NCD films are not altered. C-V measurements are done to confirm this that the NCD films retain their dielectric properties. The results of the C-V measurements are shown in Figure 5.21.
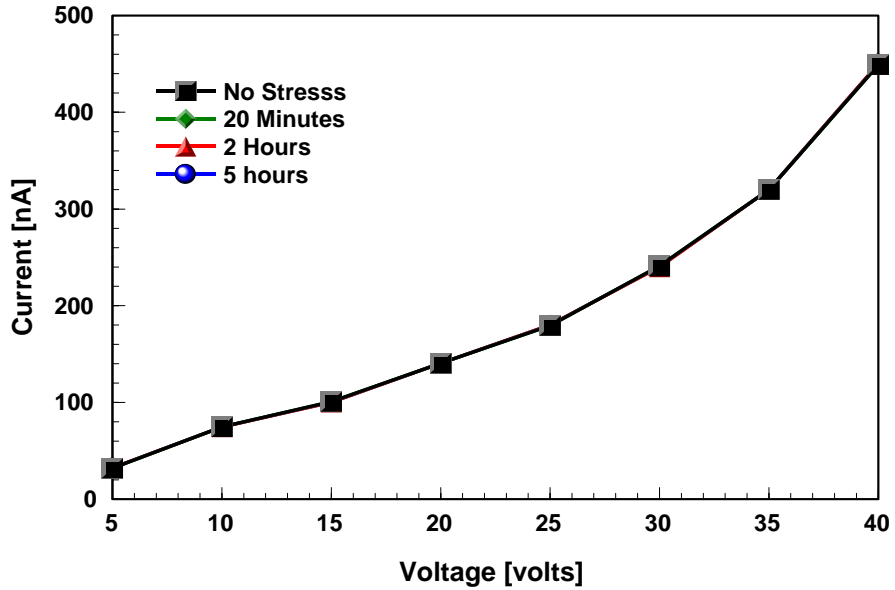
Figure 5.19 – Stress Induced Leakage Current (SILC) for NCD Films Stressed at 20 Volts for Different Periods of Time
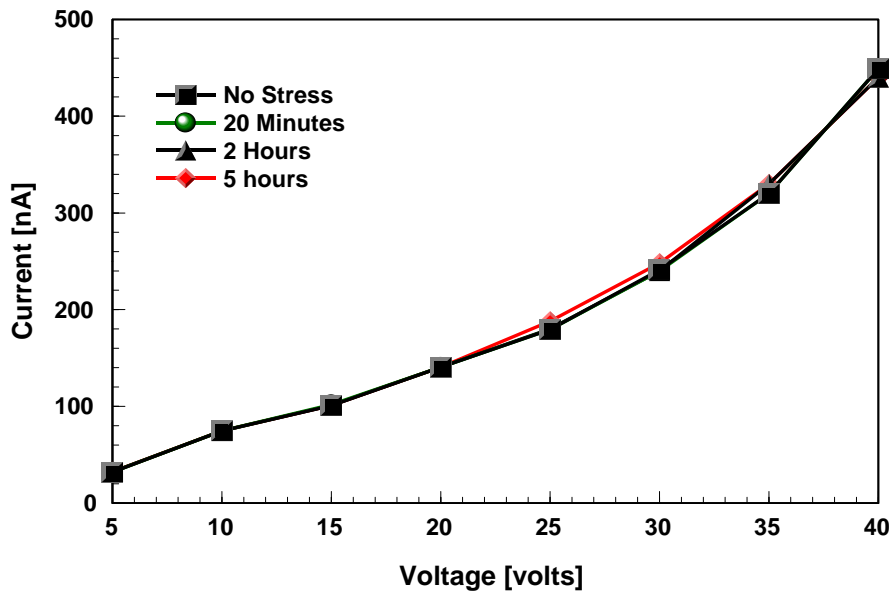
Figure 5.20 – Stress Induced Leakage Current (SILC) for NCD Films Stressed at 40 Volts for Different Periods of Time
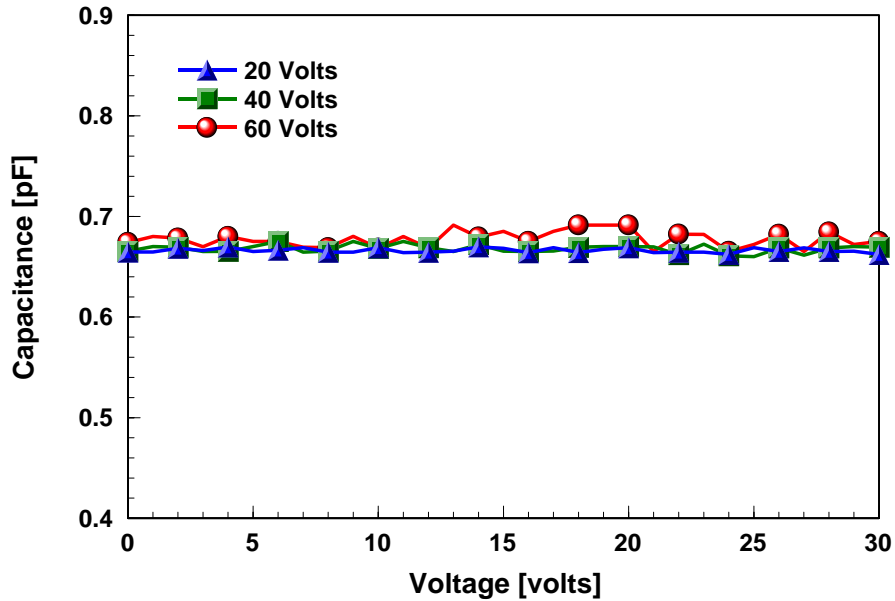
Figure 5.21 – Capacitance Measurement of the NCD Capacitors Before and After Stress
Tests

5.7   Stressed I-V and C-V Measurements – 2nd Generation

In the second generation switches, tungsten is used as the bottom electrode instead of molybdenum. Tungsten is sputtered with Ti as a seed layer. The thickness of the heterostructure is deposited close to 9000 A^0. Silicon nitride and NCD films are once again deposited through CVD technique followed by a top electrode of gold. In this version, the MEM structures are also fabricated. For the MEM structures, after patterning the dielectric layer, PMMA, which is used as the sacrificial layer is patterned to a thickness of 1 micron. The top electrodes are gold electroplated to a thickness of 1 μm. For this set of measurements dielectric layers (both Si_3N_4 and NCD) of different thicknesses are used. This is done for the MIM and MEM structures to understand the effect of thickness on the I-V and C-V measurements under stress conditions. Although the growth conditions were closely monitored a small difference of 100-200 A^0 in the final thickness is seen. Although this difference is crucial in many transistor applications, for this work the effect due to the difference in thickness is ignored.

Figure 5.22 and Figure 5.23 show I-V measurements for the MIM nitride and NCD capacitors. The dielectric thickness of the nitride capacitors is 1400 A^0 and for

NCD is 1500 A^0. The area of the capacitors being tested is 90 µm X 90 µm. In order to avoid dielectric break down the capacitors are tested by gradually increase the voltage. For the nitride films, the leakage current values are low initially up to 15 volts beyond which the current increases and dielectric break down occurs 30 volts. In the second generation tests, all stress measurements are performed for duration of 1 hour.
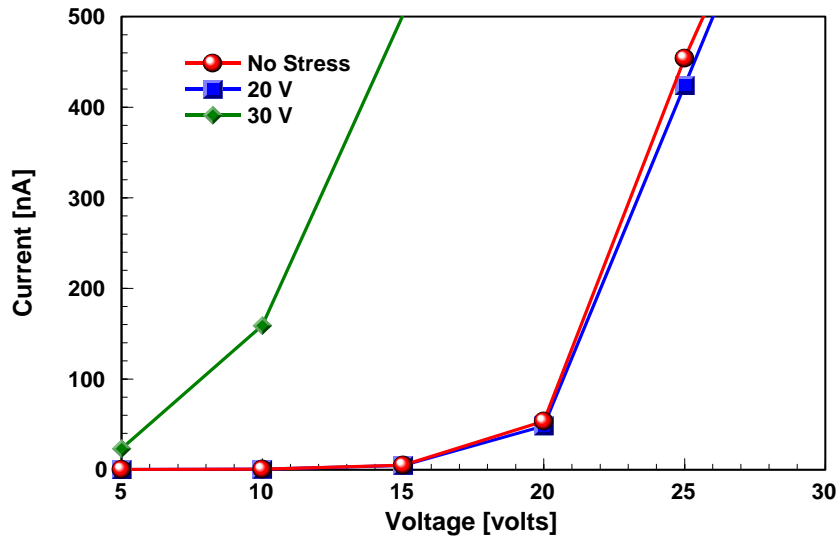
Figure 5.22 – Stress Induced Leakage Current (SILC) for Nitride MIM Capacitor with Dielectric Thickness of 1400 A^0
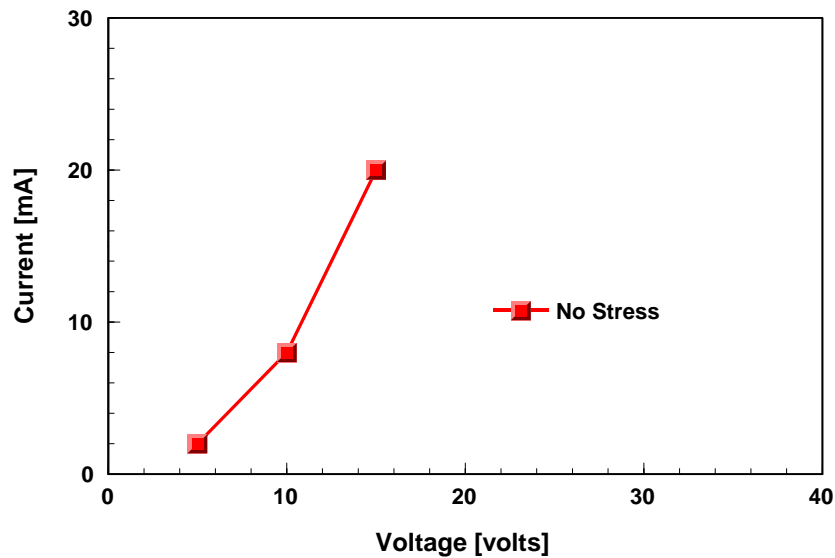
Figure 5.23 – Stress Induced Leakage Current (SILC) for NCD MIM Capacitor with Dielectric Thickness of 1500 A^0

90

The growth time for the diamond film is too short (~ 1 hour) causing many defects, openings and voids in the film which result in a short upon application of an electric field. As the measured leakage current is in the order of mA in the first measurement, no stress tests are performed for the NCD capacitors. This claim can be confirmed by the very high capacitance value (~ 400 pF) as shown in Figure 5.24. Surface defects in the diamond film lead to a through conductive path between the bottom and top electrode. In this work undoped NCD films exhibits dielectric behavior for thicknesses above 0.3 μm.
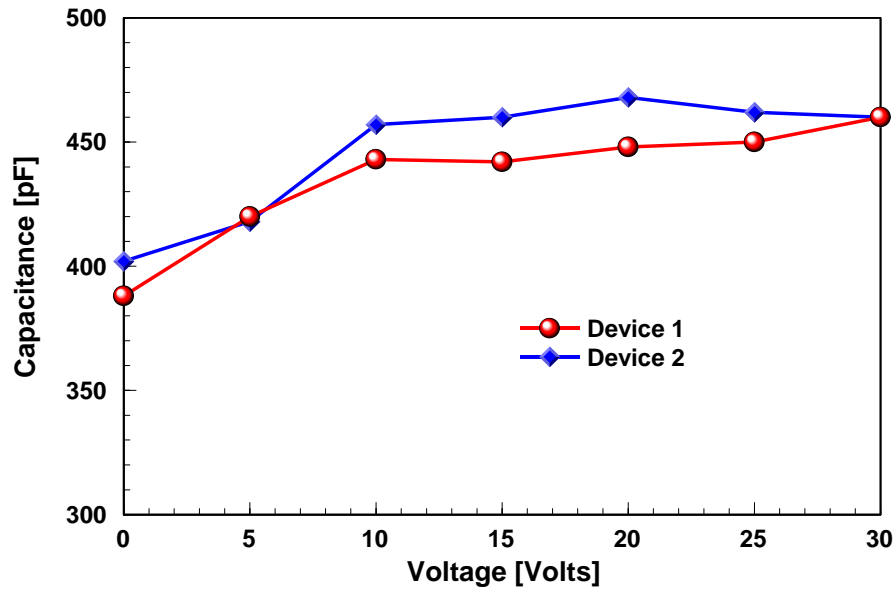
Figure 5.24 – Capacitance Measurement of 1500 A^0 NCD MIM Capacitor

MIM capacitors with 0.5 μm thick dielectric layers are used for the I-V stress tests. These tests, similar to the first generation switches, are carried out for both the nitride and diamond capacitors. Figure 5.25 and Figure 5.26 show the I-V response for the nitride and NCD capacitors, respectively. The MIM structures are stressed at different voltages for more than 1 hour. The nitride based capacitors exhibit an increase in leakage current after the stress tests. At higher fields (> 65 volts), the nitride capacitors are dominated by the Fowler-Nordheim [99] tunneling effect. This effect is not seen in the NCD based capacitors, wherein the higher conductivity in the diamond film dominates the increase in current in comparison to the nitride films.
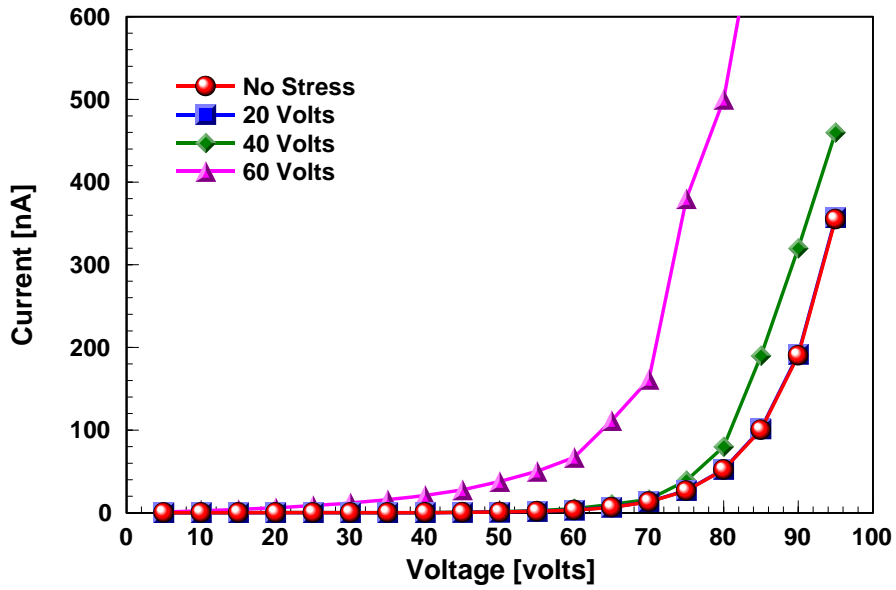
Figure 5.25 – Stress Induced Leakage Current (SILC) for Nitride MIM Capacitor with Dielectric Thickness of 5000 A^0
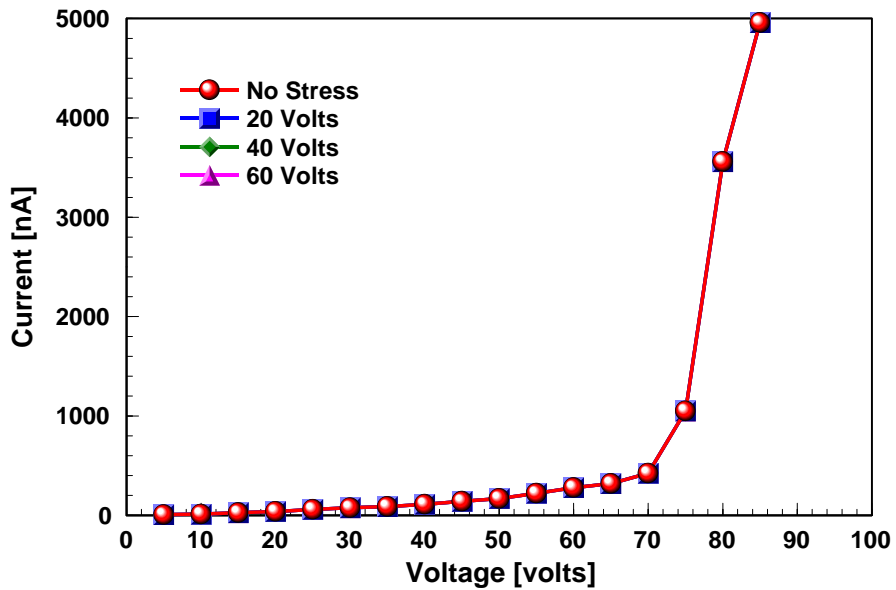
Figure 5.26 – Stress Induced Leakage Current (SILC) for NCD MIM Capacitor with Dielectric Thickness of 5000 A^0

For comparison purposes, Figure 5.27 shows the leakage current measurements for the nitride and NCD capacitors in the log scale. The graph shows the leakage current

value for the capacitors under no stress and 60 volts of stress. It is evident from the results, that there is a shift observed in the nitride capacitors where as the value does not alter in the case of NCD capacitors.
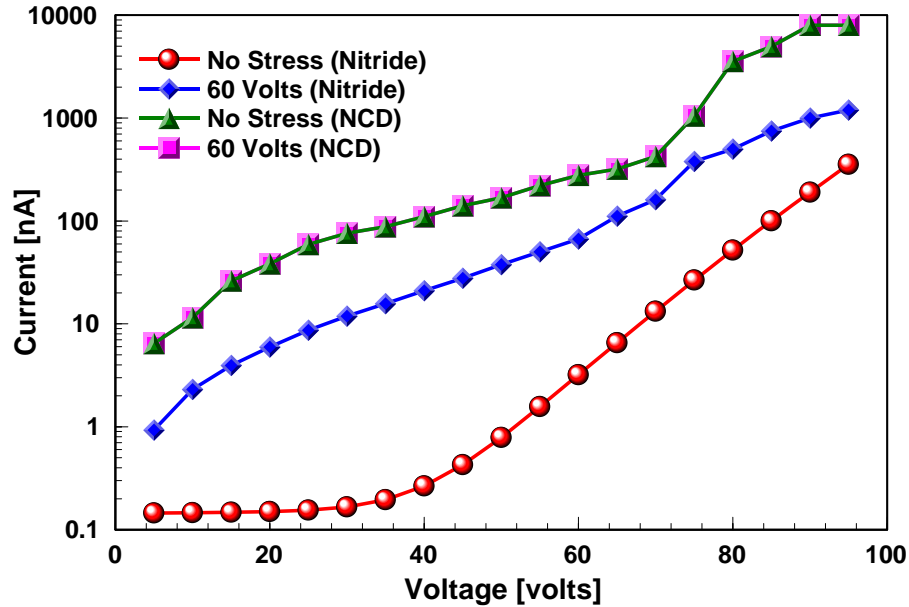
Figure 5.27 – Comparison of Stress Induced Leakage Current (SILC) in Log Scale for 5000 A^0 NCD and Nitride Capacitors

In comparison to the first generation measurements, the new set of SILC tests are carried for different thickness for both the nitride and NCD films and they show a better performance in terms of low leakage current for the films. From the measurements, tungsten is better suited as the under metal in place of molybdenum. The SILC tests for NCD based MEM capacitors are carried out by observing the shift in leakage current and actuation voltage, both as a function of time. The MEM capacitors actuate at ~ 35 volts. Figure 5.28 shows the I-V response of the MEM capacitor in the non actuated state. There is no shift in the current response upto 30 volts which equates to no change in actuation voltage, after 2 hours of testing. When the membrane actuates and falls on the dielectric layer the current value increases from nA in the up-state to μA in the down-state as shown in Figure 5.29. In comparison to the popular dielectric (nitride or oxide) based capacitive switches, repeated actuation of the switches will lead to a shift in the actuation voltage. This problem along with the charge accumulation in the dielectric layer

will eventually lead to the failure of the switches. Further progress is underway to test the switches for a longer time to check its reliability.
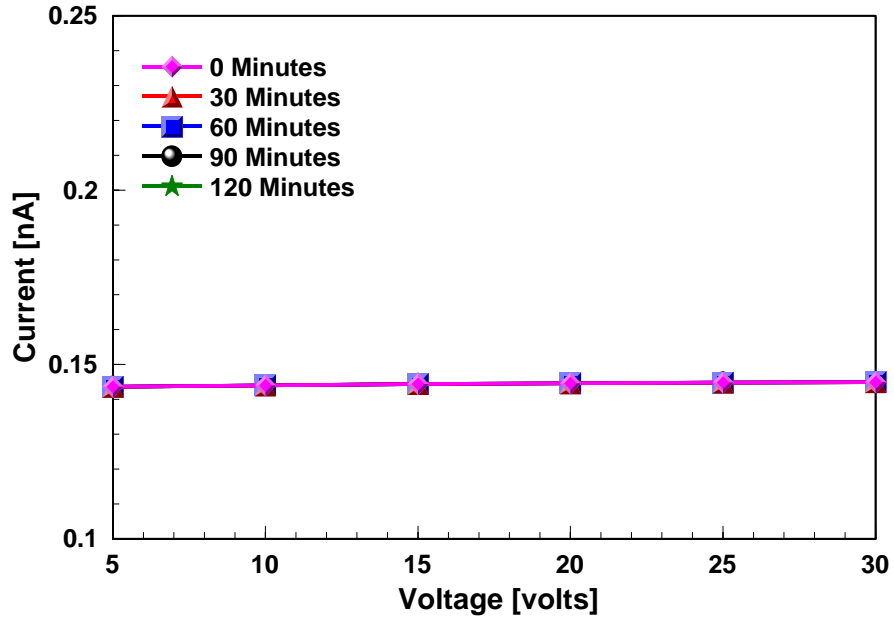
Figure 5.28 – Measured I-V Response for the NCD MEM Capacitor in the Up-State
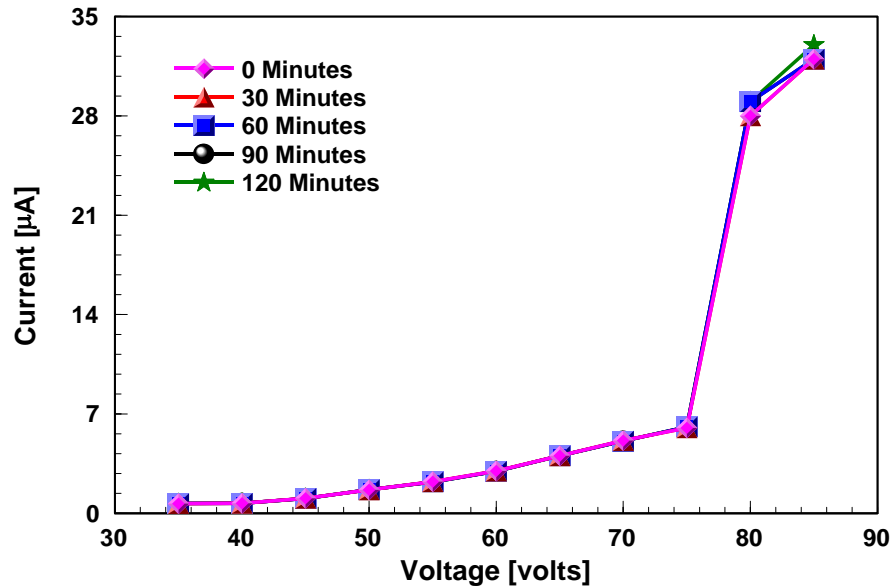
Figure 5.29 – Measured I-V Response for the NCD MEM Capacitor in the Down-State

94

5.8   Summary

Capacitive shunt switches using undoped NCD film have been designed, fabricated and tested till 65 GHz. The switches are electrostatically actuated and the measurements show an insertion loss of 1.1 dB and an isolation of 30 dB at ~50 GHz, respectively. The measured capacitance in the down-state of the beam is 0.75pF in comparison to 1.26 pF from simulation results obtained from ADS. The difference in capacitance can be attributed to the roughness of the dielectric layer and the difference in overlap area when the beam is actuated. Charging studies are performed for the nitride and NCD films using CKM metrology and stressed I-V measurements. SILC measurements are carried out for the capacitors using both Mo and W as the bottom electrodes for various dielectric thicknesses. The leaky nature of the NCD films is proven through these measurements. Although static power consumption is an issue with NCD capacitors, they can be used in applications which demand little to no degradation in performance and allow microwatts of power consumption.

Chapter 6

Summary and Recommendations

6.1 Summary

The work presented in this dissertation was focused on developing RF-MEMS and microwave devices based on NCD thin films. The research was multi-disciplinary and included thin film development and analysis (material science), mechanical characterization of NCD to realize compressively stressed films (mechanical engineering) and developing high power RF-MEMS devices based on NCD actuators and capacitive shunt switches with NCD as a dielectric (microwave engineering). Furthermore, this research presented the life cycle of a NCD based RF-MEMS starting from growth, proceeding to the design, fabrication and integration of the device and finishing with the measurement and modeling of the fabricated device.

Growth recipes for developing intrinsic and doped NCD films along with different seeding techniques using microwave plasma and hot filament CVD techniques have been presented in detail. Mechanical characterization techniques to measure the Young's modulus, first order resonant frequency and intrinsic stress of the grown NCD films have been demonstrated. A Young's modulus of 1020 GPa was measured using a non-destructive technique. The films were intentionally grown with built in compressive stress and the measured values were in the range of 140- 560 MPa. Measured results for the effect of different growth parameters that include temperature, pressure and gas ratio on the intrinsic stress developed in the films have been presented.

NCD based RF-MEMS actuators were designed for high power applications wherein diamond based devices were designed, fabricated and tested to generate switches and inductors in CPW and microstrip topologies. The thermally actuated diamond bridges operated in a bi-stable mode and the design to generate this bi-stable operation was studied using mathematical formulae from beam analysis. Mechanical and

electromagnetic simulations were performed using ANSYS^{TM} and ADS^{TM}, respectively to understand mechanical and electrical properties of the diamond actuators. Small signal S-parameter measurement was performed in the frequency range of 1-40 GHz on the integrated switches. Measured results show a return loss and insertion loss of 20 dB and 0.2dB, respectively, at 20GHz. Furthermore, tunable inductors were designed and fabricated in a CPW topology. Measurements were carried out in the frequency range of 1-30GHz and the measured results show an inductance ratio of 2.2 at 30 GHz. Large signal (high power) measurements were performed on both mechanically-actuated diamond switches in the power range of 24-47 dBm and on electrically actuated switches (that use a dual actuation scheme) in the range of 24-40 dBm. The measurements show an insertion loss of 0.2-0.3 dB in the entire power spectrum. The switches did not show any mechanical degradation and depreciation in the RF performance for the limited period in which the tests were performed.

NCD films were also used as insulators in capacitive shunt switches to address reliability issues due to charging. Prior to the design, material characterization studies were performed to grow intrinsic NCD films on metal thin films. A carbide forming layer was necessary to facilitate NCD growth. Diamond films were successfully grown on Mo and W thin films with moderate roughness (~ 8-9 nm). The electrostatically actuated switches were simulated in Agilent's ADS and an equivalent circuit was generated to extract the lumped element values of the switch model. The switches were fabricated on a high resistive silicon substrate using standard surface micromachining techniques. Small signal measurements were performed in the frequency range of 1-65 GHz with insertion loss of 1.1 dB and an isolation of 30 dB at ~50 GHz, respectively. Preliminary charging studies were performed using the CKM and I-V techniques for nitride and NCD films and both methods demonstrate the relatively leaky nature of the diamond dielectric film. Despite the finite conductivity of the NCD film, however, the measured loss of the switch is dominated by mismatch loss due to imperfections in the MEM beam. These NCD based switches can be used in applications where microwatt of power consumption is permitted without any depreciation in performance for a longer duration of time. This

balance between microwave loss and DC conductivity may prove to be an effective method to mitigate dielectric charging.

6.2   Recommendations for Future Work

In order to realize switches with better performance, the shunt switches can be fabricated with using tungsten as the bottom electrode. This could possibly account for the difference in the down-state capacitance value during actuation. Furthermore, a thorough theoretical analysis can be carried out to better understand the different regions in the leakage current measurements. Reliability measurements for both the diamond actuators at higher power levels and the capacitive switches should be performed for a longer period of time. The fabricated NCD actuators and NCD capacitive switches could be tested in switching speed measurements. Figure 6.1 shows the typical set up which will be used for the switching speed measurements. The 10 GHz signal source will be modulated and the diode detector converts the RF signal into DC. An oscilloscope will be used to compare the modulated and driving waveform to measure the switching speed.
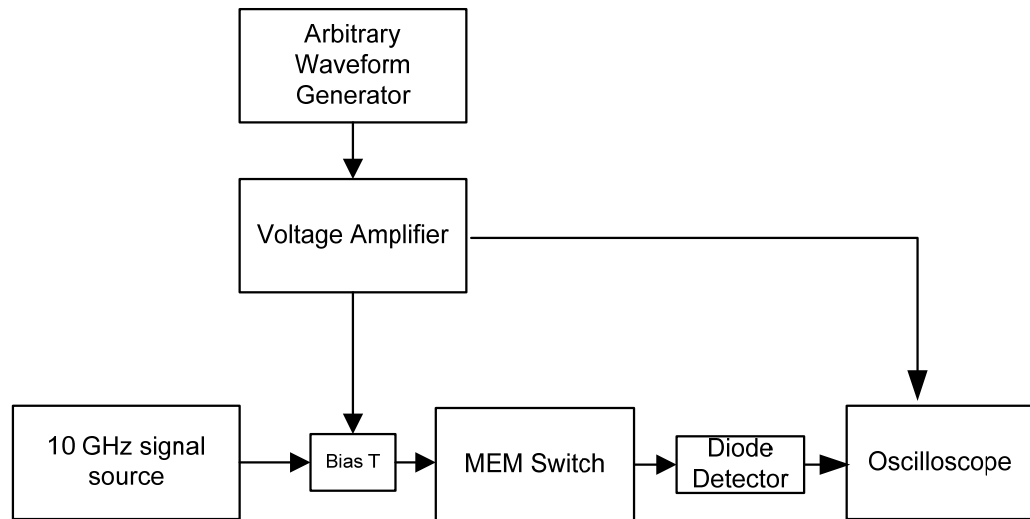
Figure 6.1 – Block Diagram for Switching Speed Measurement

Temperature-based studies on the diamond actuators will highlight the performance of the switch which includes microwave measurements and mechanical stability under low and elevated temperature conditions. The outstanding thermal

conductivity of NCD thin films can be useful in their operation. As an improvement to the current design, the contacts pads which are currently of platinum can be substituted with doped diamond; the low temperature UNCD films introduced by Argonne National Laboratories can be used. After electroplating copper, a thin film Mo or W can be deposited over which doped UNCD films can be grown. Repeated actuation under hold and cold switching conditions will have little to no effect on the contact due to the outstanding mechanical and material characteristics of diamond films.

NCD based distributed MEMS transmission line (DMTL) phase shifters can be designed to operate in the K band. Diamond actuators designed and tested in this work will be used to generate these phase shifters. Figure 6.2 shows the layout of the phase shifter. In this design 10-12 switches will be fabricated on a single silicon frame and actuated using the dual (thermal + electrostatic) actuation scheme. The first generation 9 section phase shifter that were successfully fabricated. But due to the excessive compressive stress in each individual switches resulted in the switches breaking from the silicon frame. In designing such NCD based DMTL phase shifters, it is very important to understand and control the stress build up during the diamond growth process.
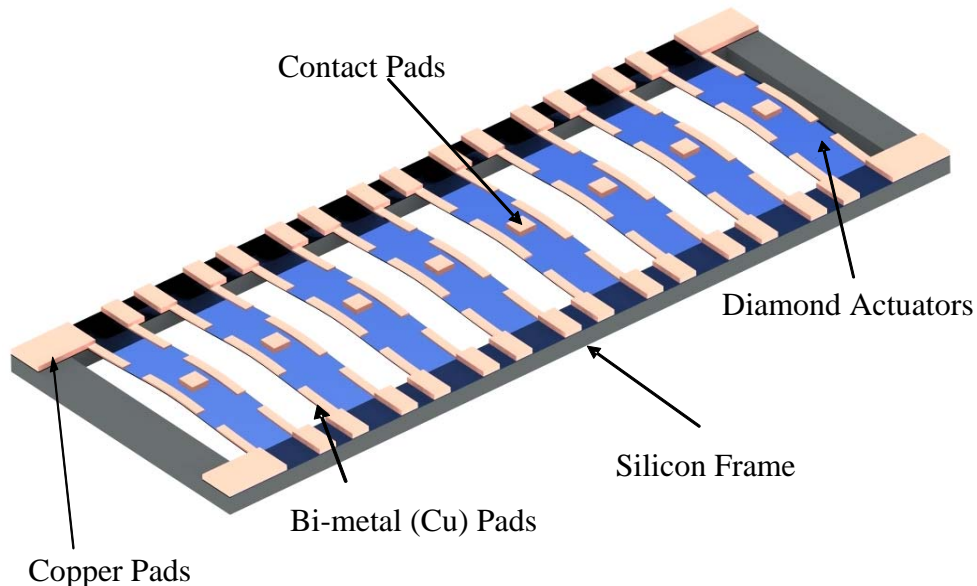
Figure 6.2 – Layout of the Multi-Bit DMTL NCD Phase Shifter

99

Ferroelectric films are widely used in the microwave community as thin films to generate tunable phase shifters, varactors, circulators etc. But their performance at high frequencies is limited due to high insertion loss and single degree of freedom in capacitive tuning. Combining UNCD and ferroelectric films will help overcome these limitations. Barium strontium titanate (BST) will be the ferroelectric material used for investigation. BST films need to be annealed during the deposition process or post annealed after deposition. UNCD films which offer outstanding thermal properties will be ideal for depositing BST. Sputtering, PLD and sol-gel techniques could be used for this investigation. Characterization tools such as SEM, AFM, XRD and Raman spectroscopy will be helpful used to investigate these heterostructures. This proposed thin film research will be the first of its kind to merge ferroelectric and diamond films.

RF-MEMS/NEMS devices based on UNCD and BST heterostructures can be developed. Tunable MEMS capacitors with BST and UNCD will provide great range in tunability and also controlling charging issues and parasitic losses thereby increasing the overall Q at microwave frequencies. High power terminations and attenuators based on doped UNCD films can be developed. These will be a good candidate to replace the high power attenuators which are made of bulk substrates like aluminum nitride and beryllium oxide. The tunable switches could be further integrated with the UNCD high power attenuators to realize phase and amplitude controlled circuits. Finally true time delay (TTD) phase shifters integrating BST and UNCD films wherein the dual mode actuation scheme will be used to facilitate a multi bit 10-12 section UNCD actuator will be integrated to a host substrate with the heterostructure dielectric layer.

References

1. Hector J.DeLos Santos, "Introduction to microelectromechanical microwave Systems", Boston Artech House, 1999.

2. Varadan V.K, "RF MEMS and their applications", John Wiley & Sons, Inc. 2003.

3. Larry E. Corey, "Radio frequency micro-electro-mechanical switches (RF MEMS) Improvement Program," Pre-solicitation Conference, Oct 19 2001.

4. Gregory T.A.Kovacs, "Micromachined transducers sourcebook", McGraw-Hill Publishers, 1998.

5. Source: http://newton.ex.ac.uk/research/qsystems/people/sque/

6. S.Bhattacharyya et al., "Synthesis and characterization of highly-conducting nitrogen-doped ultrananocrystalline diamond films", Applied Physics Letters, Vol.79, No.10, pp.1441-1443, 2001.

7. G.M.Rebeiz, "RF MEMS- Theory, design and technology", John Wiley and Sons Publication, 2003.

8. V.Milanovic et al., "Batch transfer integration of RF microrelays", IEEE Microwave and Guided Wave Letters, Vol.10, No.8, pp.313-315, August 2000.

9. P.Blondy et al., "Packaged mm-wave thermal MEMS switches", 31st European Microwave Conference, pp.1-4, September 2001.

10. H.C.Lee et al., "Piezoelectrically actuated RF MEMS DC contact switches with low voltage operation", IEEE Microwave and Guided Wave Letters, Vol.15, No.4, pp.202-204, April 2005.

11. G.M. Rebeiz and J.B. Muldavin, "RF MEMS switches and switched circuits," IEEE Microwave Magazine, Vol.2, No.4, pp.59-71, December 2001.

12. B.Schauwecker et al., "Serial combination of ohmic and capacitive RF MEMS switches for large broadband applications", IEEE Electronic Letters, Vo.40, No.1, January 2004.

13. C.L. Goldsmith et al., "Performance of low-loss RF MEMS capacitive switches," IEEE Microwave and Guided Wave Letters, Vol.8, No.8, pp.269-271, August 1998.

14. H.A.C.Tilmans et al., "Wafer level packaged RF-MEMS switches fabricated in a CMOS fab", International Electron Devices Meeting, pp.41.4.1-41.4.4, December 2001.

15. Larry E. Corey, "Radio Frequency Micro-Electro-Mechanical Switches (RF MEMS) Improvement Program," Pre-solicitation Conference, October 2001.

16. Electronic Reference: http://en.wikipedia.org/wiki/Piezoelectric

17. Electronic Reference: http://en.wikipedia.org/wiki/Lorentz_force

18. P.Schmid et al., "Diamond switch using new thermal actuation scheme", Diamond and Related Materials, Vol.12, No.3-7, pp.418-421, March-July 2003.

19. D.Saias et al., "An above IC MEMS RF switch", IEEE Journal of Solid State Circuits, Vol.38, No.12, pp.2318-2324, December 2003.

20. B.Lakshminarayanan et al., "High power high reliability sub-microsecond RF MEMS switched capacitors", IEEE International Microwave Symposium, pp.1801-1804, June 2007.

21. T. Ketterl et al., "MEMS Series Switch with Nanometer Wide Gaps in Suspended Coplanar Waveguide Transmission Lines", IEEE International Microwave Symposium, pp.255-258, June 2006.

22. B.Lakshminarayanan et al., "High reliability miniature RF MEMS switched capacitors", IEEE Transactions on Microwave Theory and Techniques, Vol.56, No.4, pp.971-981, April 2008.

23. D.Sparks et al., "Reliable Vacuum Packaging Using NanoGetters[TM] and Glass Frit Bonding", Proceedings of SPIE, pp.5343-5346, January 2004.

24. Technological developments by Teravicta Technologies Inc.

25. Technological developments by XCOM Wireless.

26. J.R.Reid et al., "Measurements of charging in capacitive microelectromechanical switches," Electronic Letters, Vol.38, No.24, pp.1544-1545, November 2002.

27. W.M.van Spengen et al.,"A comphrensive model to predict the charging and reliability of capacitive RF MEMS switches", Journal of Micromechanical. Microenginerring, No.14, pp.514-521, Jan 2004.

28. X.Yuan et al., "Initial observation and analysis of dielectric charging effects on RF MEMS capacitive switches", IEEE International Microwave Symposium, pp.1943-1946, June 2005.

29. G.J.Papaioannou et al., "On the dielectric polarization effects on capacitive RF MEMS switches", IEEE International Microwave Symposium, pp.761-764, June 2005.

30. R.W.Herfst et al., "Center-shift method for the characterization of dielectric charging in RF MEMS capacitive switches", IEEE Transactions on Semiconductor Manufacturing, Vol.21, No.2, pp.148-153, May 2008.

31. G.Papaioannou et al., "Temperature study of the dielectric polarization effects of capacitive RF MEMS switches", IEEE Transactions on Microwave Theory and Techniques, Vo.53, No.11, pp 3467-3473, November 2005.

32. H.San et al., "Using metal-insulator-semiconductor capacitor to investigate the charge accumulation in capacitive RF MEMS switches", 3rd IEEE International Conference on Nano/Micro Engineered and Molecular Systems, pp.1048-1052, 2008.

33. F.W.DelRio et al., "Atomic layer deposition of Al_2O_3/ZnO nano-scale films for gold RF MEMS", IEEE International Microwave Symposium, pp.1923-1926, June 2004.

34. J.R.Webster et al., "Performance of amorphous diamond RF MEMS capacitive switch", IEEE Electronic Letters, Vol.40, No.1, pp.221-223, January 2004.

35. J.Chee et al., "DC-65 GHz characterization of nanocrystalline diamond leaky film for reliable RF MEMS switches", 35th European Microwave Conference, pp.581-584, October 2005.

36. C.Bordas et al., "Carbon nanotube based dielectric for enhanced RF MEMS reliability", IEEE International Microwave Symposium, pp.375-378, June 2007.

37. B.Pillans et al., "Schottky barrier contact based RF MEMS switch", IEEE Journal of Microelectromechanical Systems, Vol.17, No.6, pp.1439-1446, December 2008.

38. S.Melle et al., "Reliability modeling of capacitive RF MEMS", IEEE Transactions on Microwave Theory and Techniques, Vol.53, No.11, pp.3482-3488, November 2005.

39. R.W.Herfst et al., "Identifying degradation mechanisms in RF MEMS capacitive switches", IEEE MEMS Conference, pp.168-171, January 2008.

40. P.Czarnecki et al., "New insights into charging in capacitive RF MEMS switches", 46th Annual International Reliability Physics Symposium, pp.496-505, April 2008.

41. D.Hyman et al., "GaAs-compatible surface micromachined RF MEMS switches", IEEE Electron Letters, Vol.35, No.3, pp.224-226, 1999.

42. D.Peroulis et al., "RF MEMS switches with enhanced power-handling capabilities", IEEE Transactions on Microwave Theory and Techniques, Vol.52, No.1, pp.59-68, January 2004.

43. B.Ducarouge et al., "Power capabilities of RF MEMS", 24th International Conference on Microelectronics, Vol.1, pp.65-70, May 2004.

44. D.Hyman et al., "Contact physics of gold microcontacts for MEMS switches", IEEE Transactions on Components and Packaging Technology, Vol.22, No.3, pp.357-364, September 1999.

45. J.Muldavin et al., "Power handling and linearity of MEM capacitive switches", IEEE International Microwave Symposium, Vol.3, pp.1915-1918, June 2003.

46. B.Pillans et al., "RF power handling of capacitive RF MEMS switches", IEEE International Microwave Symposium, pp.329-332, June 2002.

47. J.D.Martinez et al., "Surface and bulk micromachined RF MEMS capacitive series switch for watt-range hot switching operation", IEEE European Microwave Conference, pp.1237-1240, October 2007.

48. C.Goldsmith et al., "Update on RF MEMS switch reliability", Technical Report 2009.

49. P. Bergonzo et al., "Improving diamond detectors- A device case", Diamond and Related Materials, Vol.16, No.4-7, pp.1038-1043, April-July 2007.

50. W.P.Kang et al., "Nanodiamond lateral VFEM technology for harsh environments", IEEE Transactions on Nuclear Science, Vo.54, No.4, pp.1061-1065, August 2007.

51. K.J.Gabriel et al., "In situ friction and wear measurements in integrated polysilicon mechanisms", Sensors and Actuators A, pp. 84-188, February 1990.

52. E Kohn et al. "RF MEMS based on diamond", Workshop presentation, 35th European Microwave Conference, October 2005.

53. Electronic reference:

http://newton.ex.ac.uk/research/qsystems/people/sque/diamond/structure/

54. I.Ahmed, "Deposition of textured diamond using hot-filament assisted chemical vapor deposition method", Masters Thesis, University of South Alabama, 1998.

55. M.Amaral et al., "Growth rate improvements in the hot-filament CVD deposition of nanocrystalline diamond", Diamond and Related Materials, Vol.15, No.11-12, pp.1822-1827, November 2006.

56. M.Miyake et al., "Characteristics of nano-crystalline diamond films prepared in $Ar/H_2/CH_4$ microwave plasma", Diamond and Related Materials, Vo.51, No.9, pp.4258-4261, March 2007.

57. X.Zheng et al., "Investigation on the etching of thick diamond film and etching as a pretreatment for mechanical polishing", Diamond and Related Materials, Vol.16, No.8, pp.1500-1509, December 2006.

58. Y.K.Liu, et al., "Comparative study of nucleation processes for the growth of nanocrystalline diamond", Diamond and Related Materials, Vol.15, No.2-3, pp.234-238, February 2006.

59. J.C.Arnault et al., "Comparison of classical and BEN nucleation studied on thinned Si (111) samples: a HRTEM study", Applied Surface Science, May 2003.

60. D. M. Gruen, "Nanocrystalline Diamond Films", Annual Review of Material Science, Vol.29, pp.211-259, 1999.

61. W. Zhu et al., "Effects of noble gases on diamond deposition from methane-hydrogen microwave plasmas", Journal of Applied Physics, Vol.68, No.4, pp. 1489-1496, 1990.

62. M.Belmonte et al., "Wear resistant CVD diamond tools for turning of sintered hard metals", Diamond and Related Materials, Vol.12, No.3-7, pp.738-743, March-July 2003.

63. S.Turchetta et al., "CVD diamond insert in stone cutting", Diamond and Related Materials, Vol.14, No.3-7, pp.641-645, March-July 2005.

64. A.Glaser et al., "Deposition of uniform and well adhesive diamond layers on planar tungsten copper substrates for heat spreading applications", Materials Science and Engineering: B, Vol.127, No.2-3, pp.186-192, February 2006.

65. D.M.Gruen et al., "Deposition and Characterization of Nanocrystalline Diamond Films", Journal of Vacuum Science and Technology A, Vol.12, No.4, pp.1491-1495, 1994.

66. D. Zhou et al., "Control of diamond film microstructure by Ar additions to CH_4/H_2 microwave plasmas", Journal of Applied Physics, Vol.84, No.4, pp.1981-1989, 1998.

67. O. Auciello et al., "Materials science and fabrication processes for a new MEMS technology based on ultrananocrystalline diamond thin films", Journal of Physics: Condensed Matter, Vol.16, No.16, pp.539-552, 2004.

68. M.Kubovic, et al., "Surface channel MESFETs on nanocrystalline diamond" Diamond and Related Materials, Vo.14, No.3-7, pp. 514-517, 2005.

69. N. S. Xu et al., "Study of field electron emission from nanocrystalline diamond thin films grown from a N_2/CH_4 microwave plasma", Journal of Physics D: Applied Physics, Vol.33, No.3-4, pp.1421-1427, 2000.

70. U.A.Palnitkar et al., "Adhesion properties of nitrogen ion implanted ultra-nanocrystalline diamond films on silicon substrate", Diamond and Related Materials, Vol.17, No.4-5, pp. 864-867, 2008.

71. R.Haubner et al., "Comparison of sulfur, boron, nitrogen and phosphorus additions during low-pressure diamond deposition", Diamond and Related Materials, Vol.14, No.3-7, pp.355-363, 2001.

72. S.Bhattacharyya et al., "Synthesis and characterization of highly-conducting nitrogen-doped ultrananocrystalline diamond films", Applied Physics Letters, Vol.79, No.10, pp.1441-1443, 2001.

73. J.Zhang et al., "Characterization of boron-doped micro- and nanocrystalline diamond films deposited by wafer-scale hot filament chemical vapor deposition for MEMS applications", Diamond and Related Materials, Vol.17, No.1, pp.23-28, 2008.

74. D.A.Long, "Raman Spectroscopy", McGraw-Hill, 1977.

75. T. Lin et al., "Compositional mapping of the argon–methane–hydrogen system for polycrystalline to nanocrystalline diamond film growth in a hot-filament chemical vapor deposition system", Applied Physics Letters, Vol.77, No.17, pp.2692-2694, 2000.

76. Electronic reference: http://en.wikipedia.org/wiki/Young%27s_modulus

77. O.Auciello et al., "Are diamonds a MEMS's best friend?", IEEE Microwave Magazine, Vol.8, No.6, pp.61-75, 2007.

78. B.P.van Drieenhuizen et al., "Comparison of techniques for measuring both compressive and tensile stress in thin films", Sensors and Actuators A, Vol.38, pp.756-765, 1993.

79. M.G.Allen et al., "Microfabricated structures for the insitu measurement of residual stress, Young's modulus and ultimate strain of thin films", Applied Physics Letters, Vol.51, pp.241-243, 1987.

80. H.Guckel et al., "Fine grained polysilicon films with built-in tensile strain", IEEE Transaction on Electron Devices, Vol.35, No.6, pp.800-801, 1988.

81. J.Brank et al., "RF MEMS-based tunable filters", International Journal RF Microwave CAE, Vol.11, pp. 276-284, September 2001.

82. N.S.Barker et al., "Distributed MEMS true-time delay phase shifters and wide band switches", IEEE Transactions on Microwave Theory and Techniques, Vol.46, No.11, pp.1881-1890, November 1998.

83. C.W.Baek et al., "2D mechanical beam steering antenna fabricated using MEMS technology", IEEE MTT-S International Microwave Symposium, pp.211-214, June 2001.

84. J.Bryzek et al., "Marvelous MEMS", IEEE Circuits and Devices Magazine, Vol.22, No.2, pp.8-28, March-April 2006.

85. A.Aleksov et al., "First diamond FET RF power measurement on diamond quasi-substrate", 60th Device Research Conference, pp.181-182, June 2002.

86. P.Schmid et al., "Diamond switch using new thermal actuation scheme", Diamond and Related Materials, Vol.12, No.3-7, pp.418-421, March-July 2003.

87. Electronic Reference: http://en.wikipedia.org/wiki/Hooke%27s_law

88. P.Benkart et al., "3D chip stack technology using through-chip interconnects", IEEE Design and Test of Computers, pp.512-518, November 2005.

89. S.Balachandran et al., "MEMS tunable planar inductors using DC contact switches", 34th European Microwave Conference, Vol.12, pp.713-716, October 2004.

90. J. B. Muldavin, "Design and analysis of series and shunt MEMS switches," Ph.D. dissertation, Department of Electrical Engineering and Computer Science, The University of Michigan at Ann Arbor, Ann Arbor, MI, 2001.

91. C.L.Goldsmith et al., "Lifetime characterization of capacitive RF MEMS switches", IEEE MTT-s International Microwave Symposium, Vol.1, pp.227-230, May 2001.

92. Z.Peng et al., "Dielectric Charging of RF MEMS capacitive switches under bipolar control-voltage waveforms", IEEE International Microwave Symposium, pp.1817-1820, June 2007.

93. X.Yuan et al., "Modeling and characterization of dielectric-charging effects in RF MEMS capacitive switches", IEEE International Microwave Symposium, pp.753-756, June 2005.

94. M.Adamschik et al., "Diamond microwave micro relay", Diamond and Related Materials, Volume 12, No.3-7, pp.342-346, July 2003.

95. S.Balachandran et al., "Thermally actuated nanocrystalline diamond micro-bridges for microwave and high-power RF applications", IEEE International Microwave Symposium, pp.367-370, June 2007.

96. Agilent Advanced Design System Linecalc, Version 2006A.

97. P. Edelman et al., "Non-contact charge-voltage method for dielectric characterization on small test areas of IC product wafers", Materials Science in Semiconductor Processing", Vol.9, No.1-3, pp.252-256, June 2006.

98. T. Wang et al., "Hot hole stress induced leakage current (SILC) transient in tunnel oxides", IEEE Electron Device Letters, Vol.19, No.11, pp.411-413, November 1998.

99. S.M.Sze, "Physics of semiconductor devices", John Wiley and Sons, 1981.

Appendices

Appendix A Photolithography Procedures

The photolithography steps for 3000 PY negative resist is:

- Clean sample with Acetone and Methanol. Blow dry with Nitrogen

- Spin coat the sample with Futurrex 3000PY at 3000 rpm for 40 seconds

- Soft bake sample at 155^0C for 60 seconds on a hot plate

- Expose the sample for 17 seconds in UV-light. A mask aligner is used for this purpose

- Hard bake at 110^0C for 60 seconds.

- Develop the exposed photoresist in RD-6 for 25 seconds. Rinse the sample with DI water thoroughly and blow dry with Nitrogen.

- Typical thickness : 3.4 - 3.6 µm

Three kinds of Shipley^{TM} resists were used for varying thickness which includes SC 1813, 1818, and 1827. The photolithography steps for SC 18xx resist is:

- Clean sample with Acetone and Methanol. Blow dry with Nitrogen

- Spin coat HMDS followed with the photoresist at 2500 rpm for 30 seconds. HMDS is used for adhesion

- Soft bake at 110^0C for 70 seconds.

- Expose in the mask aligner for 25 seconds

- Develop in MF-319 for 80 seconds. Rinse thoroughly in DI water and blow dry with nitrogen.

The photolithography steps for AZ 5214 resist is:

- Spin PMGI SF 11@ 2500rpm for 45 secs

- Bake it @ 180^oC for 5 minutes in the hot plate

- Repeat this process twice to yield a thickness of close to 2 microns

- After cooling down, spin AZ 5214 @ 4000rpm for 45 secs

- Bake it @110°C for 90 seconds in the hot plate

- Expose using the mask aligner (Channel 2) for 6 seconds

- Develop the photo-resist in AZ 726 for 35 seconds

- Expose the PMGI in the Deep UV system for 50 minutes. This is done to expose the PMGI completely

- Develop in 101 developer for 4 minutes.

The photolithography process for AZ 9260 resist is:

- Spin AZ 4533 thinner 1:50 (adhesion promoter) @ 6000rpm for 45 secs

- Bake it @ 180°C for 5 minutes in the hot plate

- After cooling down, spin AZ 9260 @ 6000rpm for 45 secs

- Bake it @110°C for 3 minutes in the hot plate

- Expose using the mask aligner (Channel 2) for 27 secs

- Develop the photo-resist in AZ 400K: H$_2$O {1:4}for 3 minutes

- Rinse in water thoroughly for 2-3 minutes

The photolithography process for maN 490 resist is:

- Spin maN @ 3000rpm for 45 secs

- Bake @ 100°C for 10 minutes

- Expose in CI2 for 45 secs

- Develop in mA-332 for 1 -1.5 minutes

- Oxygen plasma for 2 minutes

Appendix B   Fabrication of the Diamond Actuator and Host Substrate

- A two inch low resistive silicon substrate is thoroughly cleaned with acetone and methanol and blow dried with nitrogen

- An intrinsic diamond layer is grown in the big plasma system to a thickness of 1500 A^0

- Boron doped (p-type) nanocrystalline diamond is grown to a thickness of 1.4 μm

- The silicon wafer with the nanocrystalline diamond is cleaned in Piranha solution (1 part of H_2O_2 + 2 parts of H_2SO_4) and then subjected to oxygen plasma for the diamond to be oxygen terminated. Oxygen terminated is necessary for good adhesion of metal or dielectric film with nanocrystalline diamond. The recipe of the oxygen plasma is:
  - O_2 gas : 6 sccm ; Pressure: 100 mT ; Power: 100 watts ; Time: 2-3 mins

- Silicon dioxide is grown using a PECVD process to a thickness of 300nm. This oxide layer is used as the masking layer for growing intrinsic diamond on top of the doped diamond layer

- A positive tone lithographic process is carried to pattern the silicon dioxide. After the lithography step, silicon dioxide is etched in CF4 plasma in the RIE system. The recipe for etching the oxide is:
  - CF_4 gas: 45 sccm ; Pressure: 40 mT ; RF power: 600 watts; Time: 20 mins

- The photo-resist, which is used as the etch mask for silicon dioxide is removed by dipping in the above mentioned piranha solution for close to 2 minutes. The photo-resist is completely removed in this process and the wafer is thoroughly rinsed with DI water

- Intrinsic diamond is grown in the two samples using the hot filament CVD technique to a thickness of 300 nm

- After the intrinsic diamond growth, remaining SiO_2 is etched in the RIE for 30 minutes

Appendix B (Continued)

- Backside of the wafer was etched in the RIE system. During intrinsic diamond growth, traces of diamond are deposited on the backside. The wafers are treated in pure oxygen plasma to etch this diamond. The recipe is:
  - O_2 gas: 45 sccm; Pressure: 40 mT; Power: 800 watts; Time: 30 mins
- The wafer is cleaned in acetone and IPA and treated in oxygen plasma
- A seed layer of Ti (60 A^0) and Au (500 A^0) is deposited using an e-beam evaporator. This seed layer is required for electroplating in the subsequent steps
- Lithography is done to open the areas of the bi-metal (copper) using a positive resist. The mask is a dark field mask, so 5214 resist is used for the lift off process
- Copper which is used for the thermal actuation scheme (bi-metal pads) is deposited using a thermal evaporator to a thickness of 2 μm
- After the bi-metal (Cu) layer, the center contact pads along with the solder pads are to be electroplated. A single spin lithography using AZ 9260 is carried out to yield a thickness of 8-9 μm
- Copper is electroplated to a thickness of 5 μm with a current setting of 3 mA and voltage setting of 0.25 volts. Electroplating is slowly done to ensure no stress build up in the copper films
- The silicon wafer is cleaned with acetone and methanol and ashed in oxygen plasma
- Tin solder pads are included in the actuator portion in the second generation switches. A two spin lithography using AZ 9260 is carried out to yield a thickness of 14 μm
- Tin is electroplated to a thickness of 2-3 μm with a voltage setting of 0.16 volts
- Photo-resist is removed by rinsing the samples thoroughly in 1 methyl 2 pyrilidone (1M2P). This is followed by rinsing the wafers in acetone and iso-propanol.

113

- Photo-resist is used as the mask to etch the seed layer. A two spin lithography using AZ 9260 is carried out to yield a thickness of 14 μm. The seed layer is etched in the RIE system and the recipe is:
  - Ar: 45 sccm; Pressure: 40 mT; Power: 1200 watts; Time: 10 mins for etching gold
  - CF_4: 45 sccm; Pressure: 40 mT; Power: 600 watts; Time: 30 mins for etching titanium
- Titanium (Ti) is used as the hard mask for etching diamond. Hence close to 380nm of titanium is deposited in the ion beam. This is a time consuming and slow process and also the samples are kept in two distinct positions in order to facilitate conformal coating of Ti throughout the wafer. This is a very crucial step, as non-conformal deposition of Ti will mean etching diamond from places where it should be protected. During deposition 5-7 minute break is given after every 30 minutes of deposition
- A single spin lithography using AZ-9260 is carried out to pattern the Ti layer. Ti is etched in the RIE using the following recipe:
  - Pressure: 40mT ; Gas: CF_4 (45 sccm); Power:600 watts ; Time: 45mins
- After removing the photo-resist using acetone and methanol, Ti is used as the hard mask to etch diamond in the RIE system. The recipe for etching diamond is:
  - Pressure: 10 mT; Gas: O_2 (8 sccm), Ar (3 sccm); Power: 1000 watts; Time:10 minutes
  - Pressure: 10mT; Gas: CF_4 (10 sccm); Power:500 watts; Time:10 secs
  - These two steps are repeated for a total of 3 hrs to etch the diamond
- After removing the photo-resist used to pattern the Ti layer, a single spin lithography process using maN 490 is carried to deposit platinum (Pt) on the copper contact pad. Ti (50 A^0) and Pt (500 A^0) are deposited using an e-beam evaporator

Appendix B (Continued)

- To release the diamond beams, silicon is etched in a DRIE system using aluminum (Al) as a hard mask. Al is deposited using an e-beam evaporator to a thickness of 4000 A^0. Prior to this, a single spin lithography using AZ 5214 is done.

- The host substrates (alumina, aluminum nitride) are cleaned using acetone and methanol.

- A seed layer of Ti (100 A^0) and Au (1200 A^0) is deposited using an e-beam evaporator. A single spin lithography using AZ 9260 is carried out to open the transmission line areas.

- The transmission lines are gold electroplated to a thickness of 3-4 μm. The copper solder pads are electroplated to a thickness of 2-3 μm using the same procedure.

- The diced diamond actuators are integrated onto the host substrate using the SOLID process with a flip chip bonder.

Appendix C   Fabrication of the Capacitive Shunt Switch

- A one inch high resistive silicon substrate is thoroughly cleaned with acetone and methanol and blow dried with nitrogen

- Molybdenum (Mo), which is the bottom electrode, is sputtered to a thickness of 0.9 μm. For the second generation switches tungsten is used as the bottom electrode. Tungsten (W) is deposited to a thickness of 1 μm after depositing a seed layer of Ti which is 200 A^0 thick.

- Both Mo and W are etched in an RIE system. Prior to etch process, a single spin 1827 lithography process is carried out. The etch recipe for W and Mo is:
  - CF_4 gas: 40 sccm; O_2 gas: 5 sccm; Pressure: 100 mT; Power: 150 watts; Time: 15 mins

- Nanocrystalline diamond ((NCD) is grown using the MPECVD technique to a thickness of 0.5 μm

- Titanium is used as the hard mask to etch diamond. Titanium is deposited using lift-off technique to a thickness of 4000 A^0. Prior to the deposition, a single 3000 PY lithography process is carried out. The etch recipe for NCD film is:
  - O_2 gas: 50 sccm; CF_4 gas: 5 sccm; Pressure: 50 mT; Power: 350 watts; Time: 30 mins

- Gold transmission lines are patterned using a single spin 3000 PY lithography process and lift-off technique to a thickness of 1 μm

- PMMA which is used as the sacrificial layer is spun to a thickness of 2 μm. After spinning PMMA, titanium is patterned using 3000 PY lithography process and lift-off technique to a thickness of 300 A^0. This titanium layer is used as the hard mask for etching PMMA. The etch recipe for PMMA is:
  - O_2 gas: 25 sccm; Pressure: 100 mT; Power: 100 watts; Time: 10 -15 mins

Appendix C (Continued)

- Titanium is removed in 1:20 ($HF:H_2O$) and cleaned thoroughly in DI water. A seed layer of Ti (200 A^0) and Au (2000 A^0) is deposited using an e-beam system.

- A single spin lithography process is carried out using 1827 photo-resist to open up the beam areas

- The beam along with the pedestal is gold electroplated to a thickness of 2 microns. In electroplating, the gold solution is heated to a temperature of 60^0C in a hot plate with a stirrer set to 2000 rpm. The current rating is set to 0.06 mA. The thickness of the platted gold is measured using a profilometer. The procedure is repeated if the thickness is not equal to the desired value. Prior to measuring the thickness, the samples are rinse using DI water and blow dried with nitrogen.

- Then using a bright-field beam mask, the beam and pedestal layers are protected with a positive resist, preferably 1827, using the positive tone process

- The seed layer is etched throughout the sample apart from the protected beam areas. Gold is etched at 25^0C at a rate of 25 A^0/sec and chrome is etched at 40^0C at a rate of 40 A^0/sec in gold and chrome etchant respectively

- Finally the samples are kept in beaker of 1165 solution heated to 80^0C overnight and later rinsed in DI water and isopropyl alcohol.

- Prior to placing the samples in the critical point dryer (CCP), they are kept in a beaker of high purity methanol. Following the procedure given, the samples are dried in the CCP, which is filled with the high purity methanol.

- If photo-resist is still sticking on to the sample, it can be removed by ashing the same in a plasma etcher. The typical settings are:
    o O_2 gas: 40 sccm; Pressure: 250 mT; Power: 100 watts; Time: 2 mins

About the Author

Srinath Balachandran received his Bachelor of Engineering in 2000 from the University of Madras, India. He started his M.S program in fall 2001 and worked with Dr. Thomas Weller from the summer of 2002 specializing in the area of RF-MEMS. Srinath completed his M.S degree in spring 2004. Upon completion, he enrolled into the Ph.D. program starting from fall 2004. His research interests are in the area of RF-MEMS techniques for microwaves, application of micromachining for mm-wave circuits.